



저작자표시-비영리-변경금지 2.0 대한민국

이용자는 아래의 조건을 따르는 경우에 한하여 자유롭게

- 이 저작물을 복제, 배포, 전송, 전시, 공연 및 방송할 수 있습니다.

다음과 같은 조건을 따라야 합니다:



저작자표시. 귀하는 원저작자를 표시하여야 합니다.



비영리. 귀하는 이 저작물을 영리 목적으로 이용할 수 없습니다.



변경금지. 귀하는 이 저작물을 개작, 변형 또는 가공할 수 없습니다.

- 귀하는, 이 저작물의 재이용이나 배포의 경우, 이 저작물에 적용된 이용허락조건을 명확하게 나타내어야 합니다.
- 저작권자로부터 별도의 허가를 받으면 이러한 조건들은 적용되지 않습니다.

저작권법에 따른 이용자의 권리는 위의 내용에 의하여 영향을 받지 않습니다.

이것은 [이용허락규약\(Legal Code\)](#)을 이해하기 쉽게 요약한 것입니다.

[Disclaimer](#)

공학박사학위논문

**Single-molecule analysis of
biomolecules using solid-state
nanopores**

솔리드스테이트 나노포어를 이용한 생체
분자의 단일분자 수준 분석

2019년 8월

서울대학교 대학원
재료공학부
유재석

Single-molecule analysis of biomolecules using solid-state nanopores

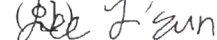
솔리드스테이트 나노포어를 이용한 생체분자의
단일분자 수준 분석

지도교수 김 기 범

이 논문을 공학박사 학위논문으로 제출함
2019 년 7 월

서울대학교 대학원
재료공학부
유 재 석

유 재 석의 박사 학위논문을 인준함
2019 년 5 월

위 원 장	남 기 태	
부 위 원 장	김 기 범	
위 원	선 정 윤	
위 원	김 영 록	
위 원	이 지 은	

ABSTRACT

SINGLE-MOLECULE ANALYSIS OF BIOMOLECULES USING SOLID-STATE NANOPORES

Jae-Seok Yu

Department of Materials Science and Engineering

The Graduate School

Seoul National University

The nanopore is a biosensor capable of detecting small size molecules such as DNA, RNA, protein, and peptide with high sensitivity. Basically, a nanopore is a nanometer-sized pore formed on a thin, impermeable membrane, which can be lipid bilayers or solid-state thin films. When a biomolecule passes through a nanopore by an electric field, it generates a current drop, which is used to analyze physical and chemical properties of the passing molecule. This dissertation focuses primarily on improvements in solid-state nanopore devices and single-molecule level analysis of biomolecule using the nanopore device.

Chapter 1 contains a general introduction to the nanopore technologies. First, the basic sensing principles of nanopore are described in detail, and two major classes of nanopores, biological nanopores and solid-state nanopores, are introduced. Biological nanopores such as α -hemolysin and MspA, are pore-shaped proteins which are inserted into lipid bilayers to form ion channels. Solid-state nanopores, developed to improve

the limitations of biological nanopores, have the advantages of robustness, durability, chemical stability, and ability to tune the nanopore dimensions. Several limitations of solid-state nanopores for high detection sensitivity and studies to overcome them are also described in this chapter.

In chapter 2, the fabrication processes for improving the membrane quality of low noise solid-state nanopore is described. A low noise solid-state nanopore platform has been developed using a quartz substrate to reduce the dielectric noise. However, the silicon nitride membrane used in the device had limitations in the membrane quality. Due to the transfer method, plasma-enhanced chemical vapor deposition (PECVD) silicon nitride had to be used, which caused pore expansion during the measurement and instability during high temperature cleaning. In addition, the polymer supporting layer used in the transfer process was not completely removed, but remained on the surface of the nanopore membrane, resulting in protein adsorption. Here, we developed a method for transferring high quality low-pressure chemical vapor deposition (LPCVD) silicon nitride to the low noise nanopore platform without a supporting layer. The nanopore membrane had a clean and uniform surface and exhibits excellent noise properties.

In chapter 3, we explore the possibility of using peptide-based materials as a membrane in solid-state nanopore devices as an effort to develop a sequence-specific, programmable biological membrane platform. We use a tyrosine-mediated self-assembly peptide sheet. At the air/water interface, the 5mer peptide YFCFY self-assembles into a uniform and robust two-dimensional structure, and the peptide sheet is easily transferred to a low-noise substrate. The thickness of the peptide membrane can be adjusted to approximately 5 nm by an etching process, and the diameters of the

peptide nanopores can be precisely controlled using a focused electron beam with an attuned spot size. The ionic current noise of the peptide nanopore is comparable to those of typical silicon nitride nanopores or multilayer two-dimensional materials. Using this membrane, we successfully observed translocation of double-stranded DNA (dsDNA) with sufficient signal-to-noise ratio (SNR) of ~ 30 and an elongated translocation speed of ~ 1 bp/ μ s. Our results suggest that the self-assembled peptide film can be used as a sensitive nanopore membrane and employed as a platform for applying biological functionalities to solid-state substrates.

In chapter 4, we demonstrate a rapid identification of the location of zinc finger protein (ZFP), which is bound to a specific locus along the length of a dsDNA to a single protein resolution using a low noise solid-state nanopore. When ZFP labeled DNAs were driven through a nanopore by an externally applied electric field, characteristic ionic current signals arising from the passage of the DNA/ZFP complex and bare DNA were detected, which enabled us to identify the locations of ZFP binding site. We examined two DNAs with ZFP binding sites at different positions and found that the location of the additional current drop derived from the DNA/ZFP complex is well-matched with a theoretical one along the length of the DNA molecule. These results suggest that the protein binding site on DNA can be mapped or that genetic information can be read at a single molecule level using solid-state nanopores.

In chapter 5, we attempted to distinguish between three similar peptide sequences (~ 40 amino acids, ~ 5 kDa) that differed only by location or number of cysteine residues with solid-state nanopores. The cysteine residues are located at one end, one at the center, and at both ends for each of three peptides. We found that differentiation of the three types of peptides by nanopore signals was difficult. However, when the cysteine

residue was labeled with a negatively charged molecule, Flamma[®] 496, the labeled peptides showed distinct signals for each peptides. Comparing the relative current blockades of labeled peptides with applied voltages, we found the label was able to change peptide conformations and the resulting ionic current signals from the three labeled peptides were distinguished based on relative current blockade, full width at half-maximum of the current blockade distribution, and single-molecule level peak shape analysis. Our results suggest that solid-state nanopores combined with a targeted labeling strategy could be used to obtain characteristic peptide signatures that could ultimately be used for protein identification.

Keywords: nanopore, solid-state nanopore, single-molecule, DNA sequencing, protein, peptide, transcription factor, biosensor, protein identification, DNA-protein interaction

Student number: 2013-22479

Table of contents

Abstract	i
Table of contents	v
List of figures	viii

CHAPTER 1. Introduction	1
1.1. Nanopore technologies	2
1.1.1. Basic principles and history of nanopores	2
1.1.2. Fabrication methods of solid-state nanopores	7
1.1.3. Biological applications of solid-state nanopores	13
1.2. Issues in solid-state nanopores	25
1.2.1. Spatial resolution	25
1.2.2. Signal to noise ratio	30
References	36

CHAPTER 2. Enhancement of Solid-State Nanopore Membrane	43
2.1. Introduction	44
2.2. Results and discussion	47
References	51

CHAPTER 3. DNA Translocation through a Nanopore in Ultrathin Self-assembled Peptide Membrane 53

3.1. Introduction 54

3.2. Experimental details 57

3.3. Results and discussion 59

 3.3.1. Peptide film characterization and nanopore formation 59

 3.3.2. Nanopore conductance measurements and noise characteristics 65

 3.3.3. DNA translocation through a peptide nanopore 67

3.4. Summary 71

References 72

CHAPTER 4. Identifying the Location of a Single Protein along the DNA Strand Using Solid-State Nanopores 81

4.1. Introduction 82

4.2. Experimental details 87

4.3. Results and discussion 93

 4.3.1. Translocation of short DNA (520 bp)/ZFP complex 93

 4.3.2. Characterization of DNA/ZFP binding 98

 4.3.3. Translocation of long DNA (5605 bp)/ZFP complex and identifying the binding locations 102

4.4. Summary 110

References 111

CHAPTER 5. Differentiation of Selectively Labeled Peptides using Solid-State Nanopores	119
5.1. Introduction	120
5.2. Experimental details	123
5.3. Results and Discussion	125
5.3.1. Schematics of the experiments	125
5.3.2. Electroosmotic capture of unlabeled peptides	129
5.3.3. Nanopore measurement of three unlabeled peptides	132
5.3.4. Capture rate of labeled peptides in the EO and EP directions	134
5.3.5. Stretching of labeled peptides in the EP direction	138
5.3.6. Nanopore measurement of three labeled peptides	141
5.3.7. Comparison of peak shapes of the three labeled peptides	144
5.4. Summary	149
References	150
 CHAPTER 6. Summary and Conclusions	 157
 Abstract (in Korean)	 161
List of publications	165

List of figures

Chapter 1

Figure 1-1. Basic idea of nanopore sequencing. Adopted from ref. 2.

Figure 1-2. (a) Representative translocation signals of poly[U] through α -hemolysin and the blockade lifetimes according to (b) the length of poly[U] and (c) the applied potential. Adopted from ref. 3.

Figure 1-3. (a) Feedback-controlled ion-beam sculpting method. (b) TEM image of ~ 60 nm diameter pore made by FIB in a 500 nm Si_3N_4 membrane. (c) TEM image of the nanopore after ion-beam exposure. Adopted from ref. 4.

Figure 1-4. (a) A schematic diagram of silicon oxide nanopore device. (b) A schematic diagram of electron beam applied to a nanopore membrane. (c) TEM images of silicon oxide nanopores of various sizes formed by electron beam. Adopted from ref. 5.

Figure 1-5. (a) Surface free energy according to the ratio of pore radius, r and thickness, h . For pores with $r < h/2$, it is preferred that the radius shrinks in terms of free energy. (b) Nanopore diameters according to electron beam density and irradiation time. Adopted from ref 5 and 6.

Figure 1-6. The formation processes of nanopores by dielectric breakdown. (a) An

electric field is formed inside the membrane due to the application of electric potential on both sides of the silicon nitride membrane. (b) Leakage current generation due to trap-assisted tunneling of ions at the membrane surfaces. (c) A localized conductive path is generated by accumulation of traps. (d) Nanopore formation. Adopted from ref. 7.

Figure 1-7. Scatter plots of dsDNA passing through a 10 nm nanopore events of (a) simple events with a single blockade level and (b) complex events. Adopted from ref. 9.

Figure 1-8. (a) A schematic diagram of quartz-based low noise solid-state nanopore and optical microscope image of the nanopore device. (b) Concatenated traces of translocation of poly A, T, and C. (c) Histogram of the residual currents of poly A, T, and C. (d) Concatenated traces of translocation of mixture of poly A and T. (e) Histogram of the residual currents of the mixture of poly A and T. Adopted from ref. 14.

Figure 1-9. (a) Schematic of the silicon chip with 5 μm of SiO_2 layer inserted. (b) TEM image of a nanopore. (c) Concatenated translocation events and current drop histograms of poly(dA), poly(dC), and poly(dT). Adopted from ref. 15.

Figure 1-10. Schematic diagrams of a BSA and a fibrinogen proteins and their nanopore translocation current blockade, dwell time, and ECD (event charge deficit) histograms. Adopted from ref. 16.

Figure 1-11. (a) Schematic drawing of protein states during nanopore translocation through silicon nitride nanopores. (b) Excluded volume generated when the proteins pass through the nanopore. Inset: the difference in excluded volume depending on the presence or absence of urea. Adopted from ref. 17.

Figure 1-12. Detection of virus-antibody interaction using solid-state nanopores. The increase in volume due to antibody binding is reflected in the nanopore current drop amplitude. Adopted from ref. 19.

Figure 1-13. (a) Representative nanopore signals of gp120 protein, antibody monomer, and antibody dimer. (b) The current drop histogram of gp120 showing a single peak. (c) The current drop histogram of antibody showing two distinct peaks. Adopted from ref. 20.

Figure 1-14. (a) Schematic diagram of nanopore drug screening. Nanopore translocation of p53-MDM2 complex is determined by Nutlin-3 binding. (b) Example nanopore current traces of (I) free MDM2, (II) MDM2 + GST-p53TAD, (III) MDM2 + GST-p53TAD + Nutlin-3, and (IV) MDM2 + GST-p53TAD + ABT-737. Adopted from ref. 21.

Figure 1-15. (a) Ionic current traces of ssDNA translocation through 5 nm, 10 nm, and 20 nm thick SiN nanopores. (b) Thinning SiN nanopore membrane using SF₆ RIE process and its etch depth versus etch time. (c) Thinning of SiN nanopore membrane by electron irradiation. Adopted from ref. 14, 22, and 23.

Figure 1-16. (a) Optical microscope images of graphene nanopore membrane on SiN layer and DNA translocation signals of the graphene nanopore. (b) The fabrication processes of BN nanopore and the current traces of DNA translocation. (c) Schematic diagram of MoS₂ nanopore chip, and optical and TEM images of MoS₂ nanopore structure. Adopted from ref. 24, 25, and 26.

Figure 1-17. An example noise power spectral density versus frequency. Four different noise sources are shown according to the frequency regime.

Figure 1-18. Reduction in dielectric noise of solid-state nanopores. (a) A schematic diagram of PDMS coated nanopore chip and a noise PSD plot of a bare Si/SiN nanopore, a PDMS coated nanopore, and an alpha-hemolysin nanopore. (b) A schematic diagram of a nanopore chip with a 5 μm SiO₂ layer inserted and a thick glass layer integrated. (c) A schematic diagram of a quartz-based nanopore device and an optical microscope image. (d) A schematic diagram of glass nanocapillary nanopore. Adopted from ref. 14, 31, 32, 33, and 34.

Chapter 2

Figure 2-1. (a) A TEM image of the surface of a transferred PECVD SiN membrane. (b) Example ionic current traces when DNA or DNA/protein complexes pass through a PECVD SiN nanopore. (c) Noise PSD plot of ionic current traces in b.

Figure 2-2. Schematic illustration of fabrication process for LPCVD SiN nanopore on the quartz substrate. (a) 100 nm thick SiN membrane on Si substrate and a quartz chip are prepared using photolithography and a wet etching processes. (b) The SiN membrane is transferred on a quartz substrate in the DI water. (c) The Si substrate is removed. (d) SiN membrane thickness is reduced to a desirable level using RIE.

Figure 2-3. (a) A TEM image of the surface of LPCVD SiN membrane. (b) Example TEM images of LPCVD SiN nanopores of 2 nm, 4 nm, and 6 nm. (c) Noise PSD plots of 10 nm thick and 5 nm diameter LPCVD SiN nanopore when electric potential of 0 mV and 200 mV were applied.

Chapter 3

Figure 3-1. Peptide film characteristics. (a) Chemical structure of YFCFY. (b) Oblique view of droplet with a single large facet on siliconized glass. (c) TEM image of peptide film assembled at the air/water interface. (d) Optical images of peptide film transferred to silicon nitride membrane. (e) Schematic diagram of a peptide nanopore on silicon nitride supporting layer. (f) TEM images of ~ 5 nm peptide nanopore.

Figure 3-2. Thickness and diameter control of peptide nanopores. (a) Thickness of YFCFY film when exposed to a 5% methanol solution. (b) AFM image of YFCFY film after thinning. (c) Nanopore forming rate under $\sim 10^7$ e/nm²·s electron beam irradiation. (d) TEM images of peptide nanopores with various diameters.

Figure 3-3. Peptide film stability under high density of electron beam.

Figure 3-4. Peptide nanopore characteristics in ionic solutions. (a) I - V characteristics of peptide nanopores in 1 M KCl. Inset: I - V curve of ~ 2.5 nm peptide nanopore. (b) Noise PSD of a peptide nanopore under applied voltages of 0 and 100 mV. (c) I_{RMS} of the peptide nanopore under applied voltages of 0 to 500 mV. (d) Normalized PSD and noise power fitting.

Figure 3-5. DNA translocation through peptide nanopores. (a) Current traces of 1000-bp DNA translocation at three applied voltages. (b) Scatter plot and current drop histograms of DNA translocation events. (c) SNR at three applied voltages. (d) Dwell

time histograms for three voltages. (e) Representative events showing dragging effects at the pore entrance (scales are not same).

Figure 3-6. Zeta potential of YFCFY peptide films.

Chapter 4

Figure 4-1. Schematic illustrations of nanopore-based identification of DNA-protein interactions. (a) A translocation event of a bare dsDNA gives rise to a single level current drop. (b) dsDNAs with ZFP binding sites at different parts of the strands display an additional current drop peak in accordance with the binding site. (c) Schematics of two dsDNAs used in this work. One is 5605 bp with a 20 bp binding site at the 2-to-5 position and the other is 520 bp with a 20 bp binding site at the center. (d) Cross-sectional illustration of a low noise solid-state nanopore device used in this work (not to scale).

Figure 4-2. The effect of KCl on ZFP-DNA dissociation. Zinc finger proteins bound to immobilized target DNA with its specific recognition sequence were exposed to varying KCl concentrations. The level of remaining ZFP on its target DNA after treating the sensor chip with a given KCl concentration was presented. ZFP binding to a target DNA was not affected at low KCl concentrations. Dissociation began at 0.5 M KCl, and most of proteins seemed to dissociate at KCl concentrations over 0.7 M.

Figure 4-3. Analysis of DNA (520 bp, binding site at the center) translocation events with ZFP in 400 mM KCl. (a) Current traces from the translocation of DNA-ZFP complex under three different applied voltages. Two types of event signals were detected. (b) Scatter plot of translocation events for 100 mV applied voltage. Type (I) and type (II) events were indicated as navy diamonds and green circles, respectively.

Type (II) events clearly show higher current drop and longer dwell time. (c) The frequency of translocation events as a function of applied voltage, showing an exponential increase in event frequency along with increased applied voltage. (d) Histogram of $t_1/(t_1+t_2)$, where t_1 is assigned as the dwell time from the start of the event to the additional spike, and t_2 is assigned as the dwell time from the additional spike to the end of the event.

Figure 4-4. AFM images of bare DNA (a) and the DNA-ZFP complex (b). DNA (520 bp) that was approximately 180 nm in length was used in this analysis. The scan sizes of the images are 250×250 nm with Z-scale of 4 nm. Gel-shift assay of 520 bp DNA (c) and 5605 bp DNA (d) in the presence and absence of ZFP. Lane 1, DNA marker; Lane 2, DNA without recognition sequence; Lane 3, DNA without recognition sequence reacted with ZFP; Lane 4, DNA with recognition sequence; Lane 5, DNA with recognition sequence reacted with ZFP; Lane 6, ZFP alone.

Figure 4-5. Gel-shift assay of bare DNA and the DNA/ZFP complex run on a 10% native polyacrylamide gel and stained with EtBr (a) and coomassie blue (b). Lane 1, DNA marker; Lane 2, DNA (134 bp) without recognition sequence; Lane 3, DNA (134 bp) without recognition sequence reacted with ZFP; Lane 4, DNA (126 bp) with recognition sequence; Lane 5, DNA (126 bp) with recognition sequence reacted with ZFP; Lane 6, ZFP. The protein bands in the lower position are from unbound free ZFPs.

Figure 4-6. Analysis of DNA translocation events (5605 bp, binding site at 2-to-5 position) with ZFP in 500 mM KCl. (a) Current traces from the translocation of DNA-

ZFP complex under three different applied voltages. Representative translocation signals from bare DNA (Type I) and DNA/ZFP (Type II) are shown. (b) Scatter plot of DNA translocation events (5605 bp)/ZFP through 7 nm nanopore on 20 nm thick SiN. Type (I) events were indicated as navy diamonds, and type (II) events were indicated as green circles, respectively. (c) All-point current histogram for DNA/ZFP translocations, showing discrete peaks for Type (I) and Type (II) events. (d) The frequency of translocation event as a function of applied voltage, which shows exponential increase of frequency upon increased voltage level.

Figure 4-7. (a) A representative event signal of DNA (5606 bp)/ZFP translocations. Open pore current is indicated as I_0 , the first current blockade level is I_{DNA} , and the additional current drop is I_{ZFP} . The first current drop magnitude from the open pore current ($I_0 - I_{DNA}$) is indicated as ΔI_{DNA} , and the magnitude of the additional current drop ($I_{DNA} - I_{ZFP}$) is indicated as ΔI_{ZFP} . (b) Voltage dependency of ΔI_{DNA} and ΔI_{ZFP} . Both linearly increase with applied bias voltages. (c) Voltage dependency of $\Delta I_{ZFP}/\Delta I_{DNA}$. $\Delta I_{ZFP}/\Delta I_{DNA}$ is almost constant (~ 0.355) for three applied voltages.

Figure 4-8. (a) Histogram of $t_1/(t_1+t_2)$, where t_1 is assigned as the dwell time from the start of event to the additional spike and t_2 is assigned as the dwell time from the additional spike to the end of the event. Two Gaussian distributions were observed due to two opposite translocation directions. (b) Histogram of t_1/t_2 , where the shorter end of DNA from the ZFP binding site is analyzed as t_1 and the longer end is analyzed as t_2 .

Chapter 5

Figure 5-1. (a) Schematic diagram of the nanopore experiment (not to scale). LPCVD silicon nitride of < 10 nm thickness is used as a nanopore membrane on a quartz substrate. (b) Representative TEM images of silicon nitride nanopores of diameters < 2 nm. (c) Schematic diagrams of the three peptides of ~ 5 kDa used in the experiment (Detailed information is shown in Table 1 and Figure 5-2). (d) Example 2.5 s current traces of the Pep A solution when ± 200 mV is applied across the ~ 1.6 nm diameter nanopore. (e) $\Delta I/I_0$ distribution of Pep A translocation through three different nanopore diameters in the EO direction (black: ~ 1.6 nm, red: ~ 2.2 nm, and blue: ~ 3.4 nm).

Figure 5-2. Theoretical volume of the peptides used in the experiment. (a) Pep A, (b) Pep B, and (c) Pep C. We performed simulations using the NAMD 2.9 package with the CHARMM 27 force field with the protein parameters incorporating the CMAP.

Figure 5-3. Calculated velocities of Pep A in EO and EP directions The electrophoretic velocity, v_{EP} and electroosmotic velocity, v_{EO} of the Pep A in ionic solution can be calculated as follows.

Figure 5-4. Differentiation of unlabeled peptides. (a) $\Delta I/I_0$ distribution of unlabeled Pep A (navy), (b) Pep B (dark yellow), and (c) Pep C (red) when -100 mV was applied across a 1.6 – 1.8 nm diameter nanopore. (d) Relative current blockade $\Delta I/I_0$ (black) and FWHM (green) of the $\Delta I/I_0$ distribution for three types of peptide.

Figure 5-5. Comparison of translocation characteristics of EO and EP directions of Pep A labeled with the negatively charged molecule. (a) Example 2.5 s current traces of the labeled Pep A solution when ± 200 mV is applied across an ~ 1.8 nm diameter nanopore. (b) Capture rate, R_C , of labeled Pep A through a nanopore in the EO (blue circle) and EP (gray square) directions, respectively, according to the magnitude of applied voltage from -50 mV to -150 mV and +50 mV to +150 mV. (c) $\Delta I/I_0$ distribution of labeled Pep A at 50, 100, and 150 mV resulting from EP force, and (d) $\Delta I/I_0$ distribution of labeled Pep A at -50, -100, and -150 mV resulting from EO flow. (e) Comparison of $\Delta I/I_0$ in EO and EP directions according to the magnitude of the negative and positive voltages, respectively. (f) The ratio of $\Delta I/I_0$ in the EO compared to EP direction according to the voltages. (g) FWHM of $\Delta I/I_0$ distributions in the EO and EP directions, according to the negative and positive voltages, respectively.

Figure 5-6. Dwell time of the labeled Pep A. (a) Dwell time of the labeled Pep A in EO and EP direction translocations according to the applied voltages. Dwell time distributions for each voltage in (b) EP direction and (c) EO direction. In the EP translocation, the dwell time is 4.4, 3.1, and 2.9 μs at 50, 100, and 150 mV, respectively. In the EO translocation, the dwell time is 5.4, 3.5, and 3.2 μs at 50, 100, and 150 mV, respectively. The dwell time at 100 and 150 mV in both directions are close to the measurement limit for the signal distortion. (~ 3.3 μs at 200 kHz low-pass filter)

Figure 5-7. Differentiation of labeled peptides. (a) $\Delta I/I_0$ distribution of Pep A' (navy),

(b) Pep B' (dark yellow), and (c) Pep C' (red) when +200 mV was applied across a 1.5–1.8 nm diameter nanopore. (d) Relative current blockade $\Delta I/I_0$ and FWHM of the $\Delta I/I_0$ distribution for three types of labeled peptides. Pep C shows two distinct $\Delta I/I_0$ distributions (C1 and C2).

Figure 5-8. Single molecule level analysis. (a) Representative events of four most typical peak shapes of nanopore translocation of labeled peptides under +200 mV voltage. (b) Schematic diagrams of the conformations of each labeled peptide under an electric field. (c) Comparison of the three types of peak shape occurrence rates in translocation events of the three labeled peptides.

Figure 5-9. Dwell time of single step events and peaks with specific conformations.

(a) Dwell time of single step events occurred in the translocation of the labeled peptides. Dwell time of $\sim 9 \mu\text{s}$ is obtained from the log-normal distribution fitting. (b) Dwell time of peak shape (1) - (3) occurred in the translocation of labeled peptides. Dwell time of $\sim 15 \mu\text{s}$ is obtained from the log-normal distribution fitting.

Figure 5-10. Peak shape occurrence ratio of the Pep B' at different applied voltages. (+100 and +200 mV) Peak shape (3) decreased to less than half at 100 mV ($\sim 18\%$) than at 200 mV ($\sim 42\%$).

CHAPTER 1.

Introduction

1.1. Nanopore technologies

1.1.1. Basic principles and history of nanopores

In the past two decades, nanopores have been extensively studied because of the advantages of label-free, high-throughput detection of biomolecules at a single-molecule level. Basically, a nanopore is a nanometer-sized pore in a thin and impermeable membrane, which is the only channel connecting two chambers in the ionic solution. When an electric potential is applied to both chambers, an ionic current is generated through the nanopore and charged particles in the solution are driven through the nanopore under the electric field. As the particles pass through the pore, blocking the ionic flow, the ionic current transiently decreases. Based on the magnitude and the duration of the current drop, physical and chemical properties of the passing particles such as size, mass and charge can be obtained. This is the basic principle of nanopore sensing which is called Coulter principle or resistive pulse sensing.¹

Based on the principle, the first nanopore was aimed at DNA sequencing, proposed by G. Church, D. Deamer, D. Branton, Richard Baldarelli and J. Kasianowicz in the 1990s.² The basic idea of nanopore DNA sequencing is as follows: When single strand DNA passes through a nanopore in a linear fashion generating a current drop, four types of nucleotides, adenine (A), thymine (T), guanine (G), and cytosine (C) would exhibit different residual ionic currents. (Figure 1-1) The first experimental results were reported by Kasianowicz *et al.*, who successfully observed the translocation of single-stranded RNA and DNA molecules, which are highly negatively charged, through α -

hemolysin nanopore of 1.4 nm pore diameter.³ While both chambers of the nanopores are filled with 1 M KCl electrolyte, polyuridylic acid (poly[U]) is added to the *cis* side. When a potential of -120 mV is applied to the *cis* chamber, translocations of negatively charged poly[U] through the α -hemolysin nanopore were observed as transient current drops and the blockade lifetimes according to the length of poly[U] and the applied potential were analyzed (Figure 1-2).

In the early days, biological nanopores, α -hemolysin and *Mycobacterium smegmatis* porin A (MspA), which naturally have nanopore structure were mainly used. These nanopores have advantages of reproducible pore size, biological compatibility, and low noise property and are used for a wide range of translocation experiments. However, the biological nanopores are not suitable for translocation of double-stranded DNA or proteins due to the fixed pore sizes (\sim 1.4 nm for α -hemolysin and \sim 1.2 nm for MspA). Also, they are not stable in various experimental environments such as pH, temperature, and mechanical stress, and so on.

Due to these drawbacks, solid-state nanopores have been proposed which is based on typical semiconductor device fabrication processes. The solid-state nanopores mainly use silicon nitride thin film as a nanopore membrane which is deposited on silicon substrates. Therefore, unlike their biological counterparts, solid-state nanopores are stable in various experimental environments, available for surface modifications, and have a potential for mass production. In addition, as will be described in the following section, since the nanopore is formed by using electron beam focusing of transmission electron microscopy (TEM), the diameter of the nanopore can be controlled in a nanometer precision. The pore length can also be adjusted, by controlling the deposition

time of the nanopore membrane, or by reactive ion etching. Based on the such advantages, solid-state nanopores have broadened the diversity of nanopore experiments. In the following sections, various solid-state nanopore fabrication methods and biological applications of solid-state nanopores will be introduced.

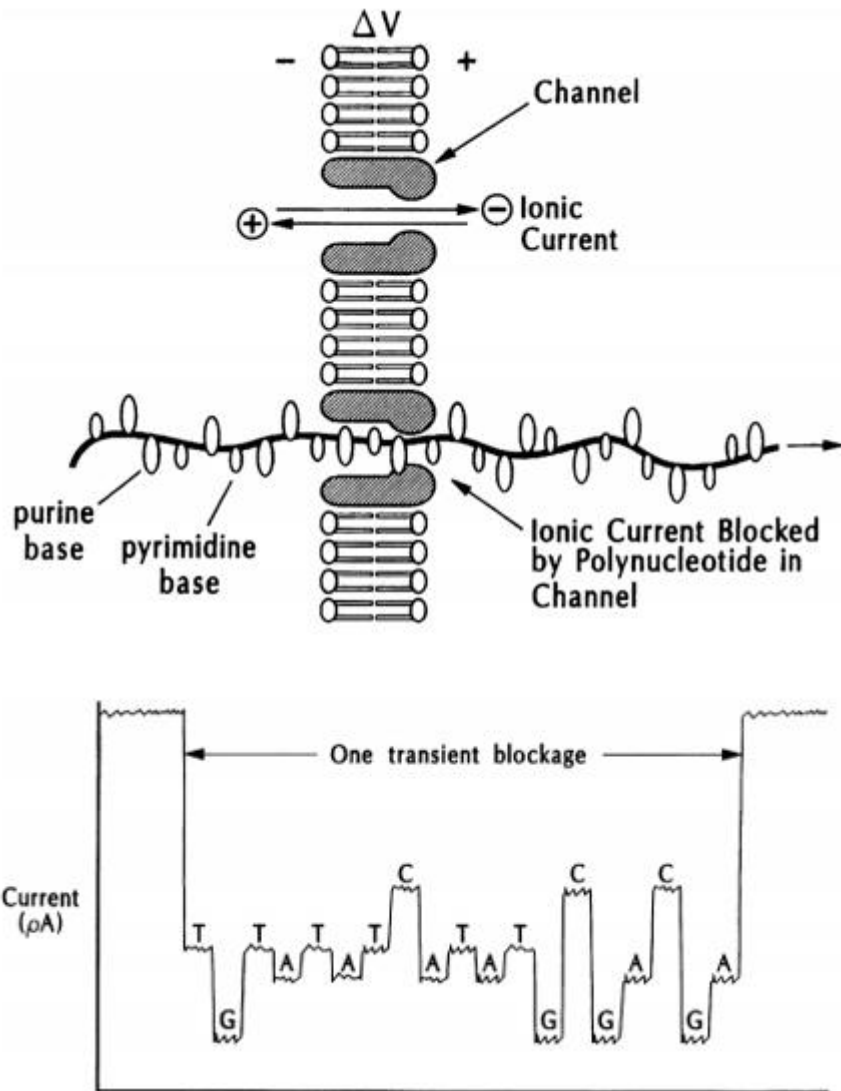


Figure 1-1. Basic idea of nanopore DNA sequencing. Adopted from ref. 2.

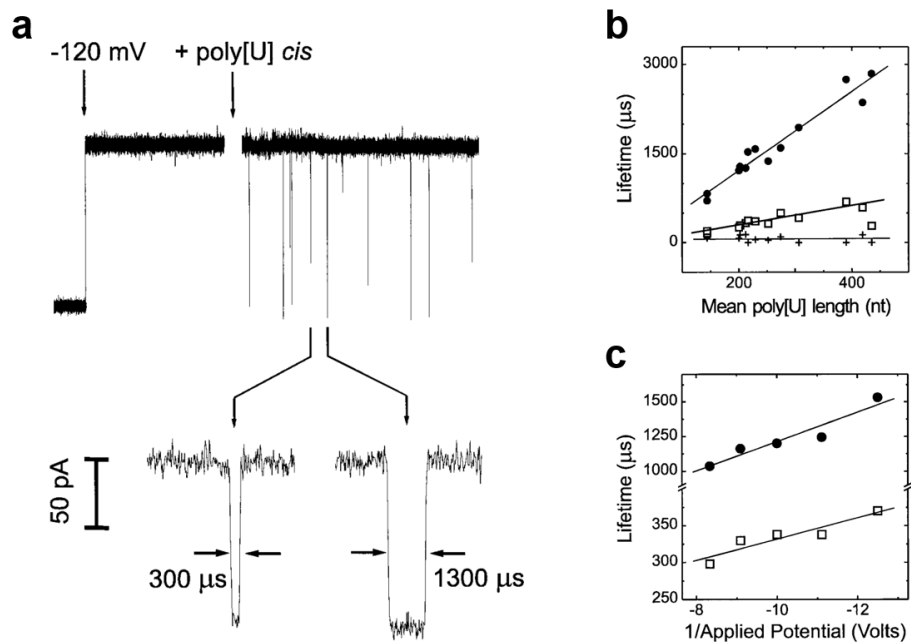


Figure 1-2. (a) Representative translocation signals of poly[U] through α -hemolysin and the blockade lifetimes according to (b) the length of poly[U] and (c) the applied potential. Adopted from ref. 3.

1.1.2. Fabrication methods of solid-state nanopores

Generally, a solid-state nanopore is fabricated in a free-standing thin membrane on a rigid substrate such as silicon, using a well-established semiconductor processes. Due to its high chemical, mechanical and thermal stability, silicon nitride is the most commonly used nanopore membrane material. Solid-state nanopore fabrication methods can be classified into three methods as follows. In 2001, the first solid-state nanopore was developed by Li *et al*, using focused ion beam (FIB).⁴ A free-standing Si_3N_4 membrane was deposited on a Si substrate and a low energy ion beam was applied to form a nanopore. This is basically a method of forming a nanopore by sputtering atoms of an Si_3N_4 membrane with an ion beam, which the authors called “ion-beam sculpting”. As shown in Figure 1-3, it is a feedback-controlled method by detecting a passing ion through the nanopore while applying a low energy ion beam to the membrane.

In 2003, Storm *et al*. developed a method of forming nanopores with direct visual feedback on SiO_2 membrane using electron beam focusing of TEM (Figure 1-4).⁵ This method has advantages of simplification of system and real-time observation of the size and shape of nanopore, compared to the FIB method described above. In addition, nanopore expansion or contraction can be controlled in nanometer precision, depending on the ratio of the thickness and diameter of the nanopore,⁵ and electron beam density (Figure 1-5).⁶ Because of these advantages, TEM poring is still the most widely used solid-state nanopore fabrication method

However, nanopore fabrication by TEM is not suitable for mass production due to

time-consuming, low-throughput, and TEM is not easily accessible to many researchers. Recently, due to these limitations, a method of forming nanopores using dielectric breakdown has been proposed.⁷⁻⁸ This method generates a high electric field by applying a voltage to the insulating membrane contained in the electrolyte solution, and induces a dielectric breakdown of the membrane (Figure 1-6). The leakage current that occurs during poring can be measured, and the pore creation can be detected in real time. In addition, when the ionic current reaches the desired level, the voltage can be turned off and the pore diameter of the desired size can be obtained as in TEM poring.

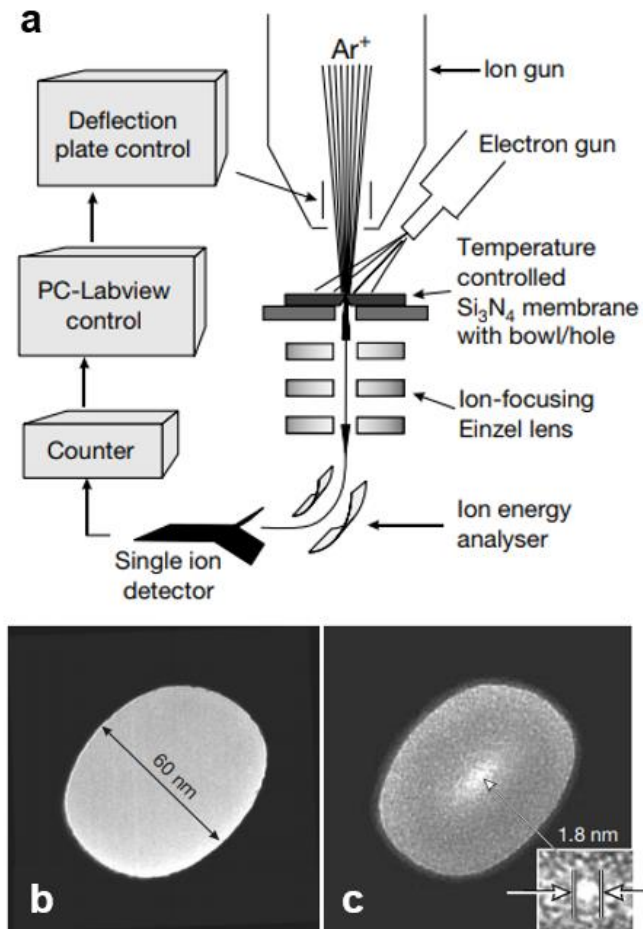


Figure 1-3. (a) Feedback-controlled ion-beam sculpting method. (b) TEM image of ~60 nm diameter pore made by FIB in a 500 nm Si_3N_4 membrane. (c) TEM image of the nanopore after ion-beam exposure. Adopted from ref. 4.

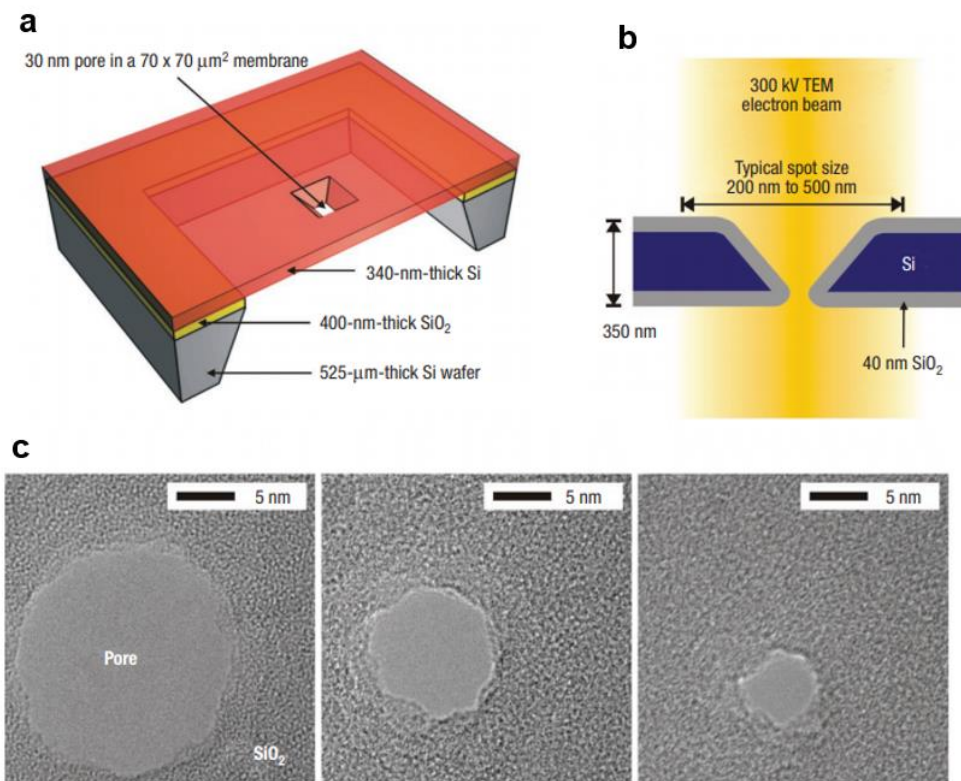


Figure 1-4. (a) A schematic diagram of silicon oxide nanopore device. (b) A schematic diagram of electron beam applied to a nanopore membrane. (c) TEM images of silicon oxide nanopores of various sizes formed by electron beam. Adopted from ref. 5.

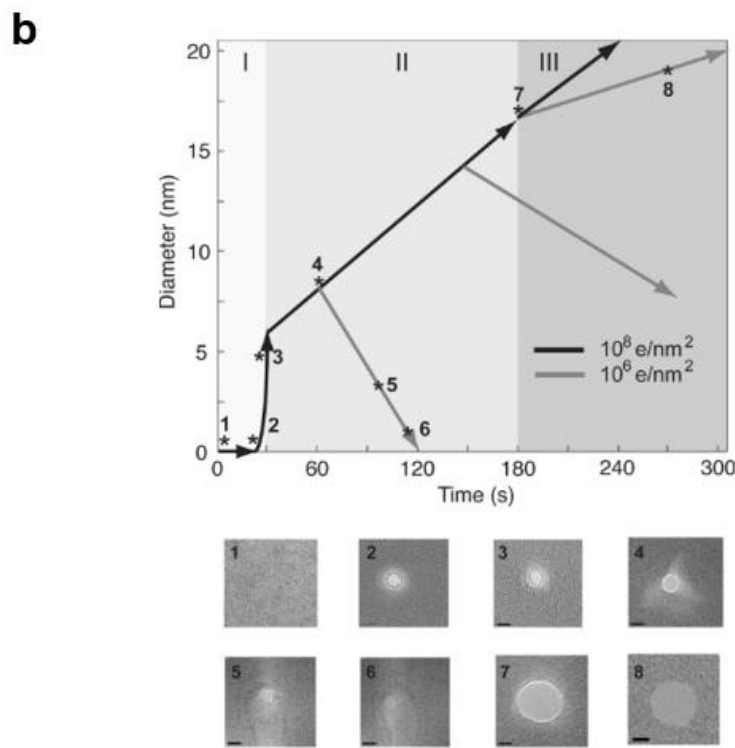
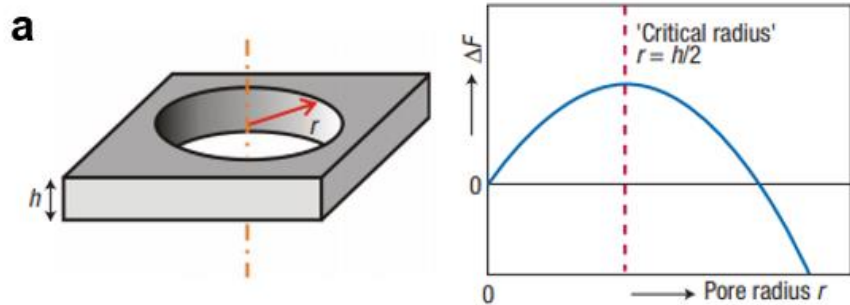


Figure 1-5. (a) Surface free energy according to the ratio of pore radius, r and thickness, h . For pores with $r < h/2$, it is preferred that the radius shrinks in terms of free energy. (b) Nanopore diameters according to electron beam density and irradiation time. Adopted from ref 5 and 6.

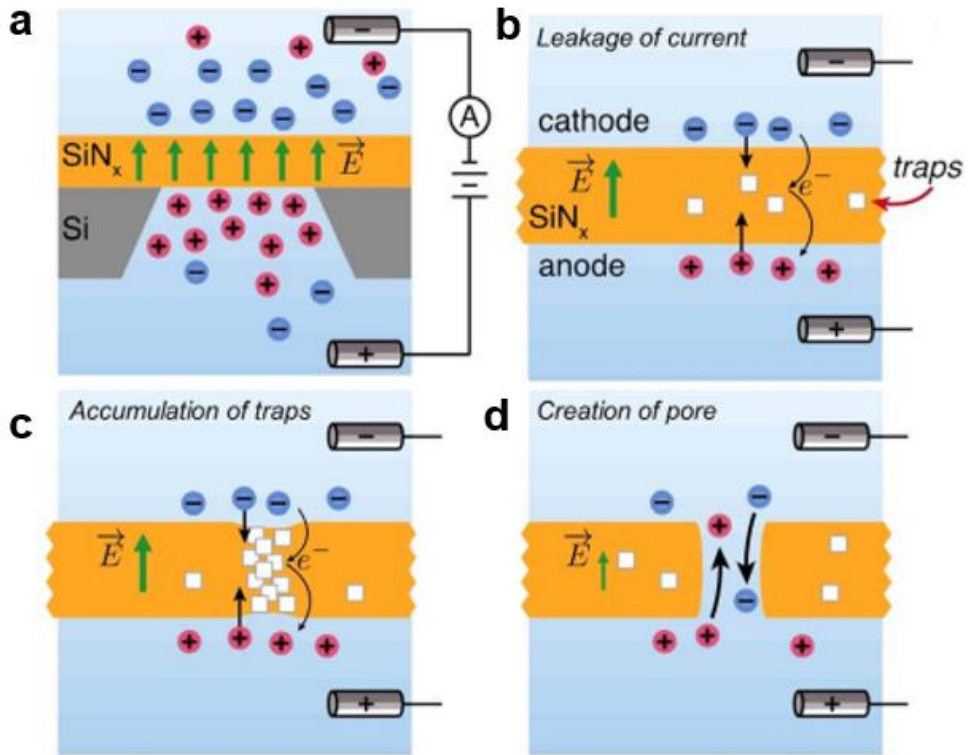


Figure 1-6. The formation processes of nanopores by dielectric breakdown. (a) An electric field is formed inside the membrane due to the application of electric potential on both sides of the silicon nitride membrane. (b) Leakage current generation due to trap-assisted tunneling of ions at the membrane surfaces. (c) A localized conductive path is generated by accumulation of traps. (d) Nanopore formation. Adopted from ref. 7.

1.1.3. Biological applications of solid-state nanopores

In the early days, solid-state nanopore researchers observed translocations of double-stranded DNA(dsDNA) which is impossible to be passed through biological nanopores. Li *et al.* observed the event configurations from the translocation of dsDNA through a SiN nanopore of ~10 nm diameter.⁹ The detected events are classified as single-level events and multi-level events based on the event configuration, from which linear and folded translocations of dsDNA could be identified (Figure 1-7). In the same way, observing the events shape of single-stranded DNA(ssDNA) through the nanopore, it was confirmed that the solid-state nanopores could function as a microscope for small molecules.¹⁰ In addition, various studies on the physics of DNA translocation through solid-state nanopores, the dominant effect of pore diameter on DNA nanopore translocation speed,¹¹ the exponential dependency of DNA length and translocation time,¹² and current increase when DNA passes through the nanopore at low salt concentration.¹³

On the other hand, since the fundamental goal of nanopore technology was DNA sequencing, there were studies to distinguish different DNA homopolymers. Lee *et al.* have focused on noise reduction for DNA sequencing using solid-state nanopores.¹⁴ They dramatically lowered the dielectric noise in the high frequency region of the noise source by replacing the nanopore substrate material from silicon to quartz. As a result, they have successfully developed low noise solid-state nanopores with sub-10 pA noise levels at 1 M potassium chloride, 10 kHz low-pass filter, which is comparable to biological nanopores. Using this low noise nanopore device, it was possible to

distinguish three different 40-nt ssDNA homopolymers (A, T, and C) passing through the solid-state nanopores by the current drop amplitude, and it was also successful to obtain characteristic signals from the mixture of poly A and poly T (Figure 1-8). Venta *et al.* also succeeded in distinguishing ssDNA homopolymers using solid-state nanopores.¹⁵ A 5 μm thick SiO_2 layer was deposited to lower the nanopore chip capacitance to reduce electrical noise and 4 MHz high-bandwidth low-noise voltage-clamp amplifier improved the detecting accuracy. As a result, three types of DNA homopolymers of poly (dA)₃₀, poly (dC)₃₀, and poly (dT)₃₀ could be distinguished by nanopore current drop (Figure 1-9).

Unlike biological nanopores, which have fixed pore size, solid-state nanopores have advantage of being able to analyze biomolecules of various sizes due to the pore size controllability. For example, various proteins, protein-protein interactions, and DNA-protein interactions can be analyzed at the single-molecule level. It was reported that the relative surface charge and dimension of proteins passing through the silicon nitride nanopores can be identified. This result was obtained from the amplitude, time duration, and integral of current blockages that occurs when the proteins pass through the nanopores (Figure 1-10).¹⁶ It has also been reported that under an electric field applied to a solid-state nanopore, as the magnitude of field increases, the proteins are stretched and unfolded inside the nanopore (Figure 1-11).¹⁷⁻¹⁸

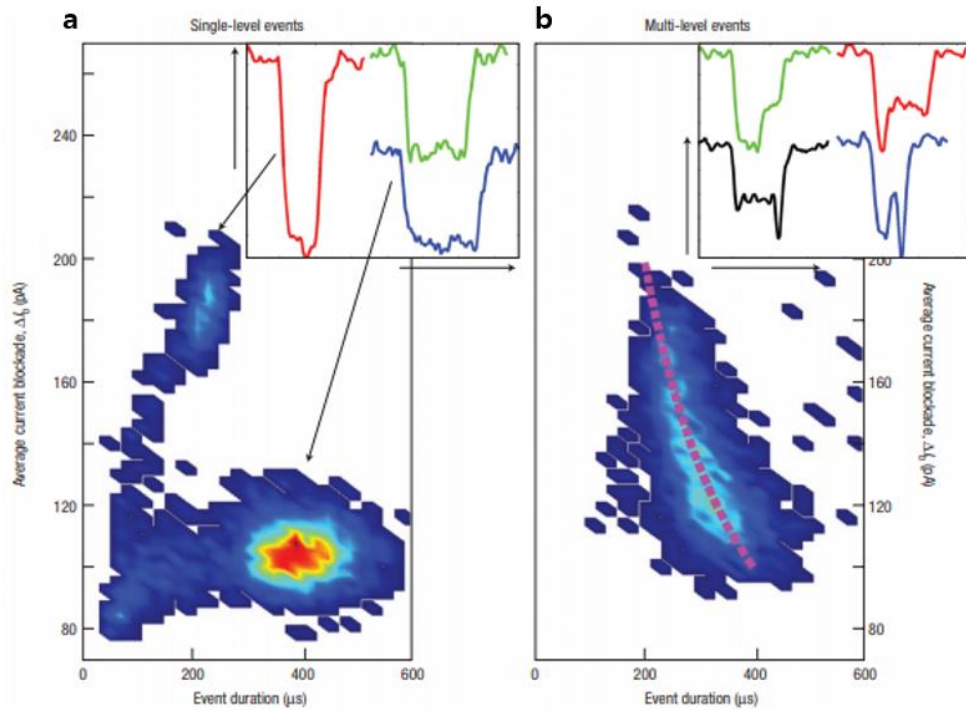


Figure 1-7. Scatter plots of dsDNA passing through a 10 nm nanopore events of (a) simple events with a single blockade level and (b) complex events. Adopted from ref. 9.

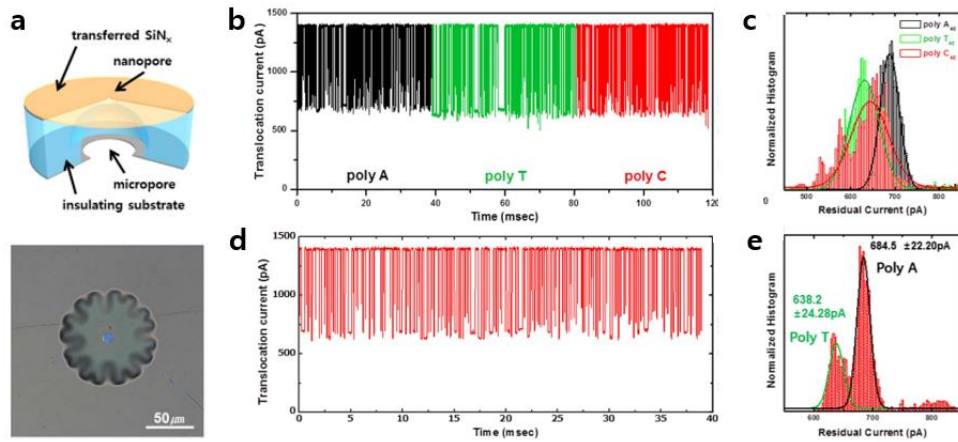


Figure 1-8. (a) A schematic diagram of quartz-based low noise solid-state nanopore and optical microscope image of the nanopore device. (b) Concatenated traces of translocation of poly A, T, and C. (c) Histogram of the residual currents of poly A, T, and C. (d) Concatenated traces of translocation of mixture of poly A and T. (e) Histogram of the residual currents of the mixture of poly A and T. Adopted from ref. 14.

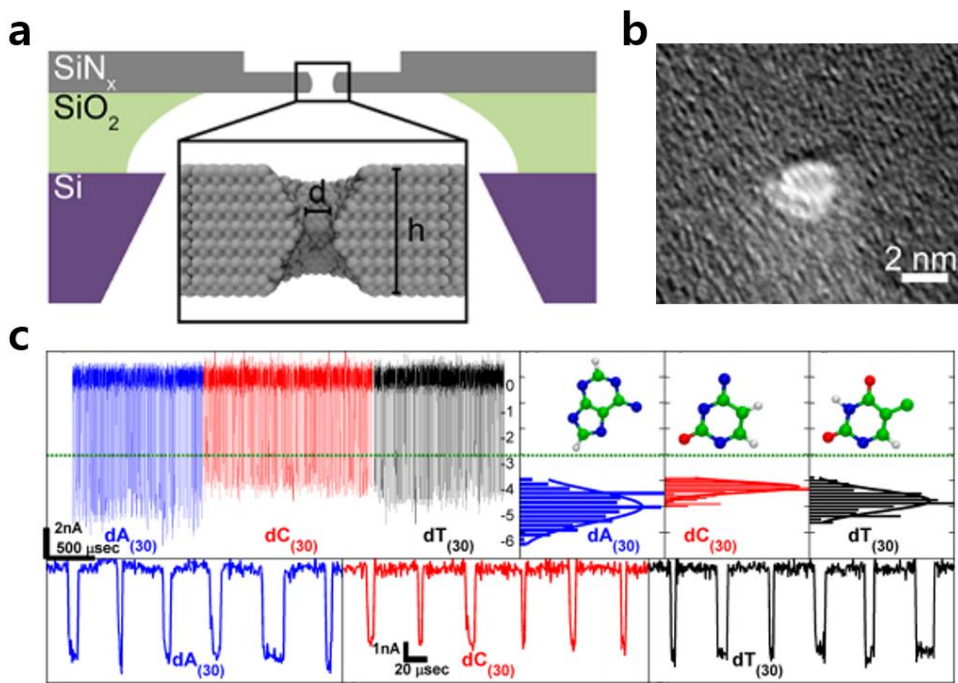


Figure 1-9. (a) Schematic of the silicon chip with 5 μm of SiO₂ layer inserted. (b) TEM image of a nanopore. (c) Concatenated translocation events and current drop histograms of poly(dA), poly(dC), and poly(dT). Adopted from ref. 15.

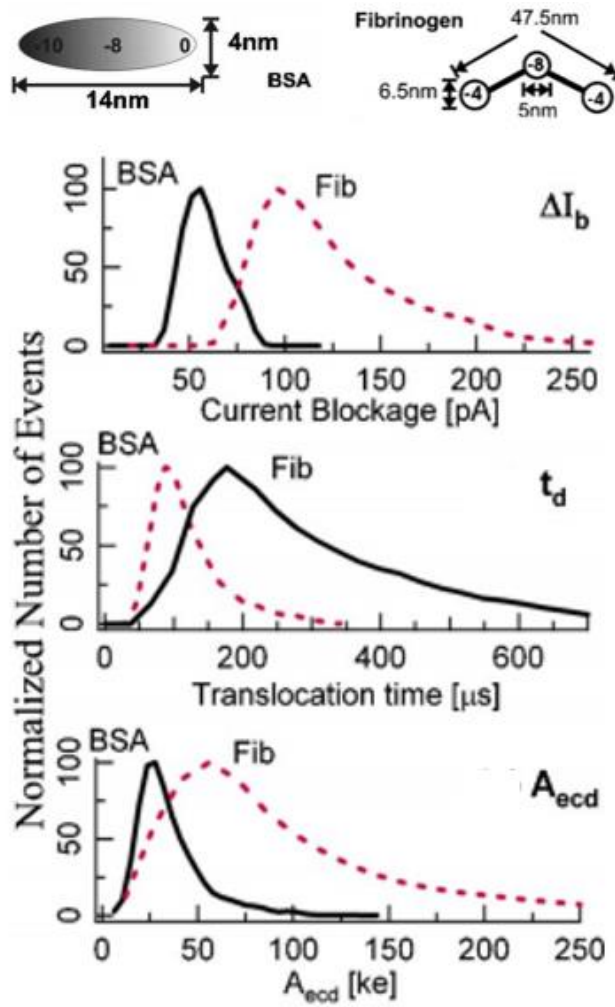


Figure 1-10. Schematic diagrams of a BSA and a fibrinogen proteins and their nanopore translocation current blockade, dwell time, and ECD (event charge deficit) histograms. Adopted from ref. 16.

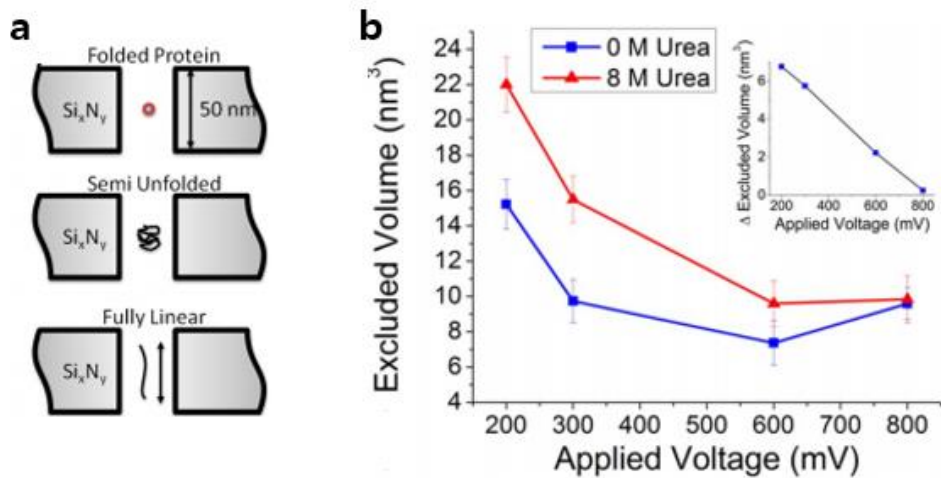


Figure 1-11. (a) Schematic drawing of protein states during nanopore translocation through silicon nitride nanopores. (b) Excluded volume generated when the proteins pass through the nanopore. Inset: the difference in excluded volume depending on the presence or absence of urea. Adopted from ref. 17.

In addition to single proteins, complex interactions between proteins can be identified by using solid-state nanopores. The changes in nanopore signal can be detected mainly by the increase of total volume due to binding of proteins, which can be utilized in understanding protein functions in human body, drug screening, and immunoassays. Uram *et al.* demonstrated the ability to detect label-free, non-destructive antibody-virus interactions with solid-state nanopores (Figure 1-12).¹⁹ They observed that as the virus binds to the antibody, the total volume became larger and the current drop through the nanopore increased. Beyond simply observing the increase in volume due to binding, Freedman *et al.* analyzed the various binding states of gp120 and anti-gp120 antibodies through signal differences in the solid-state nanopores.²⁰ Two distinct distributions were found in the histogram of nanopore current drop, and these distributions were thought to be as the result of antibody monomer or antibody dimers, respectively (Figure 1-13). In addition, as the applied voltage increased, the large current drop portion was decreased, and the unbound of proteins was detected in real time. This results showed the possibility of sensitive analysis of protein-protein interaction using solid-state nanopores.

Kwak *et al.* demonstrated that solid-state nanopores can be a new and efficient methodology of drug screening.²¹ They confirmed the suitability of the drug to interfere with the binding of p53TAD, an anticancer therapeutic p53 transactivation domain, and its inhibitory molecule, mouse double minute 2(MDM2). Here, since Nutlin-3 binds to MDM2, it functions as a drug by acting as a competitor of p53TAD-MDM2 binding. The possibility of label-free and high-throughput drug screening using solid-state nanopore was confirmed by observing the frequency difference of the

nanopore events of p53TAD-MDM2 depending on the presence or absence of Nutlin-3 (Figure 1-14). As described above, solid-state nanopores can be used for various analysis of small biomolecules such as DNA and protein, based on advantages such as label-free, high-throughput, high sensitivity at the single molecule level, and desirable dimensions of the nanopore.

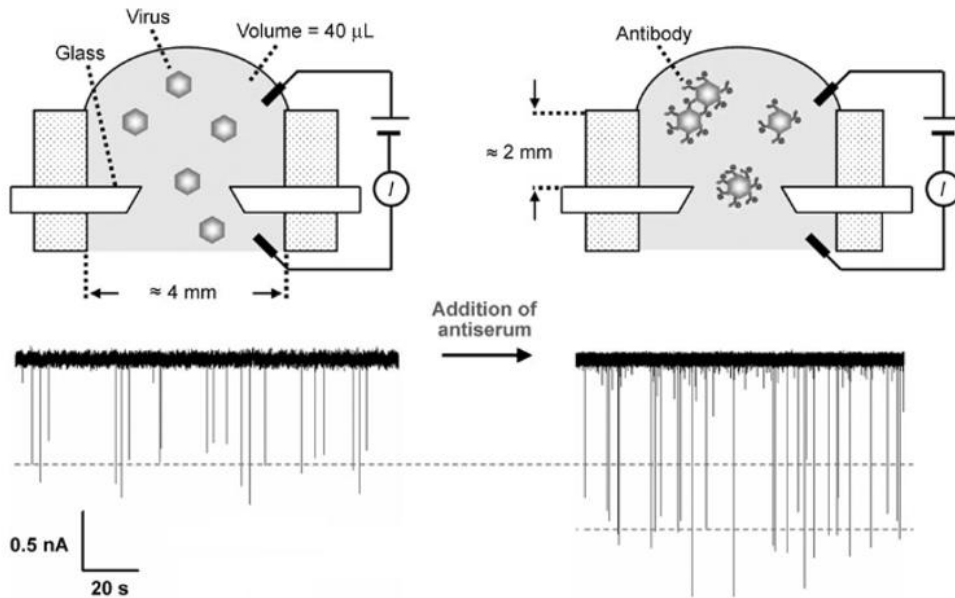


Figure 1-12. Detection of virus-antibody interaction using solid-state nanopores. The increase in volume due to antibody binding is reflected in the nanopore current drop amplitude. Adopted from ref. 19.

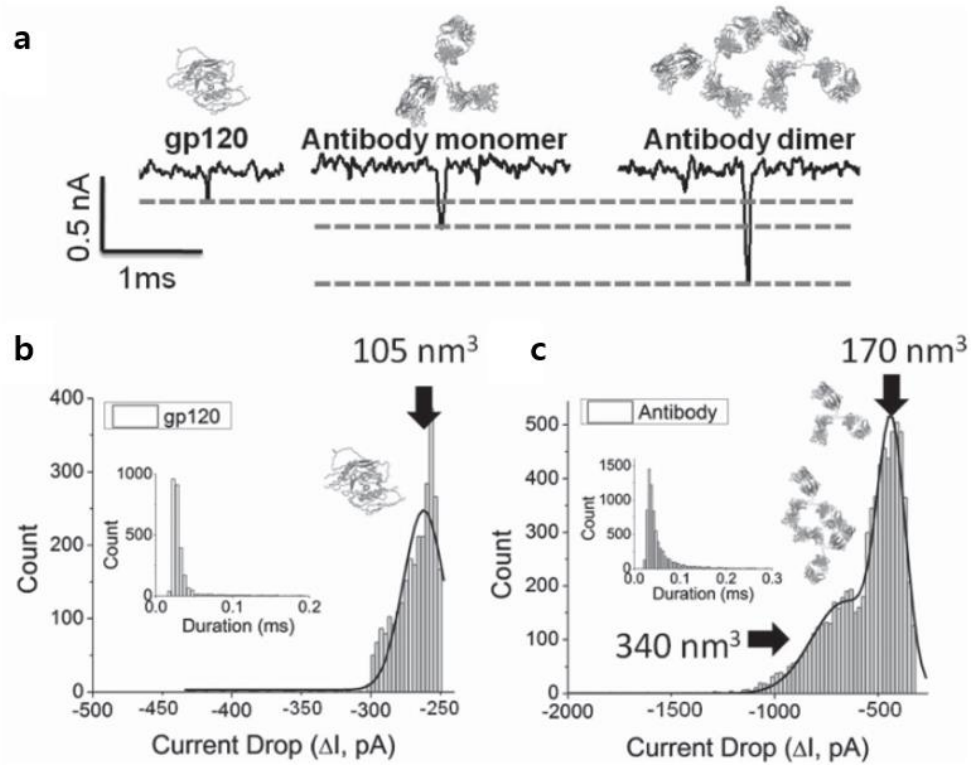


Figure 1-13. (a) Representative nanopore signals of gp120 protein, antibody monomer, and antibody dimer. (b) The current drop histogram of gp120 showing a single peak. (c) The current drop histogram of antibody showing two distinct peaks. Adopted from ref. 20.

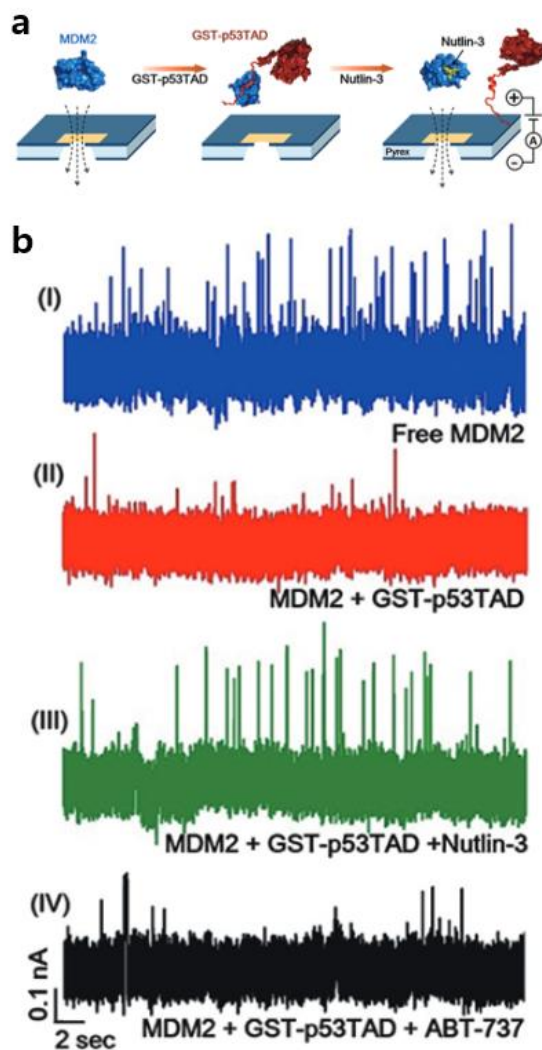


Figure 1-14. (a) Schematic diagram of nanopore drug screening. Nanopore translocation of p53-MDM2 complex is determined by Nutlin-3 binding. (b) Example nanopore current traces of (I) free MDM2, (II) MDM2 + GST-p53TAD, (III) MDM2 + GST-p53TAD + Nutlin-3, and (IV) MDM2 + GST-p53TAD + ABT-737. Adopted from ref. 21.

1.2. Issues in solid-state nanopores

1.2.1. Spatial resolution

The nanopore signal is determined by how much of the biomolecule inside the pore blocks the ionic current flow. For example, in the case of DNA translocation, the thicker the nanopore membrane, the more nucleotides contribute to the total current drop at the same time and it is more difficult to discriminate signals between the nucleotides. Theoretically, nanopore membrane thickness of 0.34 nm is required for DNA sequencing. In addition, as the membrane thickness decreases, the resistance of the pore decreases and thus the magnitude of the signal increases, resulting in a greater signal-to-noise ratio. Therefore, for better sensitivity of nanopores, studies have been actively conducted to reduce membrane thickness.

First, we introduce the results of reducing thickness of silicon nitride which is most commonly used as solid-state nanopore membrane. Lee *et al.* used a method of transferring a silicon nitride membrane to a low-noise nanopore substrate.¹⁴ Silicon nitride film was deposited on the metal layer by plasma enhanced chemical vapor deposition (PECVD) to a thickness of 5 nm, 10 nm, and 20 nm, and then transferred to a nanopore substrate. As can be seen in Figure 1-15, as the nanopore thickness decreases, the magnitude of the current drop signal is noticeably improved. There was an approach to reduce the thickness of pre-deposited silicon nitride membrane through a well-controlled reactive ion etching (RIE).²² In this method, e-beam lithography is used to define the SiN region to be etched, and then the thickness of the SiN is reduced by RIE

using SF₆ gas. The etch rate was about 1.0 nm/s, and the SiN thickness can be controlled quite accurately even at the sub-10 nm thickness (Figure 1-15). The obtained SiN membrane had a minimum thickness of ~6 nm and a maximum signal-to-noise ratio of ~46. On the other hand, a scanning transmission electron microscope (STEM) is used to reduce the thickness of the SiN membrane to 2 nm or less.²³ In this method, since the N atom is sputtered faster than the Si atom by the electron, an a-Si nanopore can be formed. Through this, a nanopore with a minimum thickness of ~1.4 nm and a diameter of ~2.5 nm was fabricated and the translocation signals of dsDNA can be successfully obtained (Figure 1-15).

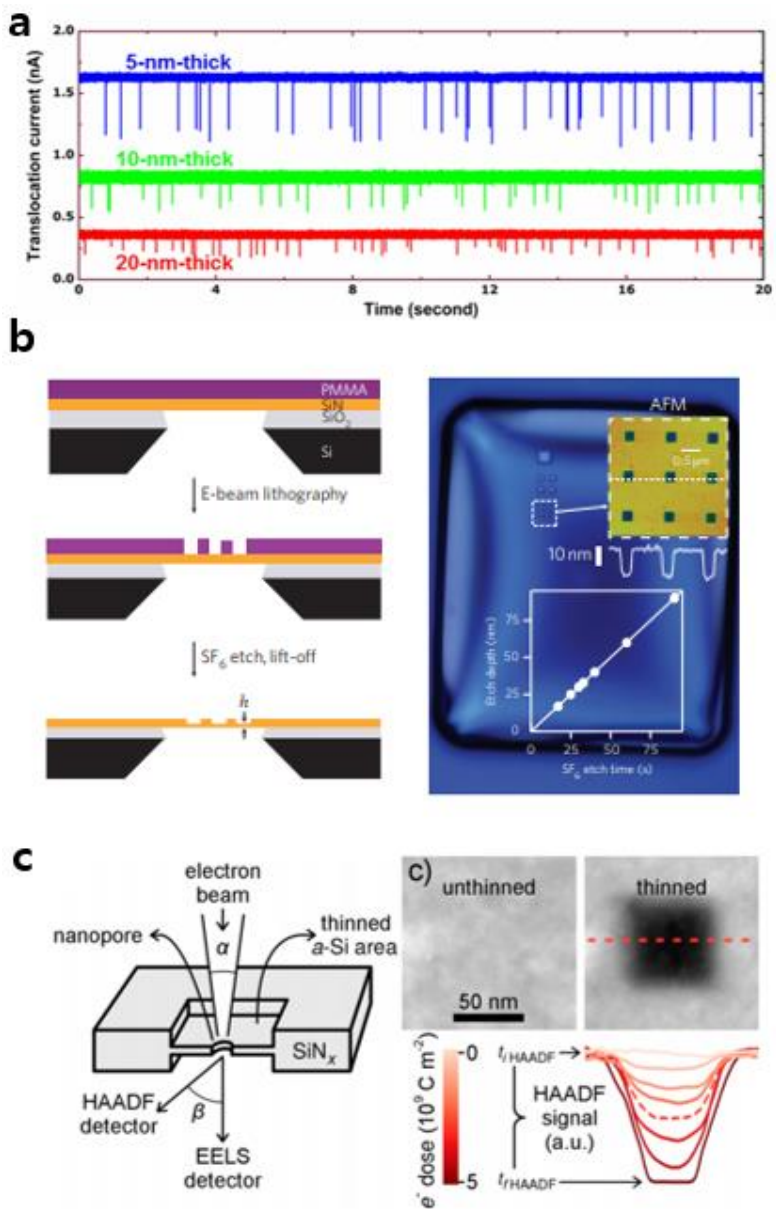


Figure 1-15. (a) Ionic current traces of ssDNA translocation through 5 nm, 10 nm, and 20 nm thick SiN nanopores. (b) Thinning SiN nanopore membrane using SF₆ RIE process and its etch depth versus etch time. (c) Thinning of SiN nanopore membrane by electron irradiation. Adopted from ref. 14, 22, and 23.

Two-dimensional (2D) materials is a single-layer, atomically thin, and is the best material for solid-state nanopore membranes. Graphene has advantages such as robustness, chemical stability, and an excellent electric conductor, and its potential as a nanopore membrane has been verified first among 2D materials. Cees Dekker group first obtained DNA translocation signals through graphene nanopores.²⁴ After graphene flakes were transferred to a silicon nitride membrane with a micro-sized pore, a graphene nanopore was formed using the conventional TEM poring method. Although the noise characteristic of the graphene nanopore was worse than typical silicon nitride membrane due to fluctuation and pinhole issues, the DNA translocation signals were sufficiently obtained (Figure 1-16).

Park *et al.* demonstrated that another 2D material, boron nitride (BN), can be as a nanopore membrane.²⁵ On a pyrex-based low noise nanopore substrate, they fabricated a silicon nitride layer with an opening diameter of less than 100 nm and transferred the BN membrane onto the layer. The BN nanopore was fabricated in a multi-layer structure rather than a single layer, resulting in improvement of noise issues due to the membrane fluctuation and pinholes. The signal-to-noise ratio(SNR) of dsDNA translocation could be achieved up to ~55 in 100 kHz low-pass filter. (Figure 1-16) Another 2D material, molybdenum disulfide (MoS₂) was also proved as a nanopore membrane.²⁶ MoS₂ nanopore showed a SNR larger than 10 for dsDNA translocations, and had the advantage of no hydrophobic interaction with biomolecules, which was a problem in graphene nanopores. (Figure 1-16)

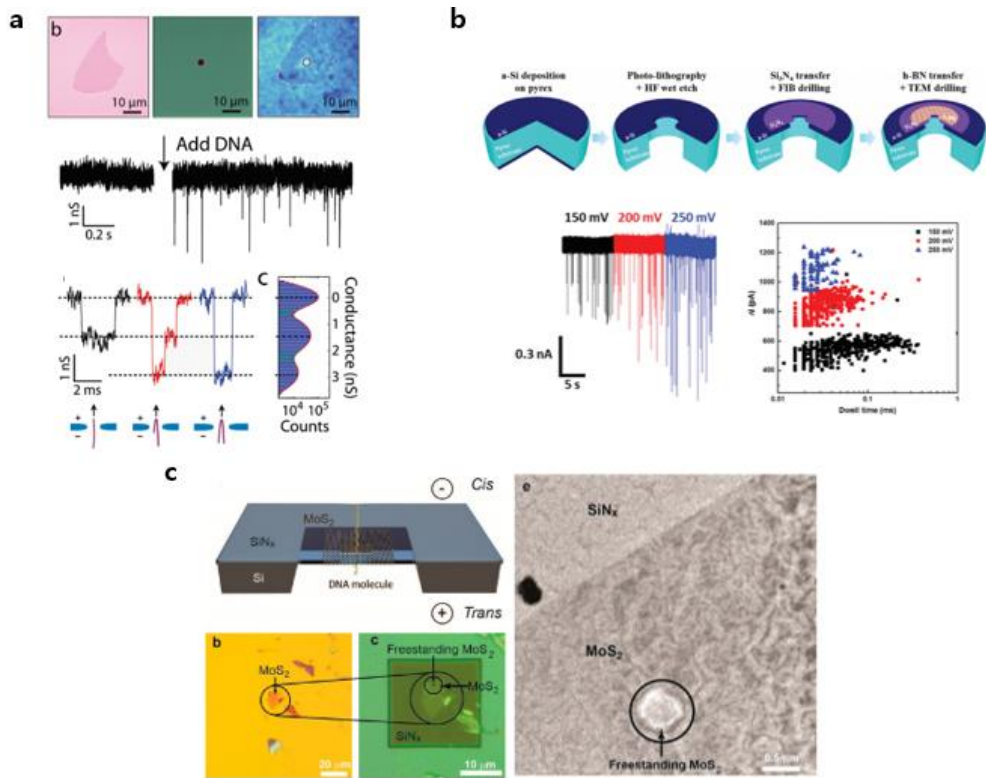


Figure 1-16. (a) Optical microscope images of graphene nanopore membrane on SiN layer and DNA translocation signals of the graphene nanopore. (b) The fabrication processes of BN nanopore and the current traces of DNA translocation. (c) Schematic diagram of MoS₂ nanopore chip, and optical and TEM images of MoS₂ nanopore structure. Adopted from ref. 24, 25, and 26.

1.2.2. Signal to noise ratio

Even if biomolecules pass through a very sensitive nanopore membrane, it would be meaningless if the measured signals were buried in noises. In nanopore measurements, ionic current noise is inevitably caused by several reasons, which affects the reliability of the measurement. The signal-to-noise ratio (SNR), typically expressed as $\Delta I/I_{\text{RMS}}$, is an important factor in the reliability of nanopore measurements, where ΔI is the current drop magnitude and I_{RMS} is the root-mean-square noise of the ionic current.

In particular, ionic current noise has become a major limitation in solid-state nanopores, rather than in biological nanopores. In order to reduce the ionic current noise, it is necessary to analyze the noise sources. The noise sources can be analyzed by obtaining the power spectral density (PSD) according to the frequency, through the fast Fourier transform (FFT) (Figure 1-17).

At low frequencies, Flicker noise which is proportional to $1/f$ is dominant. This noise is known to be caused by the charge carrier flux or fluctuation of the flux, and is expressed as equation 1 by Hooge's relation:

$$\frac{S_{\text{Flicker}}}{I^2} = \frac{A}{f} = \frac{\alpha}{N_c f} \quad (1)$$

where I is the ionic current, A is the noise power, f is the frequency, α is the Hooge parameter, and N_c is the number of charge carriers.²⁷ Thermal noise, another source of low frequency noise, is related to the resistance of the pore, and expressed as equation 2:

$$S_{Thermal} = \frac{4kT}{R} \quad (2)$$

where k is the Boltzmann's constant, T is the temperature, and R is the resistance of nanopore.²⁸ Thermal noise is frequency independent and is generally insignificant compared to other noise sources due to high resistance of the nanopore.

At the high frequency regime above 1 kHz, dielectric noise and amplifier noise are dominant. Since the amplifier noise mainly acts at a very high frequency above 100 kHz, it does not have much influence on typical nanopore measurements using 10 or 100 kHz low pass filters. The dielectric noise is related to the capacitance of the nanopore chip and is expressed as equation 3:

$$S_{Dielectric} = 4kTDC_D(2\pi f) \quad (3)$$

where k is Boltzmann's constant, T is the temperature, D is the loss tangent, and C_D is the chip capacitance.²⁹ Since the total ionic current noise is calculated as the integral of the entire frequency domain, the dielectric noise that acts in the high frequency is responsible for a very large portion. Here we present some attempts of dielectric noise reduction in solid-state nanopores, which are usually determined by the nanopore device fabrication method or the nanopore chip materials.

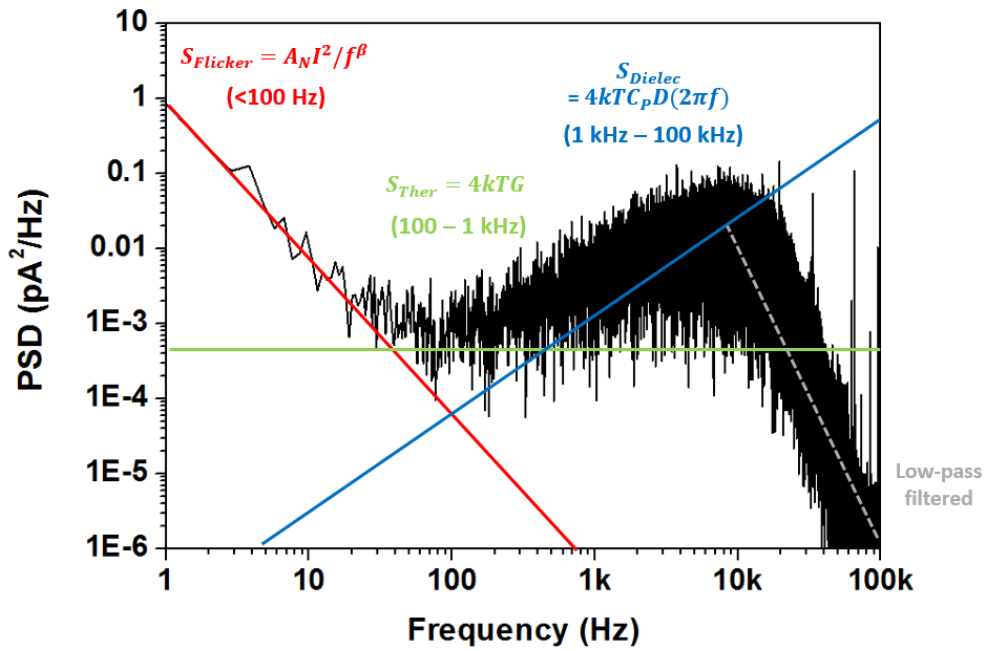


Figure 1-17. An example noise power spectral density versus frequency. Four different noise sources are shown according to the frequency regime.

To reduce the chip capacitance, polydimethylsiloxane (PDMS), which has a low dielectric constant of ~ 2.7 ,³⁰ was coated on the nanopore chip except the nanopore membrane area.³¹ As a result, the noise PSD showed that the PDMS covered nanopore chip had much lower dielectric noise than the bare Si based nanopore (Figure 1-18a). With the same principle, a 5 μm thick SiO_2 layer was inserted between the Si substrate and the SiN nanopore membrane or a glass layer was integrated to reduce the chip capacitance³²⁻³³ (Figure 1-18b).

Lee *et al.* developed a fabrication process for replacing the substrate material of a nanopore chip from silicon to quartz.¹⁴ A 200 nm thick a-Si was deposited on the quartz substrate using LPCVD. Through the photolithography and SF_6 RIE, the opening of the a-Si layer with a diameter of 5 μm on one side and a diameter of 100 μm on the other side were formed. The quartz wafer was then etched with a hydrofluoric acid (HF) solution, and a quartz substrate with a 5 μm opening was obtained (Figure 1-18c). On this substrate, a PECVD SiN membrane was transferred, and the thickness of the SiN could be obtained to a minimum of 5 nm. This quartz nanopore chip effectively reduced I_{RMS} to within 10 pA at 10 kHz low pass filter and significantly improved the signal-to-noise ratio using a 5 nm thick nanopore.

Figure 1-18d shows an example of using a glass nanocapillary as a low noise nanopore.³⁴ Glass nanocapillary nanopores have excellent noise characteristics by lowering dielectric noise and are superior in fabrication efficiency compared to Si based

nanopore chips. The tip diameter is initially several hundred nanometers, but can be reduced to less than 20 nm using scanning electron microscope (SEM). DNA translocation events were observed through the nanocapillary and showed a better signal-to-noise ratio than Si-based nanopores. However, unlike the conventional TEM poring method, it is difficult to fabricate a nanopore having a diameter of less than 10 nm in the nanocapillary, and the thickness of the sensing zone cannot be clearly defined.

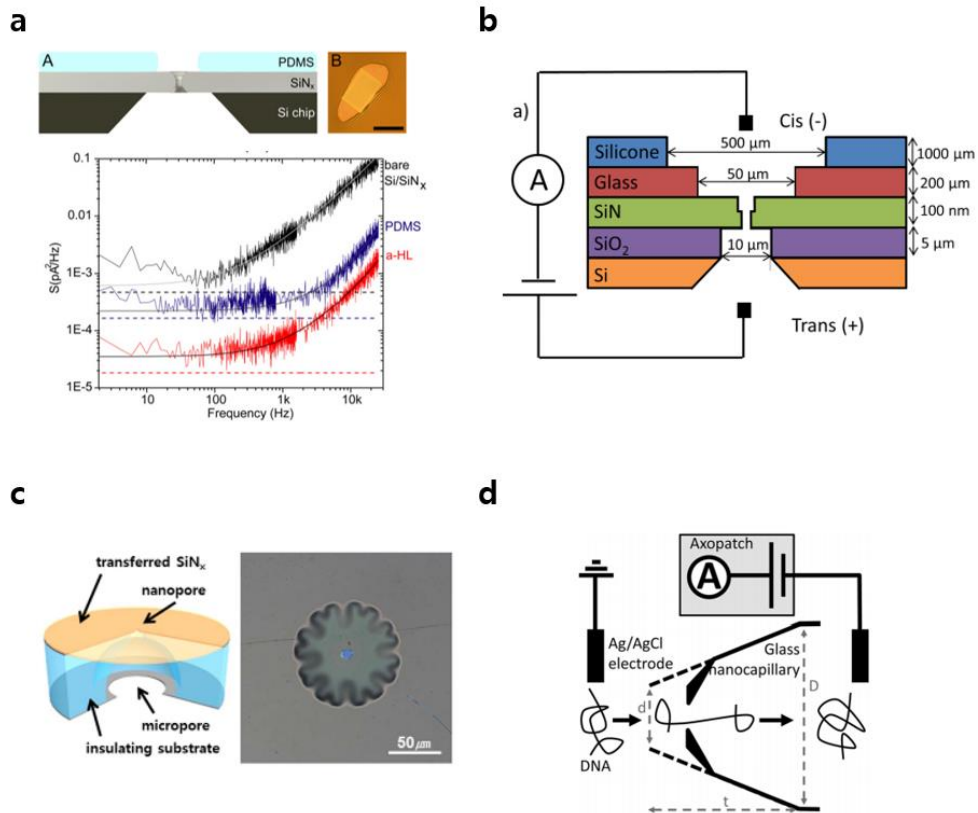


Figure 1-18. Reduction in dielectric noise of solid-state nanopores. (a) A schematic diagram of PDMS coated nanopore chip and a noise PSD plot of a bare Si/SiN nanopore, a PDMS coated nanopore, and an alpha-hemolysin nanopore. (b) A schematic diagram of a nanopore chip with a 5 μm SiO₂ layer inserted and a thick glass layer integrated. (c) A schematic diagram of a quartz-based nanopore device and an optical microscope image. (d) A schematic diagram of glass nanocapillary nanopore. Adopted from ref. 14, 31, 32, 33, and 34.

References

1. Coulter, W. H., Means for counting particles suspended in a fluid. Google Patents: 1953.
2. Church, G.; Deamer, D. W.; Branton, D.; Baldarelli, R.; Kasianowicz, J., Characterization of individual polymer molecules based on monomer-interface interactions. Google Patents: 1998.
3. Kasianowicz, J. J.; Brandin, E.; Branton, D.; Deamer, D. W., Characterization of individual polynucleotide molecules using a membrane channel. Proceedings of the National Academy of Sciences 1996, 93 (24), 13770-13773.
4. Li, J.; Stein, D.; McMullan, C.; Branton, D.; Aziz, M. J.; Golovchenko, J. A., Ion-beam sculpting at nanometre length scales. Nature 2001, 412, 166.
5. Storm, A. J.; Chen, J. H.; Ling, X. S.; Zandbergen, H. W.; Dekker, C., Fabrication of solid-state nanopores with single-nanometre precision. Nature Materials 2003, 2, 537.
6. Kim, M. J.; Wanunu, M.; Bell, D. C.; Meller, A., Rapid Fabrication of Uniformly Sized Nanopores and Nanopore Arrays for Parallel DNA Analysis. Advanced Materials 2006, 18 (23), 3149-3153.
7. Kwok, H.; Briggs, K.; Tabard-Cossa, V., Nanopore Fabrication by Controlled Dielectric Breakdown. PLOS ONE 2014, 9 (3), e92880.

8. Yanagi, I.; Akahori, R.; Hatano, T.; Takeda, K.-i., Fabricating nanopores with diameters of sub-1 nm to 3 nm using multilevel pulse-voltage injection. *Scientific Reports* 2014, 4, 5000.
9. Li, J.; Gershow, M.; Stein, D.; Brandin, E.; Golovchenko, J. A., DNA molecules and configurations in a solid-state nanopore microscope. *Nature Materials* 2003, 2, 611.
10. Fologea, D.; Gershow, M.; Ledden, B.; McNabb, D. S.; Golovchenko, J. A.; Li, J., Detecting Single Stranded DNA with a Solid State Nanopore. *Nano Letters* 2005, 5 (10), 1905-1909.
11. Wanunu, M.; Sutin, J.; McNally, B.; Chow, A.; Meller, A., DNA Translocation Governed by Interactions with Solid-State Nanopores. *Biophysical Journal* 2008, 95 (10), 4716-4725.
12. Storm, A. J.; Storm, C.; Chen, J.; Zandbergen, H.; Joanny, J.-F.; Dekker, C., Fast DNA Translocation through a Solid-State Nanopore. *Nano Letters* 2005, 5 (7), 1193-1197.
13. Smeets, R. M. M.; Keyser, U. F.; Krapf, D.; Wu, M.-Y.; Dekker, N. H.; Dekker, C., Salt Dependence of Ion Transport and DNA Translocation through Solid-State Nanopores. *Nano Letters* 2006, 6 (1), 89-95.

14. Lee, M.-H.; Kumar, A.; Park, K.-B.; Cho, S.-Y.; Kim, H.-M.; Lim, M.-C.; Kim, Y.-R.; Kim, K.-B., A Low-Noise Solid-State Nanopore Platform Based on a Highly Insulating Substrate. *Scientific Reports* 2014, 4, 7448.
15. Venta, K.; Shemer, G.; Puster, M.; Rodríguez-Manzo, J. A.; Balan, A.; Rosenstein, J. K.; Shepard, K.; Drndić, M., Differentiation of Short, Single-Stranded DNA Homopolymers in Solid-State Nanopores. *ACS Nano* 2013, 7 (5), 4629-4636.
16. Fologea, D.; Ledden, B.; McNabb, D. S.; Li, J., Electrical characterization of protein molecules by a solid-state nanopore. *Applied Physics Letters* 2007, 91 (5), 053901.
17. Freedman, K. J.; Haq, S. R.; Edel, J. B.; Jemth, P.; Kim, M. J., Single molecule unfolding and stretching of protein domains inside a solid-state nanopore by electric field. *Scientific Reports* 2013, 3, 1638.
18. Talaga, D. S.; Li, J., Single-Molecule Protein Unfolding in Solid State Nanopores. *Journal of the American Chemical Society* 2009, 131 (26), 9287-9297.
19. Uram, J. D.; Ke, K.; Hunt, A. J.; Mayer, M., Submicrometer Pore-Based Characterization and Quantification of Antibody–Virus Interactions. *Small* 2006, 2 (8-9), 967-972.
20. Freedman, K. J.; Bastian, A. R.; Chaiken, I.; Kim, M. J., Solid-State Nanopore Detection of Protein Complexes: Applications in Healthcare and Protein Kinetics. *Small* 2013, 9 (5), 750-759.

21. Kwak, D.-K.; Chae, H.; Lee, M.-K.; Ha, J.-H.; Goyal, G.; Kim, M. J.; Kim, K.-B.; Chi, S.-W., Probing the Small-Molecule Inhibition of an Anticancer Therapeutic Protein-Protein Interaction Using a Solid-State Nanopore. *Angewandte Chemie International Edition* 2016, 55 (19), 5713-5717.
22. Wanunu, M.; Dadosh, T.; Ray, V.; Jin, J.; McReynolds, L.; Drndić, M., Rapid electronic detection of probe-specific microRNAs using thin nanopore sensors. *Nature Nanotechnology* 2010, 5, 807.
23. Rodríguez-Manzo, J. A.; Puster, M.; Nicolai, A.; Meunier, V.; Drndić, M., DNA Translocation in Nanometer Thick Silicon Nanopores. *ACS Nano* 2015, 9 (6), 6555-6564.
24. Schneider, G. F.; Kowalczyk, S. W.; Calado, V. E.; Pandraud, G.; Zandbergen, H. W.; Vandersypen, L. M. K.; Dekker, C., DNA Translocation through Graphene Nanopores. *Nano Letters* 2010, 10 (8), 3163-3167.
25. Park, K.-B.; Kim, H.-J.; Kim, H.-M.; Han, S. A.; Lee, K. H.; Kim, S.-W.; Kim, K.-B., Noise and sensitivity characteristics of solid-state nanopores with a boron nitride 2-D membrane on a pyrex substrate. *Nanoscale* 2016, 8 (10), 5755-5763.
26. Liu, K.; Feng, J.; Kis, A.; Radenovic, A., Atomically Thin Molybdenum Disulfide Nanopores with High Sensitivity for DNA Translocation. *ACS Nano* 2014, 8 (3), 2504-2511.

27. Smeets, R. M.; Keyser, U. F.; Dekker, N. H.; Dekker, C., Noise in solid-state nanopores. *Proceedings of the National Academy of Sciences* 2008, 105 (2), 417-421.
28. Uram, J. D.; Ke, K.; Mayer, M., Noise and bandwidth of current recordings from submicrometer pores and nanopores. *Acs Nano* 2008, 2 (5), 857-872.
29. Dimitrov, V.; Mirsaidov, U.; Wang, D.; Sorsch, T.; Mansfield, W.; Miner, J.; Klemens, F.; Cirelli, R.; Yemenicioglu, S.; Timp, G., Nanopores in solid-state membranes engineered for single molecule detection. *Nanotechnology* 2010, 21 (6), 065502.
30. Farcich, N. J.; Salonen, J.; Asbeck, P. M., Single-length method used to determine the dielectric constant of polydimethylsiloxane. *IEEE Transactions on Microwave Theory and techniques* 2008, 56 (12), 2963-2971.
31. Tabard-Cossa, V.; Trivedi, D.; Wiggin, M.; Jetha, N. N.; Marziali, A., Noise analysis and reduction in solid-state nanopores. *Nanotechnology* 2007, 18 (30), 305505.
32. Rosenstein, J. K.; Wanunu, M.; Merchant, C. A.; Drndic, M.; Shepard, K. L., Integrated nanopore sensing platform with sub-microsecond temporal resolution. *Nature methods* 2012, 9 (5), 487.
33. Balan, A.; Machielse, B.; Niedzwiecki, D.; Lin, J.; Ong, P.; Engelke, R.; Shepard, K. L.; Drndić, M., Improving signal-to-noise performance for DNA translocation in solid-state nanopores at MHz bandwidths. *Nano letters* 2014, 14 (12), 7215-7220.

34. Steinbock, L. J.; Bulushev, R. D.; Krishnan, S.; Raillon, C.; Radenovic, A., DNA Translocation through Low-Noise Glass Nanopores. *ACS Nano* 2013, 7 (12), 11255-11262.

CHAPTER 2.

Enhancement of Solid-State Nanopore Membrane

2.1. Introduction

The quartz-based low-noise nanopores introduced in Chapter 1.2.2. greatly reduced the dielectric noise and improved the sensitivity of nanopore measurements. This low noise nanopore device is fabricated by depositing a silicon nitride film on a separate substrate and transferring it to a quartz substrate with a micro-sized hole using the “fishing method”. Due to the stability of the nickel film which is a sacrificial layer during the transfer process, silicon nitride film was deposited by plasma enhanced chemical vapor deposition (PECVD) at a relatively low temperature of ~ 200 °C.

PECVD SiN is rapidly deposited at a relatively low temperature compared to LPCVD processes. Therefore, in the case of PECVD, a stoichiometric SiN film is not formed, and a SiN film with a high hydrogen content is obtained. The PECVD SiN films have poor quality in terms of the density, breakdown strength, and so on.¹⁻⁵ As a result, the PECVD SiN nanopores had several problems, such as pore expansion during measurement and vulnerability to piranha cleaning at high temperature.

In addition, during the transfer process, poly(methyl methacrylate) (PMMA) was used as a supporting layer for floating SiN film. The PMMA layer was not completely removed by acetone cleaning or annealing but left residues on the SiN surface. Figure 2-1a shows a TEM image of SiN surface with PMMA residue. Figure 2-1b is ionic current traces when DNA and DNA/protein complexes are passed through a PECVD SiN nanopore with an applied electric potential of 200 mV. The ionic current noise, IRMS was ~ 8.7 pA when only DNA passed through the nanopore, but it increased significantly to ~ 22.6 pA when DNA/protein complexes were present. When the ionic

current traces were analyzed by noise PSD, it is obvious that the increase of IRMS was caused by the increase of the flicker noise (Figure 2-1c). Several studies have reported that protein adsorption occurs on the PMMA surface.⁶⁻⁷ Considering that, it can be assumed that proteins are adsorbed to the PMMA residue on the SiN surface, resulting membrane fluctuations and increase in the flicker noise. This chapter introduces the LPCVD SiN low noise nanopore which overcomes the limitations of the PECVD SiN nanopore devices.

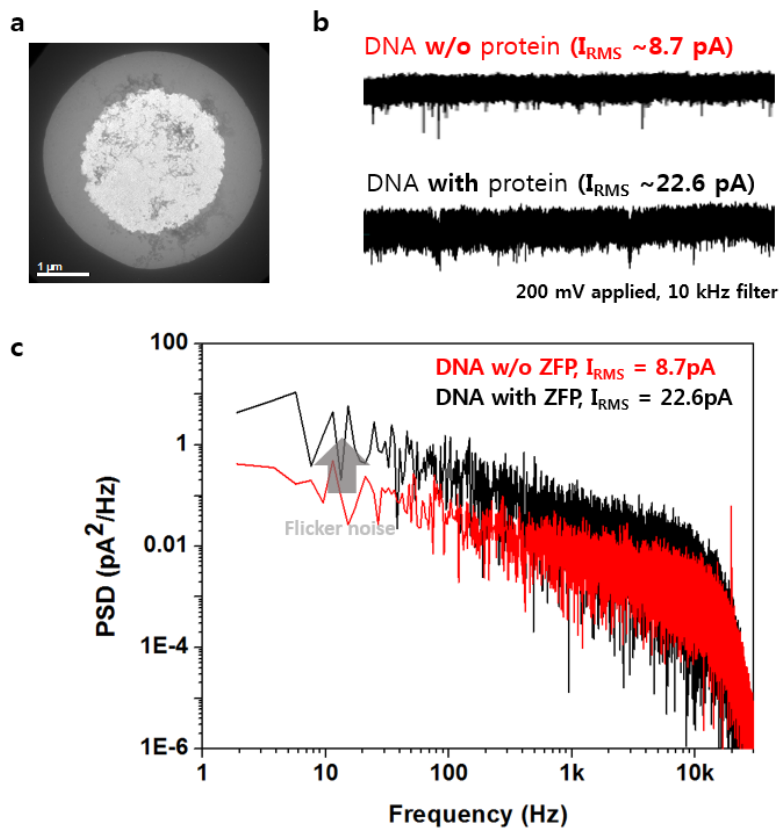


Figure 2-1. (a) A TEM image of the surface of a transferred PECVD SiN membrane. (b) Example ionic current traces when DNA or DNA/protein complexes pass through a PECVD SiN nanopore. (c) Noise PSD plot of ionic current traces in b.

2.2. Results and discussion

A low noise LPCVD SiN nanopore is fabricated with two chips: (i) a Si chip including LPCVD SiN to be used as a nanopore membrane and (ii) a quartz chip to which the LPCVD SiN membrane is to be transferred.

The chip of (i) is the same as that of a conventional Si based solid-state nanopores. First, 100 nm thick SiN is deposited on a 500 μm Si substrate by LPCVD. A 2 mm \times 2 mm pattern is formed on the SiN film by photolithography, and the SiN is removed by RIE to make an opening. After that, the Si chip including 100 nm thick freestanding SiN membrane is obtained by KOH wet etching. The quartz chip in (ii) is fabricated in the same way as in ref. 14.

The transfer process of LPCVD SiN to the quartz substrate is shown in Figure 2-2. Both surfaces of chips (i) and (ii) are hydrophilic treated with O₂ plasma (15 mA, 1 min) or piranha solution (H₂SO₄:H₂O₂ = 3:1). The two chips are placed in deionized water, and the 2 μm opening side of the quartz chip and the SiN membrane side of the Si chip are in contact with each other. The overlapping two chips are taken out of the water and dried for more than 2 hours at 90 – 100 °C hot plate. The reason for the transfer in the water is to avoid unwanted air bubbles between the SiN membrane and the quartz substrate. The freestanding SiN membrane is bonded to the quartz substrate by hydrophilic interaction. SiN in the other region is stably deposited on the Si substrate by LPCVD, which is much stronger than the hydrophilic cinteraction with the quartz substrate, resulting in easy removal of the Si substrate. The transferred 100 nm thick SiN membrane can be thinned to the desired thickness using CF₄ RIE. At 40 W, 50 sccm,

and 0.05 Torr of CF_4 RIE, the SiN etch rate is slow as ~ 0.5 nm/s, which ensure the thickness controllability even to the sub-10 nm level.

Unlike the transferred PECVD SiN, the surface of the transferred LPCVD SiN membrane is very clean and uniform because no supporting layer is required in the transfer (Figure 2-3a). Figure 2-3b is TEM images of nanopores of various sizes formed on ~ 10 nm thick LPCVD SiN membrane and shows that it is possible to stably obtain nanopores of desired size in 1 nm level. The noise of the 10 nm thick and 5 nm diameter LPCVD SiN nanopore was analyzed in 1 M KCl and 10 kHz low-pass filter (Figure 2-3b). As a result, the LPCVD SiN nanopore exhibited excellent noise characteristics of ~ 3.5 pA at 0 mV and ~ 5.2 pA at 200 mV. In the following chapters, all the nanopore experimental results are based on the low noise LPCVD SiN nanopore devices.

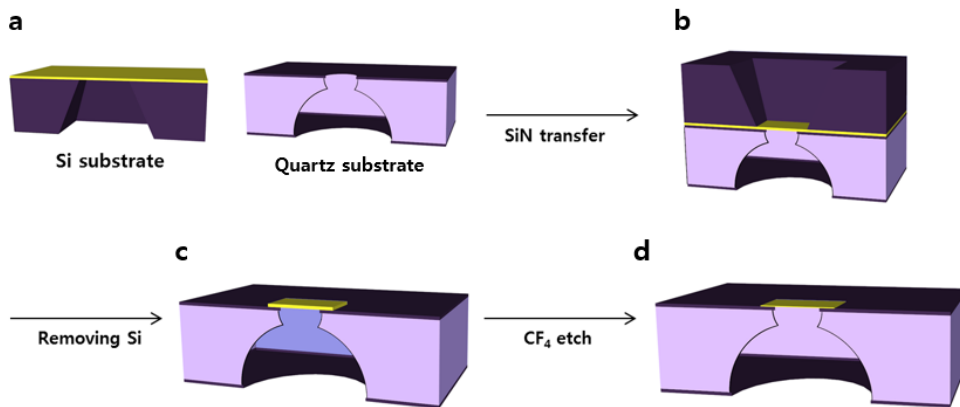


Figure 2-2. Schematic illustration of fabrication process for LPCVD SiN nanopore on the quartz substrate. (a) 100 nm thick SiN membrane on Si substrate and a quartz chip are prepared using photolithography and a wet etching processes. (b) The SiN membrane is transferred on a quartz substrate in the DI water. (c) The Si substrate is removed. (d) SiN membrane thickness is reduced to a desirable level using RIE.

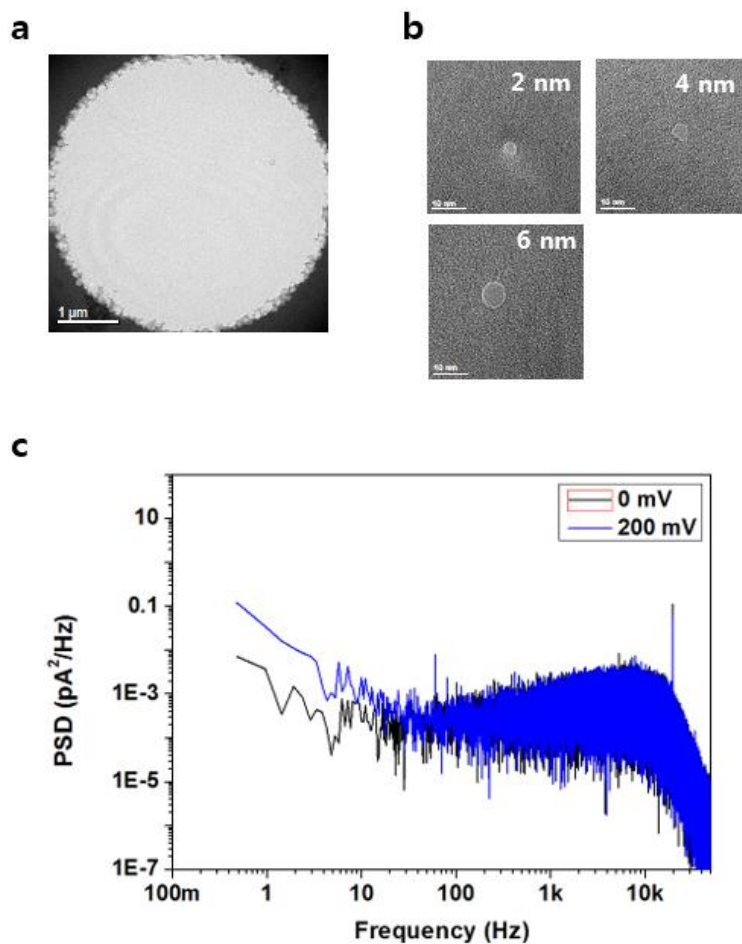


Figure 2-3. (a) A TEM image of the surface of LPCVD SiN membrane. (b) Example TEM images of LPCVD SiN nanopores of 2 nm, 4 nm, and 6 nm. (c) Noise PSD plots of 10 nm thick and 5 nm diameter LPCVD SiN nanopore when electric potential of 0 mV and 200 mV were applied.

References

1. Huang, H.; Winchester, K.; Suvorova, A.; Lawn, B.; Liu, Y.; Hu, X.; Dell, J.; Faraone, L., Effect of deposition conditions on mechanical properties of low-temperature PECVD silicon nitride films. *Materials Science and Engineering: A* 2006, 435, 453-459.
2. Joshi, B.; Eranna, G.; Runthala, D.; Dixit, B.; Wadhawan, O.; Vyas, P., LPCVD and PECVD silicon nitride for microelectronics technology. 2000.
3. Beshkov, G.; Lei, S.; Lazarova, V.; Nedev, N.; Georgiev, S., IR and Raman absorption spectroscopic studies of APCVD, LPCVD and PECVD thin SiN films. *Vacuum* 2002, 69 (1-3), 301-305.
4. Yang, C.; Pham, J., Characteristic Study of Silicon Nitride Films Deposited by LPCVD and PECVD. *Silicon* 2018, 10 (6), 2561-2567.
5. Stoffel, A.; Kovacs, A.; Kronast, W.; Müller, B., LPCVD against PECVD for micromechanical applications. *Journal of Micromechanics and Microengineering* 1996, 6 (1), 1.
6. Bi, H.; Meng, S.; Li, Y.; Guo, K.; Chen, Y.; Kong, J.; Yang, P.; Zhong, W.; Liu, B., Deposition of PEG onto PMMA microchannel surface to minimize nonspecific adsorption. *Lab on a Chip* 2006, 6 (6), 769-775.
7. Sibarani, J.; Takai, M.; Ishihara, K., Surface modification on microfluidic devices with 2-methacryloyloxyethyl phosphorylcholine polymers for reducing unfavorable protein adsorption. *Colloids and Surfaces B: Biointerfaces* 2007, 54 (1), 88-93.

CHAPTER 3.

DNA Translocation through a Nanopore in Ultrathin Self-assembled Peptide Membrane

3.1. Introduction

A nanopore is a single channel formed in a membrane that separates two chambers filled with electrolyte solutions. When a sufficient electric field is applied across the membrane, charged molecules in the solution pass through the nanopore, generating ionic current blockades. By measuring the amplitude, duration, and frequency of the ionic current drops, characteristics of the passing molecules such as the size, shape, and surface charge can be obtained.¹⁻⁵ Since the introduction of nanopore as a new DNA sequencing method,⁶ protein nanopores and solid-state nanopores have been widely used to detect and analyze biomolecules with high accuracy at the single-molecule level. Compared to protein nanopores, solid-state nanopores have the advantages of being able to easily adjust the pore dimension and long-term measurement stability under high electric fields across the membrane and high ionic concentrations.⁷⁻⁸ Owing to these advantages, experiments that require specific nanopore dimensions and long-term measurements, such as DNA homopolymer discrimination,⁹⁻¹¹ observation of DNA–protein interactions,¹²⁻¹⁵ protein–protein interactions,¹⁶⁻¹⁸ and protein conformational changes¹⁹ have been performed at the single-molecule level using solid-state nanopores.

Still, intensive efforts have been made to improve the performance of solid-state nanopore devices. Early solid-state nanopore devices used a ~20 nm thick silicon nitride layer deposited on a silicon substrate, but the nanopore membrane was too thick to be used as a sensitive nanopore sensor, and the ionic current noise arising from the substrate was too large. To reduce the ionic noise, the use of glass nanopipettes²⁰ or dielectric substrates^{9, 21} or insertion of a thick SiO₂ layer²² has been attempted and

dramatically improved the detection accuracy by reducing the dielectric noise. In addition, based on their atomically thin properties, various two-dimensional (2D) materials such as graphene,²³⁻²⁴ boron nitride,²⁵⁻²⁷ and molybdenum disulfide^{11, 28} have been used as membrane materials to improve the spatial resolution of solid-state nanopores. Integration of biomaterials into solid-state supports has also been studied to take advantage of both sides. For instance, Hall et al. attached DNA to α -hemolysin, which acts as a guide for integration to the silicon nitride support.²⁹ In addition, several interesting types of research have been conducted using the DNA origami technique by combining DNA origami nanopores having a precisely controlled pore size with a silicon nitride or glass nanopipette support.³⁰⁻³³

Among biomaterials, peptides have been developed as a functional and versatile class of materials by virtue of their ability to assemble into various nanostructures with unique properties. For instance, a tyrosine-mediated two-dimensional peptide assembly was recently developed. The YYACAYY and YFCFY sequences can assemble into flat nanosheets at the air/water interface by stabilizing their helical conformations.³⁴⁻³⁵ Moreover, the assembled 2D structures have a strong driving force to flatten the top of the hemispherical droplet into a plane, resulting in facet formation on the droplet. Owing to their high mechanical stability, the peptide sheets can be easily transferred to another substrate by quickly stamping the top of the droplet. The short film formation time (<15 min) and adjustable thin film thicknesses (~5 nm) are attractive properties of peptide sheets for use as a nanopore membrane. In this work, we employed a self-assembled peptide nanosheet to integrate biological materials and solid-state nanopores. The peptide sheet was transferred to a ~100 nm thick silicon nitride layer containing an

ion beam drilled ~200 nm hole, and a peptide nanopore was formed by perforation using transmission electron microscopy (TEM). The supporting substrate has the same structure as a previously reported low-noise glass substrate platform. The TEM-based diameter controllability and noise properties of peptide nanopores in ionic solution measurements were investigated, and dsDNA translocation through a peptide nanopore was demonstrated.

3.2. Experimental details

Self-assembly peptide

All the peptides (98% purity) were purchased from GL Biochem (Shanghai, China) and used without further purifications. Other solvents were purchased from Sigma-Aldrich. YFCFY peptide (monomer) was dissolved in deionized water and its concentration was 1.5 mM. After the solutions rendered uniformly by tip sonicating for 2 min, they were placed in a heat block at 80°C for air oxidation. After incubation for 4 days, disulfide bonds were formed from sulfhydryl residues of cysteine in the monomer. After an extracted aliquot (90 μ L) from the sufficiently oxidized solution was dropped on siliconized glass (2.2×2.2 cm²), faceting started within a few minutes. The average diameter of the droplet was 6.6 mm. The assembled films were transferred directly to the substrate by stamping the film from the upper side. Etching was performed by carefully dipping the prepared device into a 5% (v/v) methanol solution.

Nanopore experiment

On a 300 μ m thick quartz substrate, a 100 nm amorphous Si layer was deposited using low-pressure chemical vapor deposition (LPCVD) to act as a mask layer for HF wet etching. A 2×2 μ m² area was defined on one side, and a 100×100 μ m² was defined

on the other side of the substrate by photolithography and dry etching. Sandblasting was used to etch the majority of the quartz, and the last part was wet-etched using 49 wt.% HF. On top of the substrate, a ~100 nm low-stress LPCVD SiN_x layer was transferred. A ~200 nm pore was drilled by a focused ion beam. The peptide nanopore chip was assembled in custom-made polytetrafluoroethylene cells, and 1 M KCl solution buffered at pH 8.0 was used in all the experiments. The ionic current was measured using Ag/AgCl electrodes, Axopatch 200B amplifier systems with a sampling rate of 250 kHz, and a 100 kHz low-pass filter. DNA samples (1000 bp) were purchased from Thermo Fisher Scientific (NoLimits 1000-bp DNA Fragment) and used at 1 nM concentrations in 1 M KCl. DNA translocation events were analyzed using Clampfit 10.4, and events with dwell times longer than 50 μs and current drops larger than 10 times of IRMS were selected to remove bouncing events.

3.3. Results and Discussion

3.3.1. Peptide film characterization and nanopore formation

The YFCFY peptide has multiple aromatic residues and a sulfide group in the center of the sequence (Figure 3-1a). The former can induce strong π - π interaction, and the latter can be cross-linked by a disulfide bridge, stabilizing the helical conformation of the peptide. The peptide was dissolved in deionized water and placed in a heat block at 80 °C for 4 days to induce a disulfide bond between the cysteine residues; the solution was then placed on siliconized glass. Within 15 min, a 10-15 nm thick 2D assembled peptide sheet appeared on top of the droplet with faceting phenomena due to the strong driving forces (Figure 3-1b). As shown in Figures 3-1c, TEM analysis clearly reveals a macroscopically uniform morphology of the peptide sheet, and direct imaging of sheets on a holey carbon grid at high magnification resolves their structural integrity. The peptide sheet was transferred to a ~100 nm thick silicon nitride supporting layer that contained an ion beam-drilled ~200 nm hole, as shown schematically in Figure 3-1e. TEM images of the free-standing peptide membrane on silicon nitride are shown in Figure 3-1f. It can be clearly observed that the uniform YFCFY peptide sheet was well transferred, and a ~5 nm peptide nanopore can be perforated with a focused electron beam.

Because the initially transferred peptide film is quite thick (>10 nm, Figure 3-2a) for use as a highly sensitive nanopore membrane, it is necessary to obtain a thinner and more uniform film by introducing an etching process. The assembled peptide sheet has

a stable structure in water, but it slowly dissolves out when exposed to methanol owing to the high solubility of the peptide in methanol. To obtain a precise controllability, we prepared an etching solution by diluting methanol in water to 5% by volume. The freshly transferred film on silicon nitride was carefully dipped in the etching solution. Figure 3-2a shows the evolution of the thickness of the transferred film with etching time. The film was originally thick (11.55 ± 4.66 nm) but grew thinner with a smaller deviation in the thickness (4.89 ± 0.71 nm and 2.13 ± 0.7 nm after 1 and 3 h of etching, respectively). Atomic force microscopy (AFM) data show that the film was very flat and uniform after 2 h of etching (Figure 3-2b).

Unlike the case for robust silicon nitride membranes, as the peptide sheet is composed of several connected peptide molecules, it is necessary to confirm pore diameter controllability under the focused electron beam in TEM. When the same electron beam conditions used for perforating a nanopore on a silicon nitride membrane (200 kV, largest condenser lens aperture, spot mode of the highest current density) were applied, the peptide nanopore was formed too rapid to control the size of pore, and the surrounding area was easily damaged (Figure 3-3). To reduce the electron beam density and obtain the desirable size controllability, the spot size of the electron beam was minimized; this has also been done to control graphene nanopores.³⁶ An electron beam density of $\sim 10^7$ e/nm², which is an order lower than the electron density used for silicon nitride nanopores,⁷ was applied to a ~ 20 nm² area of the freestanding peptide membrane. For the YFCFY membrane, nanopores began to form after ~ 10 s of electron beam focusing; the pore diameter according to the time after pore creation is shown in Figure 3-2c. Note that the pore size can be controlled precisely at the <5 nm diameter level.

TEM images of YFCFY nanopores with diameters of 2–12 nm are shown in Figure 3-2d.

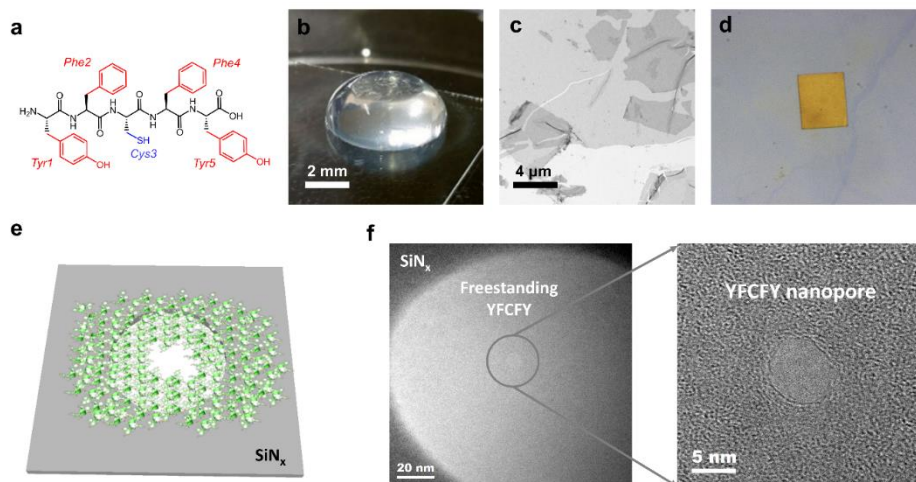


Figure 3-1. Peptide film characteristics. (a) Chemical structure of YFCFY. (b) Oblique view of droplet with a single large facet on siliconized glass. (c) TEM image of peptide film assembled at the air/water interface. (d) Optical images of peptide film transferred to silicon nitride membrane. (e) Schematic diagram of a peptide nanopore on silicon nitride supporting layer. (f) TEM images of ~5 nm peptide nanopore.

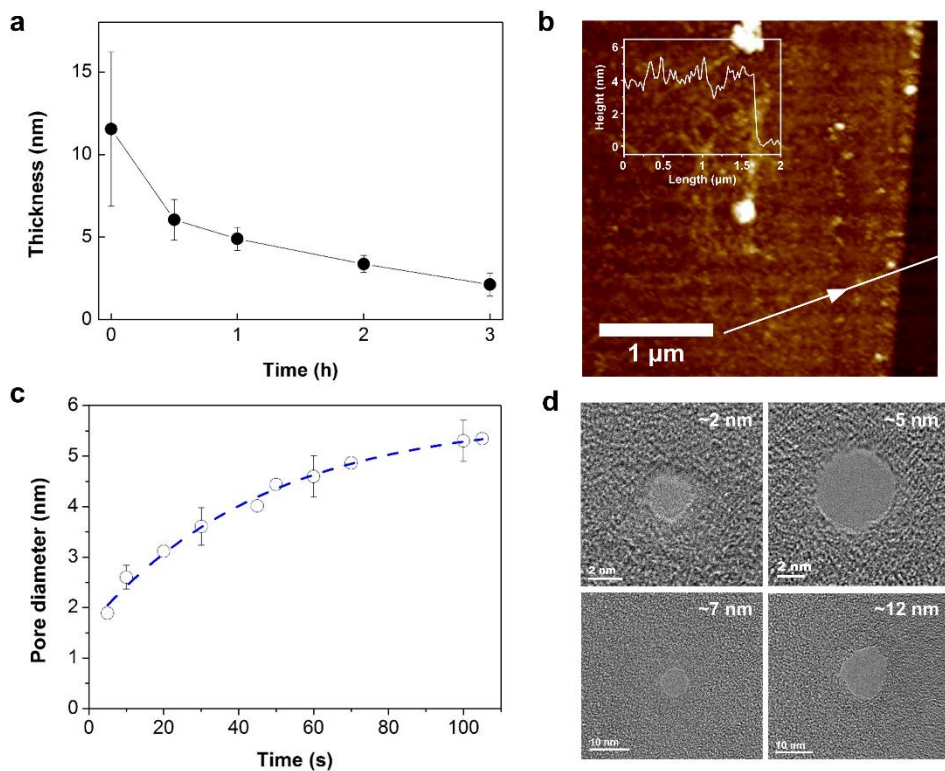


Figure 3-2. Thickness and diameter control of peptide nanopores. (a) Thickness of YFCFY film when exposed to a 5% methanol solution. (b) AFM image of YFCFY film after thinning. (c) Nanopore forming rate under $\sim 10^7$ e/nm²·s electron beam irradiation. (d) TEM images of peptide nanopores with various diameters.

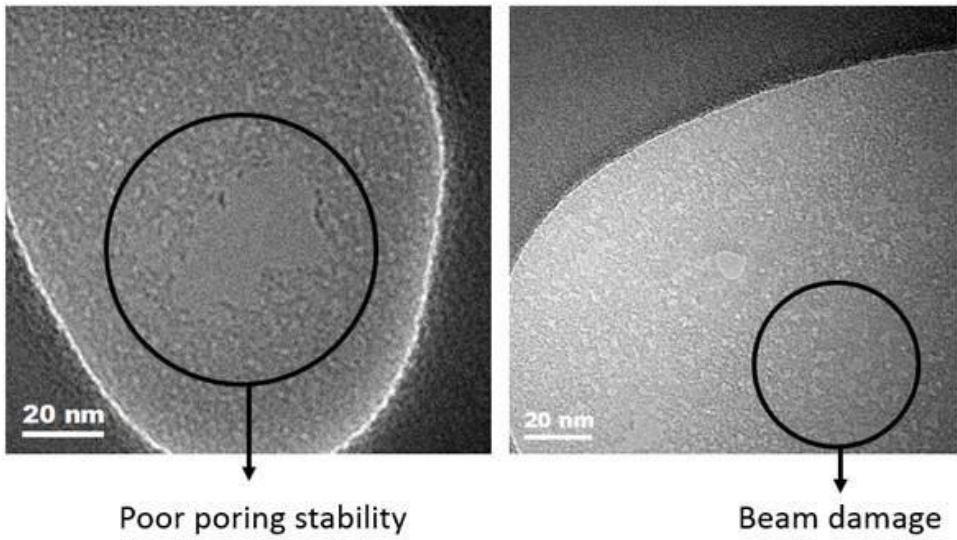


Figure 3-3. Peptide film stability under high density of electron beam.

3.3.2. Nanopore conductance measurements and noise characteristics

The peptide nanopore device was assembled into custom-made flow cells, and the chambers were filled with a 1 M potassium chloride buffer. Figure 3-4a shows the current measurement results for various pore dimensions, 158 nS (16 nm diameter, 2 nm thickness), 39.7 nS (7 nm diameter, 5 nm thickness), and 7.6 nS (2.5 nm diameter, 5 nm thickness), which exhibit linear I-V characteristics. The pore dimensions were estimated using the ionic conductance equation, $G = \sigma \left[\frac{4l}{\pi d^2} + \frac{1}{d} \right]^{-1}$, where σ is the bulk conductivity, l is the membrane thickness, and d is the pore diameter.³⁷

To analyze the noise characteristics of the YFCFY membrane, the noise power spectral density (PSD, S_I) (Figure 3-4b) and I_{RMS} , which is the square root of the integral of S_I (Figure 3-4c), of a peptide nanopore ~ 7 nm in diameter and ~ 5 nm in thickness were measured using a 100 kHz low-pass filter. I_{RMS} was ~ 20 pA with no voltage and less than 35 pA at applied voltages of up to 300 mV; I_{RMS} increased considerably as the voltage increased beyond 300 mV. The 1/f-type noise generally increases with applied voltage in the low-frequency regime, and it is expressed as $S_{1/f} = (A_N/f) \times I^2$, where A_N is the noise power, f is the frequency, and I is the ionic current.³⁸ As shown in the fitting result of the normalized PSD, S_I/I^2 , in Figure 3-4d, the noise power A_N of the peptide nanopore is $\sim 5.1 \times 10^{-8}$. The noise power is approximately 2 orders of magnitude smaller than that of a single-layer 2D membrane such as graphene or boron nitride, which has an A_N value of $\sim 10^{-6}$, and is similar to the A_N value of multilayer boron nitride or the commonly used silicon nitride.^{25, 38-40}

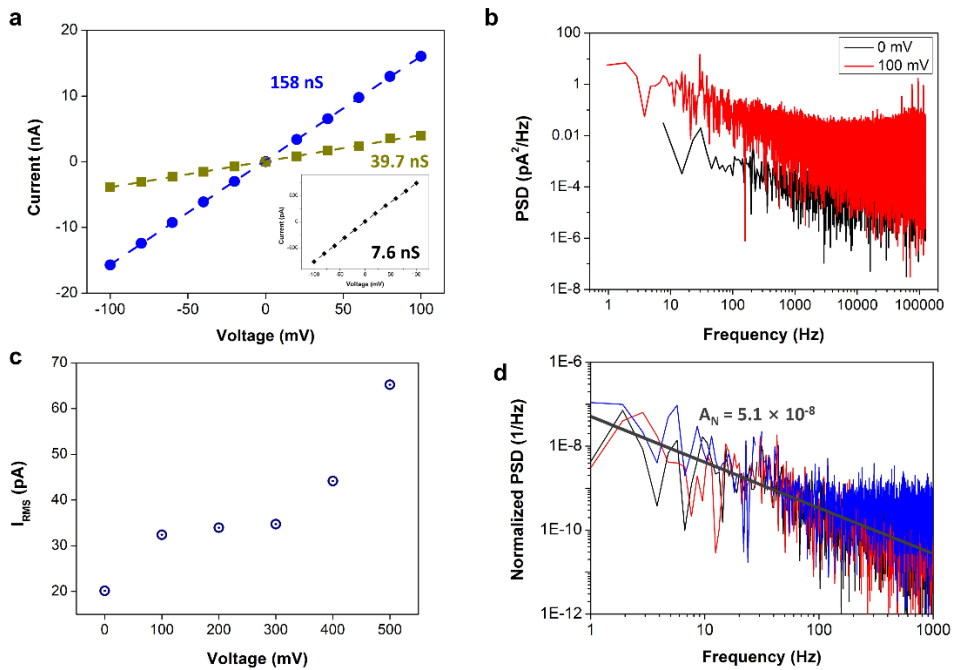


Figure 3-4. Peptide nanopore characteristics in ionic solutions. (a) I - V characteristics of peptide nanopores in 1 M KCl. Inset: I - V curve of ~2.5 nm peptide nanopore. (b) Noise PSD of a peptide nanopore under applied voltages of 0 and 100 mV. (c) I_{RMS} of the peptide nanopore under applied voltages of 0 to 500 mV. (d) Normalized PSD and noise power fitting.

3.3.3. DNA translocation through a peptide nanopore

To investigate the DNA transport characteristics and signal-to-noise ratio (SNR) of the YFCFY peptide nanopore, we performed translocation experiments using 1000-bp double-stranded DNA mixed at 1 nM concentrations in 1 M KCl solution (buffered at pH 8.0). Although the thinnest YFCFY peptide membrane that can be made is ~ 2 nm thick, it has not been possible to obtain reliable DNA translocation data because of pore expansion during the measurement. For a nanopore ~ 5 nm in thickness, more than 200 events for each applied voltage were stably obtained, and a ~ 2.5 nm diameter nanopore was used to maximize the SNR and eliminate DNA folding issues. Figure 3-5a shows current traces indicating dsDNA translocation through the peptide nanopore at various applied voltages. Although DNA translocation events were consistently observed at applied voltages above 300 mV, successive DNA translocation events could not be reliably obtained at voltages below 300 mV owing to nanopore clogging. Because the YFCFY peptide membrane is thin (~ 5 nm) and the pore diameter (~ 2.5 nm) is slightly larger than the diameter of dsDNA (2.2 nm), an SNR of as high as 30 could be obtained (Figure 3-5c).

The dwell time histogram for each voltage is log-normally distributed and shows values of ~ 992 , ~ 656 , and ~ 422 μs for voltages of 300, 500, and 700 mV, respectively (Figure 3-5d). The translocation speed of 1000-bp DNA through the peptide nanopore at 300 mV is ~ 1 bp/ μs , which is ~ 1.8 times slower than that of silicon nitride nanopores with similar dimensions (~ 2.7 nm diameter).⁴¹ Because the DNA translocation speed was reportedly reduced in a nanopore membrane with a positive surface charge,⁴² we

measured the zeta potential of the YFCFY peptide sheet to determine whether there is a surface charge effect. However, as shown in Figure 3-6, the zeta potential of the peptide film at pH 8 is approximately -23 mV, which is similar to that of silicon nitride nanopores.⁴³ A previous study analyzed the interaction between DNA and a peptide, which consists of hydrogen bonding between the protein backbone or side chain and the DNA backbone or base edges. Among the three amino acids Tyr, Phe, and Cys that make up the peptide nanopore used in this experiment, Tyr has a total of 19 hydrogen bonds to the four bases (adenine, thymine, guanine, and cytosine) of DNA strands.⁴⁴ It is also known that a large van der Waals interaction due to aromatic ring stacking is present in Phe.⁴⁵ In addition to the DNA/pore interaction by confinement owing to the small pore size, which is commonly known, it can be assumed that the drag effect occurs by the peptide/DNA interactions mentioned above. As shown in Figure 3-5e, the conformation of the DNA translocation events reveals the drag effect, where the majority of events start with a partial current blockade and become fully dropped as the peak proceeds to the end.

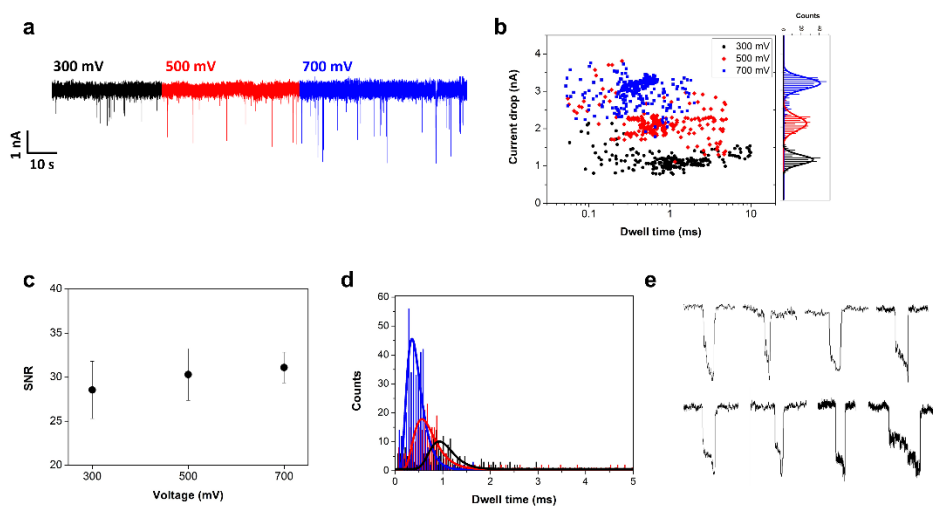


Figure 3-5. DNA translocation through peptide nanopores. (a) Current traces of 1000-bp DNA translocation at three applied voltages. (b) Scatter plot and current drop histograms of DNA translocation events. (c) SNR at three applied voltages. (d) Dwell time histograms for three voltages. (e) Representative events showing dragging effects at the pore entrance (scales are not same).

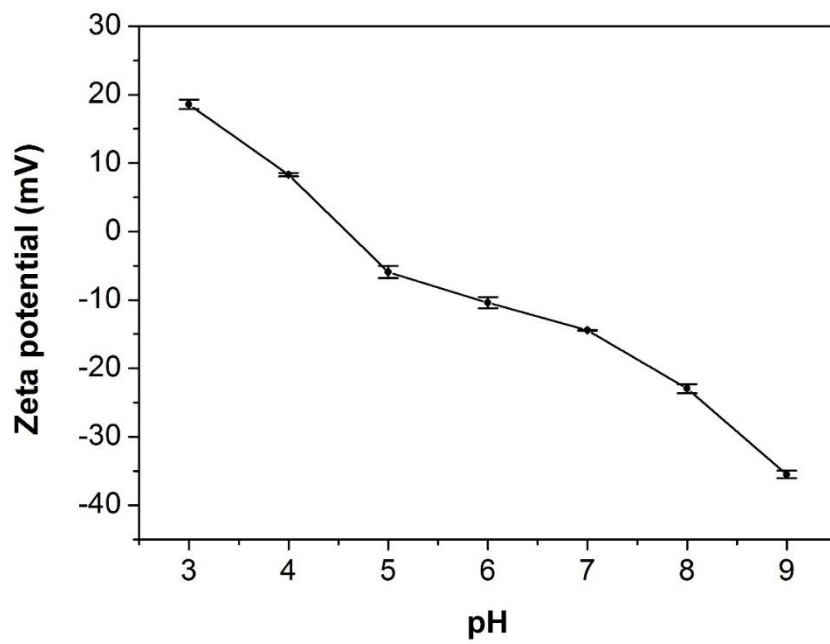


Figure 3-6. Zeta potential of YFCFY peptide films.

3.4. Summary

We first demonstrated the possibility of using a self-assembled peptide as a nanopore membrane combined with a solid-state device. The peptide proposed here, YFCFY, forms a stable and robust film at the air/water surface within ~ 15 min and can be easily implemented on a solid-state substrate. The peptide membrane also has the advantage of a low thickness, which can be reduced to as low as 2 nm through an etching process. Peptide nanopores can be successfully formed using the conventional focused electron beam method with adjusted spot size, resulting in highly reproducible nanopore diameter control. When a 100 kHz low-pass filter was used, it was confirmed that the peptide nanopore has an ionic current noise of less than 35 pA at the large applied voltage of 300 mV. Finally, in DNA translocation experiments, a slow translocation speed of ~ 1 bp/ μ s through the ~ 2.5 nm diameter peptide nanopore was obtained, which is ~ 1.8 times slower than that of silicon nitride nanopores with similar dimensions. On the basis of the characteristic event conformations, the elongated dwell time is thought to be a dragging effect caused by hydrogen bonds and van der Waals forces between DNA bases and amino acids. This first nanopore device with a peptide membrane can be further improved by controlling the interface using inorganic materials or designing new peptide sequences. Ultimately, we believe that peptide membranes can serve as a platform to incorporate biological functionalities and control specific interactions.

References

1. Fologea, D.; Ledden, B.; McNabb, D. S.; Li, J., Electrical characterization of protein molecules by a solid-state nanopore. *Applied physics letters* 2007, 91 (5), 053901.
2. Freedman, K. J.; Haq, S. R.; Edelman, J. B.; Jemth, P.; Kim, M. J., Single molecule unfolding and stretching of protein domains inside a solid-state nanopore by electric field. *Scientific reports* 2013, 3, 1638.
3. Larkin, J.; Henley, R. Y.; Muthukumar, M.; Rosenstein, J. K.; Wanunu, M., High-bandwidth protein analysis using solid-state nanopores. *Biophysical journal* 2014, 106 (3), 696-704.
4. Li, J.; Gershow, M.; Stein, D.; Brandin, E.; Golovchenko, J. A., DNA molecules and configurations in a solid-state nanopore microscope. *Nature materials* 2003, 2 (9), 611.
5. Talaga, D. S.; Li, J., Single-molecule protein unfolding in solid state nanopores. *Journal of the American Chemical Society* 2009, 131 (26), 9287-9297.
6. Kasianowicz, J. J.; Brandin, E.; Branton, D.; Deamer, D. W., Characterization of individual polynucleotide molecules using a membrane channel. *Proceedings of the National Academy of Sciences* 1996, 93 (24), 13770-13773.

7. Kim, M. J.; Wanunu, M.; Bell, D. C.; Meller, A., Rapid fabrication of uniformly sized nanopores and nanopore arrays for parallel DNA analysis. *Advanced materials* 2006, 18 (23), 3149-3153.
8. Storm, A.; Chen, J.; Ling, X.; Zandbergen, H.; Dekker, C., Fabrication of solid-state nanopores with single-nanometre precision. *Nature materials* 2003, 2 (8), 537.
9. Lee, M.-H.; Kumar, A.; Park, K.-B.; Cho, S.-Y.; Kim, H.-M.; Lim, M.-C.; Kim, Y.-R.; Kim, K.-B., A low-noise solid-state nanopore platform based on a highly insulating substrate. *Scientific reports* 2014, 4, 7448.
10. Venta, K.; Shemer, G.; Puster, M.; Rodriguez-Manzo, J. A.; Balan, A.; Rosenstein, J. K.; Shepard, K.; Drndic, M., Differentiation of short, single-stranded DNA homopolymers in solid-state nanopores. *ACS nano* 2013, 7 (5), 4629-4636.
11. Feng, J.; Liu, K.; Bulushev, R. D.; Khlybov, S.; Dumcenco, D.; Kis, A.; Radenovic, A., Identification of single nucleotides in MoS₂ nanopores. *Nature nanotechnology* 2015, 10 (12), 1070.
12. Shim, J.; Humphreys, G. I.; Venkatesan, B. M.; Munz, J. M.; Zou, X.; Sathe, C.; Schulten, K.; Kosari, F.; Nardulli, A. M.; Vasmatazis, G., Detection and quantification of methylation in DNA using solid-state nanopores. *Scientific reports* 2013, 3, 1389.
13. Squires, A.; Atas, E.; Meller, A., Nanopore sensing of individual transcription factors bound to DNA. *Scientific reports* 2015, 5, 11643.

14. Yu, J.-S.; Lim, M.-C.; Huynh, D. T. N.; Kim, H.-J.; Kim, H.-M.; Kim, Y.-R.; Kim, K.-B., Identifying the location of a single protein along the DNA Strand Using Solid-State Nanopores. *ACS nano* 2015, 9 (5), 5289-5298.
15. Kowalczyk, S. W.; Hall, A. R.; Dekker, C., Detection of local protein structures along DNA using solid-state nanopores. *Nano letters* 2009, 10 (1), 324-328.
16. Freedman, K. J.; Bastian, A. R.; Chaiken, I.; Kim, M. J., Solid-state nanopore detection of protein complexes: applications in healthcare and protein kinetics. *Small* 2013, 9 (5), 750-759.
17. Japrun, D.; Dogan, J.; Freedman, K. J.; Nadzeyka, A.; Bauerdick, S.; Albrecht, T.; Kim, M. J.; Jemth, P.; Edel, J. B., Single-molecule studies of intrinsically disordered proteins using solid-state nanopores. *Analytical chemistry* 2013, 85 (4), 2449-2456.
18. Kwak, D. K.; Chae, H.; Lee, M. K.; Ha, J. H.; Goyal, G.; Kim, M. J.; Kim, K. B.; Chi, S. W., Probing the small-molecule inhibition of an anticancer therapeutic protein-protein interaction using a solid-state nanopore. *Angewandte Chemie International Edition* 2016, 55 (19), 5713-5717.
19. Waduge, P.; Hu, R.; Bandarkar, P.; Yamazaki, H.; Cressiot, B.; Zhao, Q.; Whitford, P. C.; Wanunu, M., Nanopore-based measurements of protein size, fluctuations, and conformational changes. *ACS nano* 2017, 11 (6), 5706-5716.

20. Li, W.; Bell, N. A.; Hernández-Ainsa, S.; Thacker, V. V.; Thackray, A. M.; Bujdosó, R.; Keyser, U. F., Single protein molecule detection by glass nanopores. *ACS nano* 2013, 7 (5), 4129-4134.
21. Balan, A.; Chien, C.-C.; Engelke, R.; Drndić, M., Suspended solid-state membranes on glass chips with sub 1-Pf capacitance for biomolecule sensing applications. *Scientific reports* 2015, 5, 17775.
22. Balan, A.; Machielse, B.; Niedzwiecki, D.; Lin, J.; Ong, P.; Engelke, R.; Shepard, K. L.; Drndić, M., Improving signal-to-noise performance for DNA translocation in solid-state nanopores at MHz bandwidths. *Nano letters* 2014, 14 (12), 7215-7220.
23. Merchant, C. A.; Healy, K.; Wanunu, M.; Ray, V.; Peterman, N.; Bartel, J.; Fischbein, M. D.; Venta, K.; Luo, Z.; Johnson, A. C., DNA translocation through graphene nanopores. *Nano letters* 2010, 10 (8), 2915-2921.
24. Schneider, G. F.; Kowalczyk, S. W.; Calado, V. E.; Pandraud, G.; Zandbergen, H. W.; Vandersypen, L. M.; Dekker, C., DNA translocation through graphene nanopores. *Nano letters* 2010, 10 (8), 3163-3167.
25. Park, K.-B.; Kim, H.-J.; Kim, H.-M.; Han, S. A.; Lee, K. H.; Kim, S.-W.; Kim, K.-B., Noise and sensitivity characteristics of solid-state nanopores with a boron nitride 2-D membrane on a pyrex substrate. *Nanoscale* 2016, 8 (10), 5755-5763.

26. Zhou, Z.; Hu, Y.; Wang, H.; Xu, Z.; Wang, W.; Bai, X.; Shan, X.; Lu, X., DNA translocation through hydrophilic nanopore in hexagonal boron nitride. *Scientific reports* 2013, 3, 3287.
27. Liu, S.; Lu, B.; Zhao, Q.; Li, J.; Gao, T.; Chen, Y.; Zhang, Y.; Liu, Z.; Fan, Z.; Yang, F., Boron nitride nanopores: highly sensitive DNA single-molecule detectors. *Advanced materials* 2013, 25 (33), 4549-4554.
28. Liu, K.; Feng, J.; Kis, A.; Radenovic, A., Atomically thin molybdenum disulfide nanopores with high sensitivity for DNA translocation. *ACS nano* 2014, 8 (3), 2504-2511.
29. Hall, A. R.; Scott, A.; Rotem, D.; Mehta, K. K.; Bayley, H.; Dekker, C., Hybrid pore formation by directed insertion of α -haemolysin into solid-state nanopores. *Nature nanotechnology* 2010, 5 (12), 874.
30. Bell, N. A.; Engst, C. R.; Ablay, M.; Divitini, G.; Ducati, C.; Liedl, T.; Keyser, U. F., DNA origami nanopores. *Nano letters* 2011, 12 (1), 512-517.
31. Hernández-Ainsa, S.; Bell, N. A.; Thacker, V. V.; Göpflich, K.; Misiunas, K.; Fuentes-Perez, M. E.; Moreno-Herrero, F.; Keyser, U. F., DNA origami nanopores for controlling DNA translocation. *ACS nano* 2013, 7 (7), 6024-6030.

32. Plesa, C.; Ananth, A. N.; Linko, V.; Gülcher, C.; Katan, A. J.; Dietz, H.; Dekker, C., Ionic permeability and mechanical properties of DNA origami nanoplates on solid-state nanopores. *ACS nano* 2013, 8 (1), 35-43.
33. Wei, R.; Martin, T. G.; Rant, U.; Dietz, H., DNA origami gatekeepers for solid-state nanopores. *Angewandte Chemie* 2012, 124 (20), 4948-4951.
34. Jang, H.-S.; Lee, J.-H.; Park, Y.-S.; Kim, Y.-O.; Park, J.; Yang, T.-Y.; Jin, K.; Lee, J.; Park, S.; You, J. M., Tyrosine-mediated two-dimensional peptide assembly and its role as a bio-inspired catalytic scaffold. *Nature communications* 2014, 5, 3665.
35. Lee, J.; Choe, I. R.; Kim, N.-K.; Kim, W.-J.; Jang, H.-S.; Lee, Y.-S.; Nam, K. T., Water-floating giant nanosheets from helical peptide pentamers. *ACS nano* 2016, 10 (9), 8263-8270.
36. Goyal, G.; Lee, Y. B.; Darvish, A.; Ahn, C. W.; Kim, M. J., Hydrophilic and size-controlled graphene nanopores for protein detection. *Nanotechnology* 2016, 27 (49), 495301.
37. Kowalczyk, S. W.; Grosberg, A. Y.; Rabin, Y.; Dekker, C., Modeling the conductance and DNA blockade of solid-state nanopores. *Nanotechnology* 2011, 22 (31), 315101.
38. Smeets, R. M.; Keyser, U. F.; Dekker, N. H.; Dekker, C., Noise in solid-state nanopores. *Proceedings of the National Academy of Sciences* 2008, 105 (2), 417-421.

39. Kumar, A.; Park, K.-B.; Kim, H.-M.; Kim, K.-B., Noise and its reduction in graphene based nanopore devices. *Nanotechnology* 2013, 24 (49), 495503.
40. Heerema, S.; Schneider, G.; Rozemuller, M.; Vicarelli, L.; Zandbergen, H.; Dekker, C., 1/f noise in graphene nanopores. *Nanotechnology* 2015, 26 (7), 074001.
41. Wanunu, M.; Sutin, J.; McNally, B.; Chow, A.; Meller, A., DNA translocation governed by interactions with solid-state nanopores. *Biophysical journal* 2008, 95 (10), 4716-4725.
42. Park, K.-B.; Kim, H.-J.; Kang, Y.-H.; Yu, J.-S.; Chae, H.; Lee, K.; Kim, H.-M.; Kim, K.-B., Highly reliable and low-noise solid-state nanopores with an atomic layer deposited ZnO membrane on a quartz substrate. *Nanoscale* 2017, 9 (47), 18772-18780.
43. Firnkes, M.; Pedone, D.; Knezevic, J.; Doblinger, M.; Rant, U., Electrically facilitated translocations of proteins through silicon nitride nanopores: conjoint and competitive action of diffusion, electrophoresis, and electroosmosis. *Nano letters* 2010, 10 (6), 2162-2167.
44. Mandel-Gutfreund, Y.; Schueler, O.; Margalit, H., Comprehensive analysis of hydrogen bonds in regulatory protein DNA-complexes: in search of common principles. *Journal of molecular biology* 1995, 253 (2), 370-382.

45. Luscombe, N. M.; Laskowski, R. A.; Thornton, J. M., Amino acid–base interactions: a three-dimensional analysis of protein–DNA interactions at an atomic level. *Nucleic acids research* 2001, 29 (13), 2860-2874.

CHAPTER 4.

Identifying the Location of a Single Protein along the DNA Strand Using Solid-State Nanopores

4.1. Introduction

Zinc finger proteins (ZFPs) are one of the transcriptional activators and the most common DNA binding motif in all metazoan.¹ Each zinc finger is capable of recognizing three adjacent base pairs in the major groove of double-stranded DNA (dsDNA) via a single α -helix with high affinity and sequence specificity.² Its DNA recognition is mediated through base contacts with specific amino acids located on the recognition helix. ZFPs typically contain several fingers and three-fingered proteins such as Zif268, and Sp1 recognizes a tract of nine base pairs of dsDNA.³⁻⁴ The diversity in ZFP recognition potential has been expanded by the development of designer zinc fingers and characterization of ZFP-binding properties. Recently, engineered ZFPs with binding ability to a specific DNA sequence have gained a great deal of attention for research, diagnostics, gene therapy, and gene editing.⁵⁻⁸ Because of the sequence-specific binding nature of ZFPs, long-range haplotype mapping of DNA using engineered ZFPs would be possible. However, there are relatively few technologies to characterize binding affinities of ZFPs for their cognate DNA binding sites and to map the binding locations along the length of DNA. Gel-shift assay is the most common technique to determine the affinity of ZFP toward DNA with a recognition site, but it does not give any information about the exact location to where ZFP binds.⁹⁻¹⁰ Fluorescent imaging is another way of imaging the bound protein on DNA,¹¹⁻¹² but diffraction limitations of optical microscopy and labeling requirements hinder the practical application of this method. Although, atomic force microscopy (AFM) is capable of imaging bound molecules on DNA in high resolution,^{7, 13-15} its uses are

inherently restricted in surface environment and require rather complicated sample preparation processes. Here, we found that solid-state nanopore is an ideal method to identify the position of zinc finger proteins and their binding characteristics to single protein resolution.

Solid-state nanopores, which have nanometer sized pores fabricated in a mechanically stable membrane,¹⁶ have attracted much interest as a useful device in detection and analysis of nanometer scale biomolecules due to its advantages of high throughput, high sensitivity, and its simplicity of measurements, namely purely electrical label-free detection.¹⁷⁻¹⁸ Therefore, there are great deals of publications regarding nanopore-based analysis of DNA, RNA, protein, and their interactions as well as potential for a next generation sequencing technology.¹⁹⁻²⁵ In particular, there were several studies about the detection of DNA binding proteins or polymers such as RecA,²⁶ bis-PNA,²⁷ γ -PNA,²⁸ and E. coli SSB.²⁹ Recently, several groups have reported progress toward the detection of single protein bound to a DNA using glass and silicon nitride nanopore, allowing them to identify the presence of a target protein and quantification of a modified DNA. Carlsen et al. used DNA-protein complexes and found a dependency between nanopore event rate and protein concentration.³⁰⁻³¹ Also, by designing DNA carriers and using biotin-streptavidin binding, Bell et al. identified whether the target proteins exist in the mixed solution using a glass nanopore.³⁰⁻³¹ Solid-state nanopores modified with ligand such as aptamer could also detect the target protein by monitoring the elongated translocation time due to the interaction between grafted aptamer and passing protein.³² Biological nanopores like α -Hemolysin and cytolysin A having asymmetric structure with vestibule were also used

to study the conformational heterogeneity and binding kinetics of DNA-protein interaction.³³⁻³⁴ Symmetric protein nanopore, SP1 (stable protein) having 3 nm of pore-diameter, was also shown to have a potential for detecting ssDNA as well as characterizing the 3D structure of peptides and DNAs by eliminating the vector constriction or direction followed by random passage.³⁵ To the best of our knowledge, this is the first study for discrimination of DNA-ZFP complexes from pristine DNA to single protein resolution and identifying the location of a ZFP in a DNA strand without any additional signal amplification and fluorescent labeling. Here, we introduce detection of sequence-specific DNA-binding ZFP using solid-state nanopores. ZFPs can be designed to have strong binding affinities for their cognate DNA binding site and to have novel recognition specificities by protein engineering techniques. For instance, the affinities and specificities of engineered ZFP can be enhanced by addition of structured linkers between zinc fingers and dimerization of fused domains.³⁶⁻³⁷ In this work, the engineered ZFP Zif268-NRE with a structural linker was used to recognize the specific DNA sequence of a DNA strand and to demonstrate the possibility of identifying the location of recognition sequence using solid-state nanopore.

Low-stress LPCVD silicon nitride membrane of ~100 nm is transferred on highly insulating Pyrex substrate. Thickness of the transferred membrane is reduced to a desirable level (5-20 nm) by dry etching, and the nanopore is formed using highly focused electron beams.³⁸ The nanopore chip is then assembled into acrylic fluid cells and is hydrated using a buffered KCl solution. When positive bias voltage is applied across the nanopore by Ag/AgCl electrodes, DNA and the DNA/ZFP complex are caught by an electric field and pass through (translocate) the nanopore.

Schematic concepts of solid-state nanopore-based identification of DNA-protein interactions are described in Figure 4-1. When a bare DNA translocates a nanopore, it gives rise to a single step current blockade (ΔI_{DNA}), while ZFP-bound DNA generated an additional peak (ΔI_{ZFP}) due to the extra volume of ZFP. In other words, the increased volume caused by ZFP binding on DNA was successfully reflected by a discrete current blockade peak. Furthermore, by analyzing the ratio of DNA translocation times before (t_1) and after (t_2) the ZFP peak, the position of ZFP binding locus in two different DNAs was analyzed. The low noise characteristics of our solid-state nanopore that was fabricated upon highly insulating substrates³⁹ enabled us to monitor the location of a single protein that spans around approximately 20 bp along the length of DNA (Fig 4-1d).

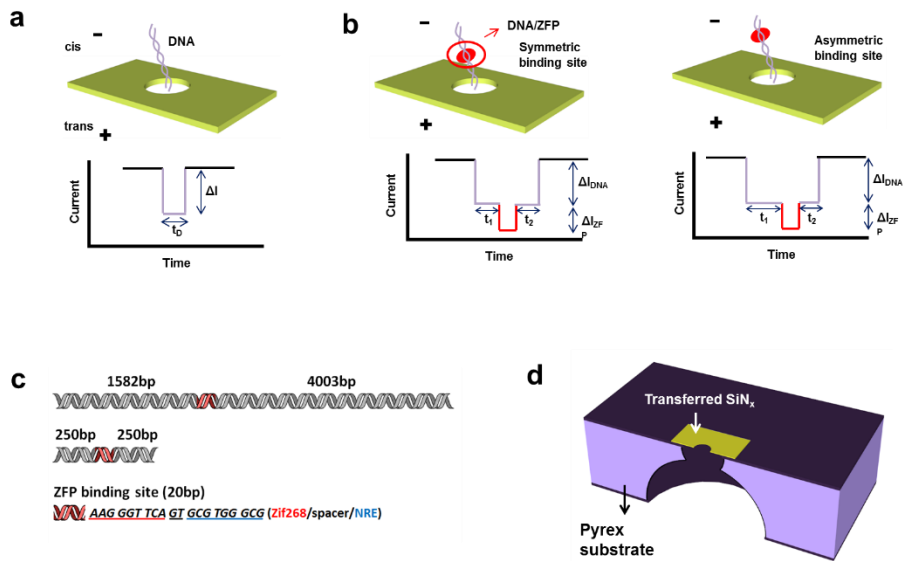


Figure 4-1. Schematic illustrations of nanopore-based identification of DNA-protein interactions. (a) A translocation event of a bare dsDNA gives rise to a single level current drop. (b) dsDNAs with ZFP binding sites at different parts of the strands display an additional current drop peak in accordance with the binding site. (c) Schematics of two dsDNAs used in this work. One is 5605 bp with a 20 bp binding site at the 2-to-5 position and the other is 520 bp with a 20 bp binding site at the center. (d) Cross-sectional illustration of a low noise solid-state nanopore device used in this work (not to scale).

4.2. Experimental details

Nanopore experiments

Low-stress LPCVD SiN_x 100 nm was deposited on 500 μm thick Si substrate. After photolithography and reactive ion etching, KOH wet etch was used to form freestanding SiN_x membrane (2 × 2 mm² window) on a 10 × 10 mm² Si chip. The SiN_x membrane was transferred onto Pyrex substrate, which is fabricated as previously described,³⁹ then the membrane was etched by CF₄ plasma to a desirable thickness (etch rate of ~15 nm/min). The nanopore was drilled into the transferred membrane by a highly focused electron beam using TEM. Prior to use, the nanopore was treated with oxygen plasma (15 mA, 30 sec), and the nanopore chip was assembled in a custom-designed acrylic flow cell. After that, 500 mM KCl electrolyte solutions (buffered at pH 8.0 with 100 mM Tris-HCl) were introduced to the flow cell to hydrate the nanopore. The assembled nanopore cell was put in a dark Faraday cage, and then Ag/AgCl electrodes were connected to a patch clamp system and put into each chamber of the flow cell (cis and trans). In all of the experiments, the DNA concentration was set to 10 nM and the ZFP concentration was set to 4 times higher than the DNA. The ionic current was measured using the Axopatch 200B; the sampling rate was 250 kHz and was low-pass filtered with a 10 kHz Bessel filter. Translocation events were collected with Clampex 10.4 and further analyzed using Clampfit 10.4 software. To discriminate real translocations from

bouncing spikes, we analyzed translocation events based on two common criteria, dwell time and current drop. Events having dwell time longer than 50 μ s and current drop larger than 10 times of noise rms values are considered as real translocations.

Chemicals

Agar powder and sodium chloride (NaCl) were provided from Daejung Chemicals & Metals Co., Ltd. (Gyeonggi-do, Korea). Luria–Bertani (LB) broth was purchased from BD (Difco, Lawrence, KS, USA). Ampicillin, isopropyl- β -D-thiogalactopyranoside (IPTG) and DL- dithiothreitol (DTT) were purchased from Biosesang (Gyeonggi-do, Korea). The other chemicals such as T4 DNA ligase, NotI, PstI and amylose resin were purchased from NEB (Ipswich, MA, USA), and Ethylenediaminetetraacetic acid (EDTA) was purchased from Biobasic (Markham, ON, Canada). Maltose monohydrate, zinc sulfate ($ZnSO_4$), magnesium chloride ($MgCl_2$), ethidium bromide and Coomassie blue were purchased from Sigma-Aldrich (St. Louis, MO, USA). The DNA ladder (100 bp), protein ladder (10 kDa) and Tris-HCl were from Noble bio (Gyeonggi-do, Korea).

Expression and purification of ZFP

Plasmids containing the Zif268//NRE zinc finger protein, pMal-c2x::zfp was kindly provided from Dr. Daniel Branton from the Department of Molecular and Cellular

Biology at Harvard University. *E. coli* BL21 (DE3) harboring pMal-c2x::zfp plasmids were grown in 100 ml LB containing ampicillin (100 µg/ml) to an OD600 of 0.7 - 0.8 in a 37 °C shaking incubator (200 rpm) followed by the addition of 0.1 mM IPTG and grown overnight at 18 °C. Cells were then harvested by centrifugation at 4 °C for 20 min and resuspended in 5 ml column buffer (20 mM Tris-HCl, 200 mM NaCl, 1 mM EDTA, pH 7.4). The collected cells were disrupted by sonication for 10 min in an ice bath at 225 W (duty cycle 50%, VC 750, Sonics & Materials Inc., Newtown, CT, USA). After centrifugation at 4,000 rpm for 20 min, the supernatant was retained and loaded onto a column packed with 600 µl amylose resin. The amylose column was washed with column buffer, and the zinc finger proteins were eluted by a column buffer containing 10 mM maltose. The purified zinc finger proteins were then identified and quantified by 8% SDS-PAGE and Bradford assay, respectively.

Preparation of dsDNA strands containing ZFP binding sites

Two types of dsDNAs with different lengths and ZFP binding positions were prepared to examine the possibility of detecting the location of recognition sequence using solid-state nanopore. Double-stranded DNA (5605 bp) with ZFP binding sites at the 2-to-5 position was constructed by inserting chemically synthesized oligonucleotides (5'-GGC CAA GGG TTC AGT GCG TGG GCG -3' and 5'-GGC CCG CCC ACG CAC TGA ACC CTT-3') with 20 bp of target sequence and NotI sites

at both ends into the NotI site of pET21a(+) vectors. The plasmid containing ZFP binding sites was then linearized by enzymatic digestion with PstI. Short dsDNA (520 bp) with ZFP binding site at the 1-to-1 position was prepared by PCR using a primer set (5'-AAA ACC CCT CAA GAC CCG TTT AGA - 3' and 5'-TGC CGG CCA CGA TGC GTC CGG CGT - 3') and purified pET21a(+) vectors containing ZFP binding sites as a template. For the gel shift assay, a pET21a(+) vector containing ZFP binding sites as a template and the primer set (5'-TCT AGA ACT AGT GGA TC-3' and 5'-ATT AAC CCT CAC TAA AG-3') were used to amplify 126 bp dsDNA with a ZFP binding sequence as a positive control. Double stranded DNA (134 bp) was used as a negative control without a ZFP binding sequence. It was prepared by amplification of the *Klebsiella pneumoniae* KCTC 2242 fimI gene using the primer set (5'-ATG CAG GGA ATG AAA TCT GGT CTG-3' and 5'-CAT TAT CTC CTT GTC TGC TCA CCG-3'). The amplified DNA fragments were purified using a gel extraction kit prior to experiments.

Gel shift assay

Zinc finger protein and tested DNAs were incubated in 10 μ l of 200 mM Tris-HCl (pH 7.0) containing 100 mM NaCl, 200 μ M ZnSO₄, 10 mM MgCl₂ and 5 mM DTT at room temperature for 1 hr.⁴ Then, the reactions were run on 10% native polyacrylamide gel and stained with EtBr to visualize the location of DNA.⁴⁰

AFM analysis of the DNA-ZFP complex

To visualize and confirm the location of ZFP on the DNA strand, the 520 bp DNA containing the ZFP binding site and the DNA-ZFP complex were imaged by AFM. After incubation of ZFP and DNA with a recognition site in a binding solution for 1 hr at room temperature, NiCl₂ was added to the binding solutions at a final concentration of 10 mM to promote the adsorption of DNA molecules on the mica surface. 100 nM DNA and 40 nM ZFP were used as a final concentration in this analysis. Pristine DNA without ZFP was also examined to compare the DNA-ZFP complex morphology. A 20 µl sample solution was deposited on the freshly cleaved mica disc (10 mm in diameter), and the mica disc was washed with 3 ml filtered distilled water after 10 min incubation at room temperature. The disc was then dried with a mild stream of nitrogen gas and stored in a vacuum desiccator until it was examined using AFM (XE-70, Park Systems, Suwon, Korea). Pristine DNA and the DNA-ZFP complex were then imaged in tapping mode with non-contact cantilever probes (PPP-NCHR, Park Systems) at a 0.3 Hz scan rate.

Effect of KCl concentration on association and dissociation of ZFP to target DNA

A pair of oligonucleotides with a ZFP binding site was synthesized with biotin at the 5' end of one oligonucleotide: Biotin-5'-
CTTACCGCCCACGCACTGAACCCTTGCAGA-3OH and 5P-

TCTGCAAAGGGTTCAGTGCGTGGGCGGTAAG-3OH. The 18-base ZFP recognition sequences are underlined. Streptavidin-coated SPR chips were preconditioned with three consecutive 10 L injections of 1 M NaCl in 50 mM NaOH at a flow rate of 10 L/min. The chip was equilibrated with TES buffer (10 mM Tris-HCl (pH 7.5), 300 mM NaCl, 1 mM EDTA) for 1 min at a flow rate of 10 mL/min. Biotinylated DNAs in TES buffer at a final concentration of 1 ng/l were injected at a flow rate of 5 mL/min for 5 min at 20 °C. The injection was stopped manually after the change in resonance unit (RU) reached 100 RU. Purified ZFP in running buffer (10 mM Tris-HCl (pH 7.6), 120 mM KCl, 10 mM MgCl₂, 0.5 mM DTT, and 30 g/mL BSA) to a final concentration of 100 nM was introduced with a flow rate of 20 L/min for 3 min at 20°C. The association of ZFP to immobilized target DNA was monitored while ZFP was introduced to the SPR chip surface. To evaluate the effect of KCl on the formation and dissociation of a specific ZFP-DNA complex, varying KCl concentrations from 0.2 M to 1 M were introduced to the chip surface with a flow rate of 20 L/min for 1 min. The sensor chip was regenerated in between association and dissociation experiments by injecting 0.5% SDS at a flow rate of 20 L/min for 1 min. Treatment of the sensor chip with 0.5% SDS released the bound protein without affecting the binding capacity of the immobilized DNA.

4.3. Results and Discussion

4.3.1. Translocation of short DNA (520 bp)/ZFP complex

To demonstrate the possibility of identifying the location of protein binding site, we prepared a simple and symmetric dsDNA (520-bp) with ZFP binding site at the center (1-to-1) of the DNA strand. The 520-bp DNA and ZFP were put into an ionic solution of 400 mM KCl, and 100 mV bias voltages were applied across a 4 nm diameter silicon nitride nanopore (5 nm thick). Electrical measurements were performed in 400 mM KCl solution because DNA-protein interactions are very sensitive to salt concentration. ZFP binding to DNA is disrupted at high KCl concentrations over 700 mM, as demonstrated in Figure 4-2. Because KCl concentration is an important parameter for signal to noise ratio in electrical measurements, 400 mM KCl was chosen because ZFP dissociation from the DNA binding site starts to occur at 500 mM KCl. From the translocation data, two types of events were observed. In Figure 4-3a, representative translocation data, two types of events are shown. One type is a single profile current drop with a relatively short translocation time (Type I), and the other is a translocation event with an additional current spike within a relatively long translocation time (Type II). Current traces are acquired from 100 pM DNA, 8 nm diameter pore, and 10 nm thick SiN and event rate in Figure 4-3c was acquired from these data.

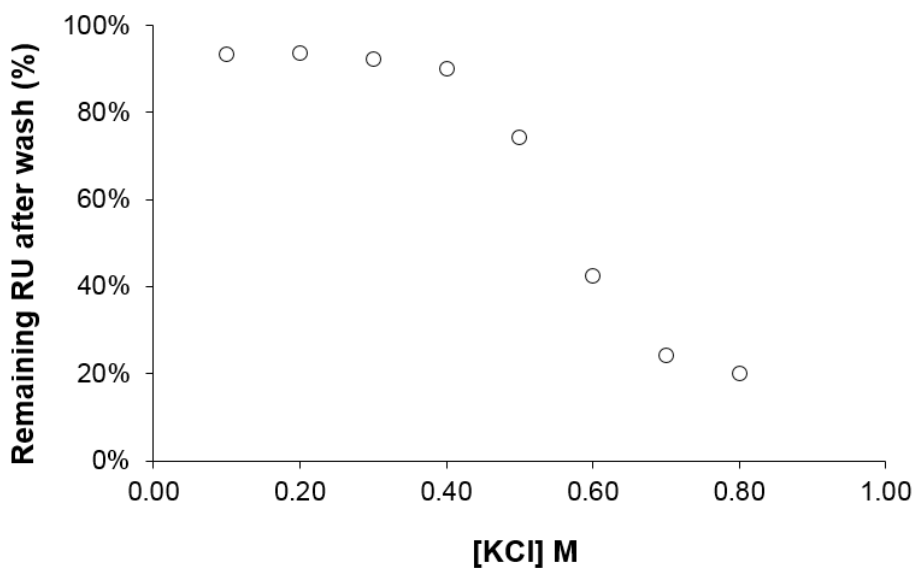


Figure 4-2. The effect of KCl on ZFP-DNA dissociation. Zinc finger proteins bound to immobilized target DNA with its specific recognition sequence were exposed to varying KCl concentrations. The level of remaining ZFP on its target DNA after treating the sensor chip with a given KCl concentration was presented. ZFP binding to a target DNA was not affected at low KCl concentrations. Dissociation began at 0.5 M KCl, and most of proteins seemed to dissociate at KCl concentrations over 0.7 M.

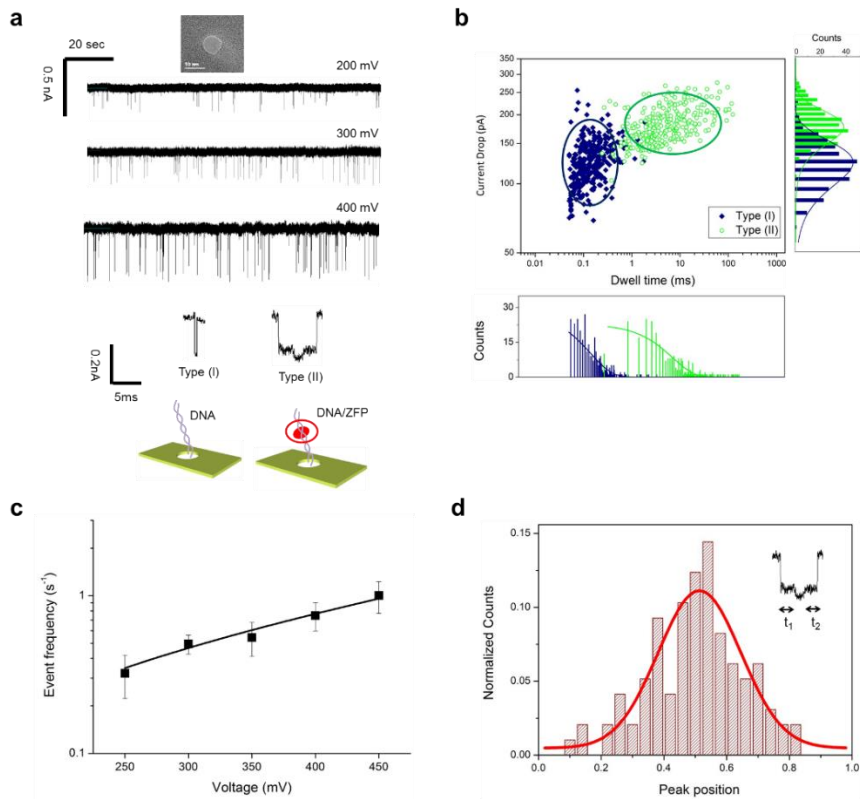


Figure 4-3. Analysis of DNA (520 bp, binding site at the center) translocation events with ZFP in 400 mM KCl. (a) Current traces from the translocation of DNA-ZFP complex under three different applied voltages. Two types of event signals were detected. (b) Scatter plot of translocation events for 100 mV applied voltage. Type (I) and type (II) events were indicated as navy diamonds and green circles, respectively. Type (II) events clearly show higher current drop and longer dwell time. (c) The frequency of translocation events as a function of applied voltage, showing an exponential increase in event frequency along with increased applied voltage. (d) Histogram of $t_1/(t_1+t_2)$, where t_1 is assigned as the dwell time from the start of the event to the additional spike, and t_2 is assigned as the dwell time from the additional spike to the end of the event.

A scatter plot of current drop versus dwell time of all DNA (520 bp)/ZFP translocation events is displayed in Figure 4-3b. The difference between type (I) and type (II) events is clearly shown. For type (II) events, the maximum magnitude of current drop, namely the gap between the open pore current and the current level of the additional spike ($\Delta I_{\text{DNA}} + \Delta I_{\text{ZFP}}$) is plotted. The current drop histograms were fitted by a Gaussian function with a mean current drop of ~ 122 pA and ~ 173 pA for type (I) and type (II) events, respectively. The dwell time histogram showed an exponential decay with a mean dwell time of ~ 136 μs and ~ 5.86 ms for type (I) and type (II) events, respectively. Based on these differences in current drop and dwell time, we assumed that type (I) and type (II) events resulted from bare DNA and DNA/ZFP complex translocations, respectively. It should be noted that although the signal amplitude is not that high due to a low molar concentration (400 nM) and a relatively low applying voltage (100 mV), the signal can be resolved because the rms noise of the present nanopore device is less than 10 pA.

We analyzed the translocation times of type (II) events, which have a characteristic current trace with distinct peaks representing the location of ZFP binding site. The position of ZFP binding site was investigated by assigning the dwell time from the start of the event to the additional current spike as t_1 and from the additional current spike to the end of the event as t_2 . A histogram demonstrating the ratio of t_1 and t_1+t_2 , which reflects ZFP location on the 520 bp DNA, is presented in Figure 4-3c. Normalized counts mean the ratio of the number of specific events to total number of events (297 events). From the histogram, one Gaussian distribution with a mean value of 0.513 ± 0.132 was observed. Assuming that the translocation time is proportional to the DNA

length, the expected mean $t_1/(t_1+t_2)$ value is 0.500, which is well matched with the experimental data.

4.3.2. Characterization of DNA/ZFP binding

The sequence-specific binding of ZFP on target DNA was also confirmed by AFM⁷. A 520 bp of DNA as used in our nanopore experiment was examined as a template for AFM analysis because short double stranded DNA (approximately 180 nm) with a persistence length of 35 nm⁴¹ is very likely to be present as a linear form, which would facilitate determining the position of bound ZFP on the DNA strand. AFM analysis revealed that the ZFP bound exclusively at the middle of a 520 bp of DNA with a specific binding site spanning from the 251st to the 270th bases (Fig 4-4b). The height of bound ZFP on the target site is approximately 3 nm whereas that of pristine DNA is approximately 1.6 nm. From these results, it is evident that ZFP binds to the target DNA in sequence-specific manner and the binding site location is represented as the additional current drop within the DNA blockade when analyzed with our solid-state nanopore.

The specific binding properties of ZFP to a target DNA were also confirmed using native polyacrylamide gel electrophoresis. ZFP and DNA harboring specific recognition sequences were incubated at room temperature for 1 hr to form DNA/ZFP complexes and then resolved by native polyacrylamide gel electrophoresis. After the gel was stained with EtBr, the DNA location was observed under UV light (Fig 4-4c and d). As expected, the ZFP binds to the DNA containing its target recognition sequence, and DNA/ZFP complex formation was evidenced by decreased mobility. As demonstrated in Figure 4-4c and d, mobility of the DNA bound with ZFP was lower than that without ZFP. The zinc finger protein location was also examined by staining

the gel with coomassie blue (Fig 4-5b). The band location of ZFP exactly matches that of DNA with a specific binding site in native polyacrylamide gel, implying that the shift was induced by ZFP-DNA complex formation. In other words, DNA/ZFP complex formation decreased DNA mobility at a given bias voltage. The bound ZFP may also partially screen the negative charge of DNA resulting in reduced DNA mobility. The specificity of ZFP to a target DNA was confirmed by reacting the protein with DNA that lacked a recognition sequence. The absence of a gel-shift in the reaction containing ZFP and DNA lacking a recognition sequence implies that the binding reaction is sequence specific. According to the gel electrophoresis and AFM results, it is evident that the type (I) and type (II) events are attributed to the passage of bare DNA and the DNA/ZFP complex, respectively.

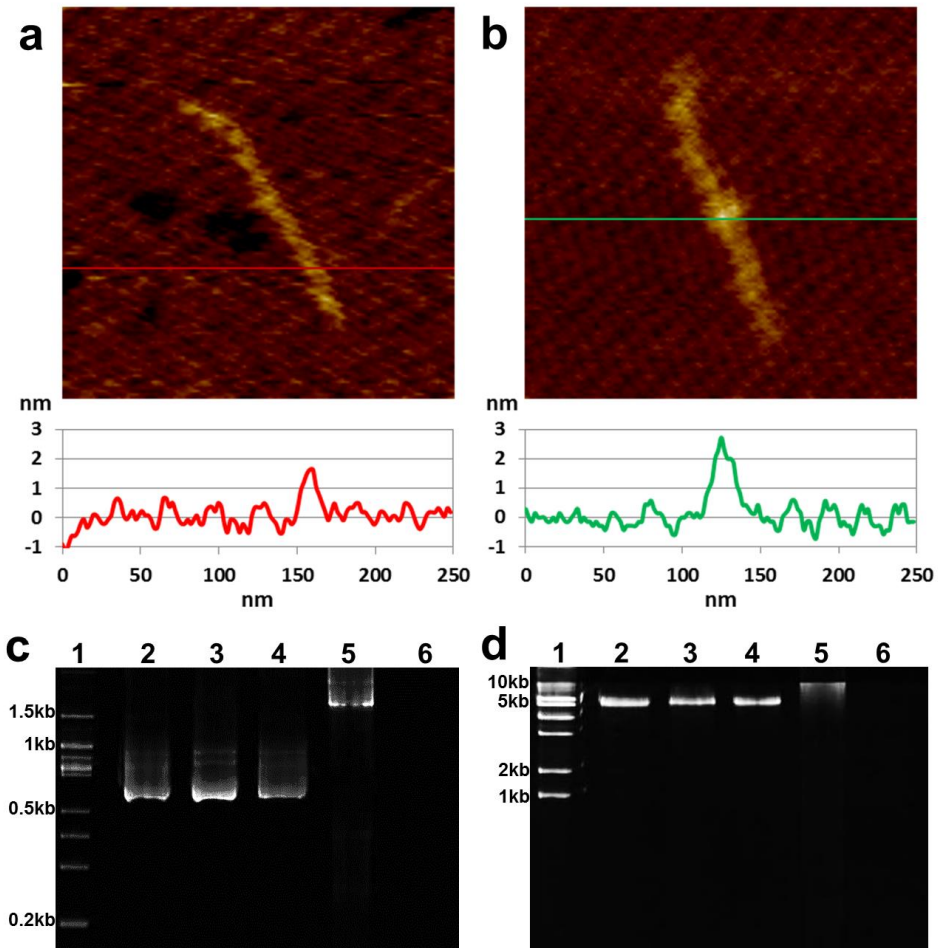


Figure 4-4. AFM images of bare DNA (a) and the DNA-ZFP complex (b). DNA (520 bp) that was approximately 180 nm in length was used in this analysis. The scan sizes of the images are 250×250 nm with Z-scale of 4 nm. Gel-shift assay of 520 bp DNA (c) and 5605 bp DNA (d) in the presence and absence of ZFP. Lane 1, DNA marker; Lane 2, DNA without recognition sequence; Lane 3, DNA without recognition sequence reacted with ZFP; Lane 4, DNA with recognition sequence; Lane 5, DNA with recognition sequence reacted with ZFP; Lane 6, ZFP alone.

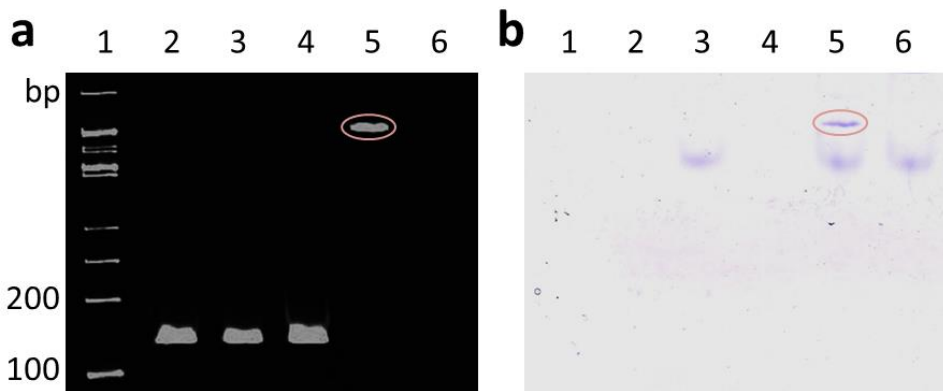


Figure 4-5. Gel-shift assay of bare DNA and the DNA/ZFP complex run on a 10% native polyacrylamide gel and stained with EtBr (a) and coomassie blue (b). Lane 1, DNA marker; Lane 2, DNA (134 bp) without recognition sequence; Lane 3, DNA (134 bp) without recognition sequence reacted with ZFP; Lane 4, DNA (126 bp) with recognition sequence; Lane 5, DNA (126 bp) with recognition sequence reacted with ZFP; Lane 6, ZFP. The protein bands in the lower position are from unbound free ZFPs.

4.3.3. Translocation of long DNA (5605 bp)/ZFP complex and identifying the binding locations

Upon confirming the sequence-specific binding between DNA and ZFP, we performed further nanopore experiments to verify the possibility of identifying the specific binding site. We prepared a 5605-bp DNA with a ZFP binding site (20 bp), which was located at the asymmetric position of 2-to-5 (1582 base-to-4003 base) in the DNA strand as shown in Figure 4-1c. In other words, the length of DNA from one end to the ZFP binding site and from the other end to the ZFP binding site are 1582 bp and 4003 bp, respectively. Figure 4-6a shows current traces from the translocation of DNA (5605 bp)/ZFP through 8 nm diameter and 10 nm thickness nanopore under three different bias voltages and event frequency plot in figure 4-6d was acquired from these data.

As was shown earlier in this report, short single level translocation events (type (I)) and long translocation events with an additional current drop (type (II)) were detected. In Figure 4a, representative translocation events of each type are shown. Type (I) events have mean dwell time of 69 μ s with $\Delta I/I_0 = 0.11$ (ΔI = magnitude of current drop, I_0 = open pore current), which shows similar current drop magnitude and dwell time as those of typical DNA translocation events.⁴²

Scatter plot of current drop versus dwell time of all translocation events is shown in Figure 4-6b. The current drop histograms were fitted by a Gaussian function with a mean current drop of ~ 864 pA and ~ 1345 pA for type (I) and type (II) events, respectively. The dwell time histograms showed an exponential decay with a mean

dwell time of $\sim 69 \mu\text{s}$ and $\sim 1.7 \text{ ms}$ for type (I) and type (II) events, respectively. The all-point current histogram reveals two distinct peaks, which represent type (I) and type (II) translocation events with a mean amplitude of current blockage of $\sim 831 \text{ pA}$ and $\sim 1228 \text{ pA}$, respectively (Fig 4-6c).

Because a number of researchers have reported quantized level events arising from the translocation of folded DNA,^{19, 43-44} we conducted further experiments to confirm that the additional current peaks are indeed attributed to ZFP binding, not to folded DNA. Using the same nanopore and ionic solution, we performed translocation experiments with varying voltage conditions (300 mV, 500 mV, and 700 mV). Figure 4-7b demonstrates the dependency of ΔI_{DNA} and ΔI_{ZFP} on three different applied voltages. Both ΔI_{DNA} and ΔI_{ZFP} linearly increase with applied voltages. We also investigated the ratio between ΔI_{ZFP} and ΔI_{DNA} , which is $\Delta I_{\text{ZFP}}/\Delta I_{\text{DNA}}$, to confirm that the additional current drop is a reflection of ZFP binding on DNA (Figure 4-7c). For three different voltage conditions, the value of the $\Delta I_{\text{ZFP}}/\Delta I_{\text{DNA}}$ is almost constant (~ 0.355), which implies that the additional current drop came from ZFP binding on DNA. Considering that the translocation of folded DNA typically results in a quantized (two- or three-fold) current drop,^{19, 43-44} it is clear that the additional current drop is caused from bound ZFP on the DNA strand.

Based on the results that the additional current spike within DNA blockade comes from the ZFP bound on DNA with recognition sequence, it is possible to identify the location of ZFP binding site in tested DNA. As described above, the position of ZFP binding site was investigated by assigning the dwell time from the start of event to the additional spike as t_1 and from the additional spike to the end of event t_2 . A histogram

demonstrating the ratio of t_1 and t_1+t_2 , which reflects the location of the ZFP in DNA, is presented in Figure 4-8.

As demonstrated in Figure 4-8a, analysis of the translocations (total 320 events) for DNA with bound ZFP resulted in two Gaussian distributions with a mean value of each $t_1/(t_1+t_2)$ distribution of 0.287 ± 0.081 and 0.729 ± 0.081 . In total, two distinct distributions were probable results because DNA can enter the nanopore in two different directions. When the shorter DNA end enters the nanopore first, we assigned the direction (I), but when the longer DNA end enters first, we assigned the direction (II). As shown in Figure 4-1c, the DNA used in this study has a ZFP binding site at the 2-to-5 position (1582 base-to-4003 base). In other words, the DNA length from one end to the ZFP binding site and from the other end to the ZFP binding site were 1582 bp and 4003 bp, respectively. Assuming that the DNA length is proportional to the translocation time, the expected t_1/t_2 values are 0.283 (1582/5585) and 0.717 (4003/5585), which closely correlate with our experimental results (0.287 and 0.729). After normalization, the translocation time ratio was assessed by designating the shorter end of DNA from the ZFP binding site as t_1 and the longer end as t_2 . Thus, the mean value of $t_1/(t_1+t_2)$ for direction (I) and (II) are 0.287 ± 0.082 and 0.271 ± 0.075 , respectively (Figure 4-8b). These results also correlate well with the theoretical value, 0.283.

It is interesting to note that the mean $t_1/(t_1+t_2)$ value is slightly larger than expected (0.283) in direction (I) (0.287) and smaller in direction (II) (0.271). The same phenomenon was observed in 520-bp DNA with ZFP that is bound at the center of the DNA. The mean value of $t_1/(t_1+t_2)$ for the DNA with bound ZFP in a symmetric position was 0.513 ± 0.132 . These results indicate that the translocation velocity of the front part

of the DNA that enters the nanopore first could be slightly lower than the latter part. Thus, the local DNA translocation velocity increases towards the end of the translocation process, which is consistent with previous reports.⁴⁵⁻⁴⁶

Surprisingly, as demonstrated in the scatter plot of Figure 4-6b, type (II) events have a much longer translocation time than type (I) events. The delayed translocation of DNA with bound protein was also reported elsewhere with a somewhat different degree of delay.^{27, 29, 47} The translocation time may have been delayed possibly due to protein adsorption to the pore walls or increased interactions of the bulky, less-charged DNA-protein complex with the pore. We presume that the following factors influence the slower DNA/ZFP complex translocation through the solid state nanopore: (i) the DNA/ZFP complex has a bulkier structure, and thus has stronger interactions with the pore walls than the bare DNA.^{27, 29, 47} (ii) ZFP binding causes local uncoiling of dsDNA in the vicinity of the ZFP binding site. Relatively hydrophobic bases, both purines and pyrimidines, are normally buried within the double helical DNA structure but the uncoiling induced by ZFP binding could result in base exposure outwards and may contribute to a greater interaction with the nanopore. A single stranded DNA with fully exposed bases has a greater interaction with the nanopore, which results in longer translocation time compared with a dsDNA.⁴⁸ (iii) Binding with positively charged ZFP in the tested environment would reduce the local negative charge of DNA because the electrophoretic force on DNA is proportional to the effective charge density of DNA.⁴⁹⁻⁵⁰ (iv) Binding with ZFP increases the overall mass of DNA and thus increases dragging force during translocation. Although there is no clear-cut explanation for this slowing down effect, we speculate that all of these factors together may contribute to the delayed

translocation of the DNA/ZFP complex. This result by itself may also suggest one way of controlling DNA translocation through the solid-state nanopore.

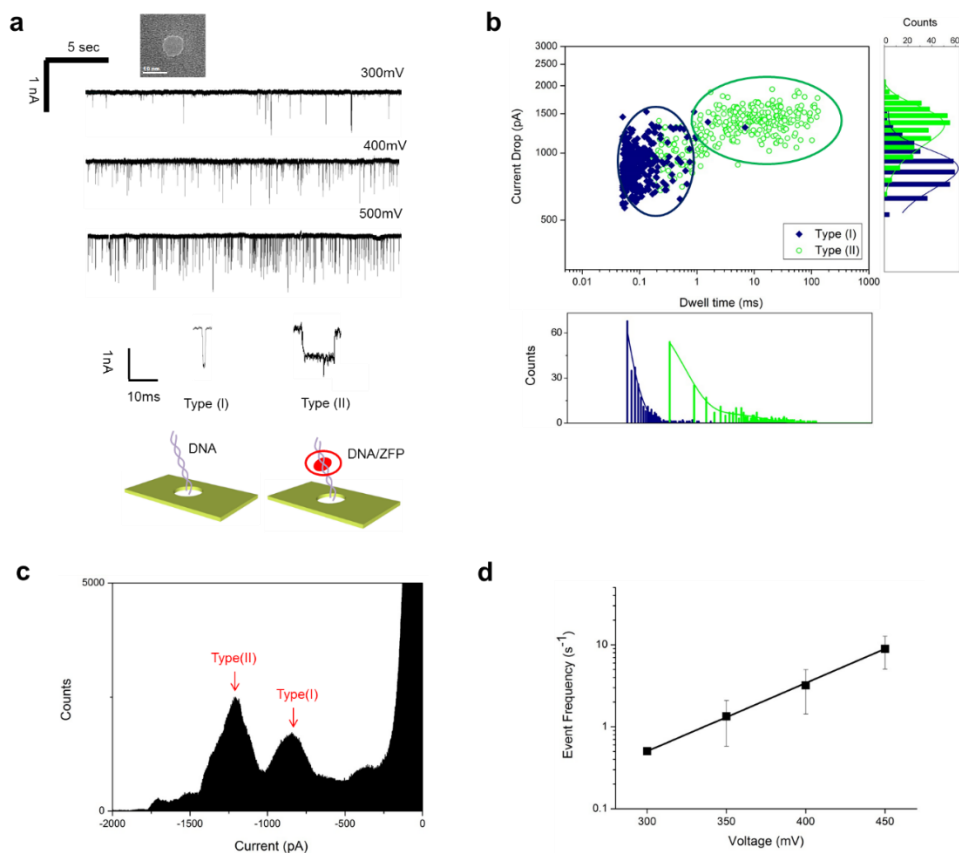


Figure 4-6. Analysis of DNA translocation events (5605 bp, binding site at 2-to-5 position) with ZFP in 500 mM KCl. (a) Current traces from the translocation of DNA-ZFP complex under three different applied voltages. Representative translocation signals from bare DNA (Type I) and DNA/ZFP (Type II) are shown. (b) Scatter plot of DNA translocation events (5605 bp)/ZFP through 7 nm nanopore on 20 nm thick SiN. Type (I) events were indicated as navy diamonds, and type (II) events were indicated as green circles, respectively. (c) All-point current histogram for DNA/ZFP translocations, showing discrete peaks for Type (I) and Type (II) events. (d) The frequency of translocation event as a function of applied voltage, which shows exponential increase of frequency upon increased voltage level.

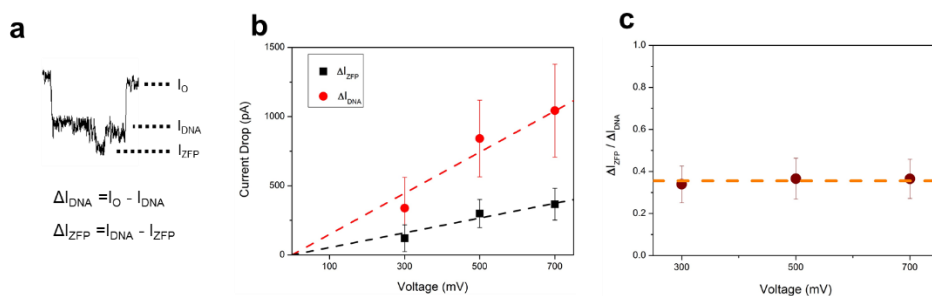


Figure 4-7. (a) A representative event signal of DNA (5606 bp)/ZFP translocations. Open pore current is indicated as I_O , the first current blockade level is I_{DNA} , and the additional current drop is I_{ZFP} . The first current drop magnitude from the open pore current ($I_O - I_{DNA}$) is indicated as ΔI_{DNA} , and the magnitude of the additional current drop ($I_{DNA} - I_{ZFP}$) is indicated as ΔI_{ZFP} . (b) Voltage dependency of ΔI_{DNA} and ΔI_{ZFP} . Both linearly increase with applied bias voltages. (c) Voltage dependency of $\Delta I_{ZFP} / \Delta I_{DNA}$. $\Delta I_{ZFP} / \Delta I_{DNA}$ is almost constant (~ 0.355) for three applied voltages.

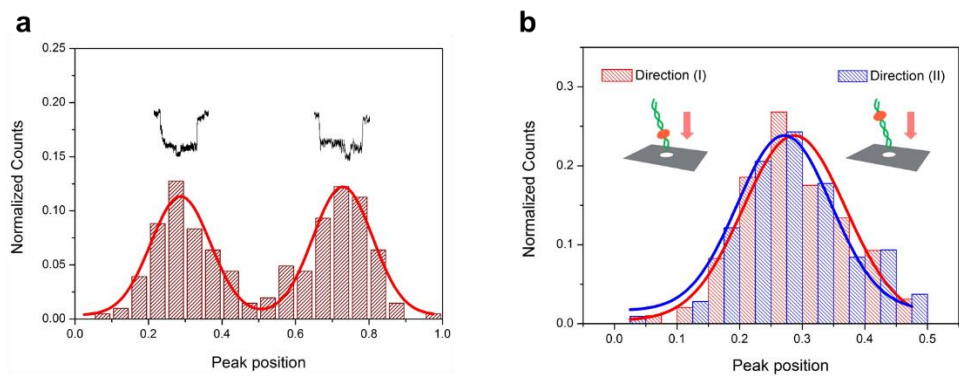


Figure 4-8. (a) Histogram of $t_1/(t_1+t_2)$, where t_1 is assigned as the dwell time from the start of event to the additional spike and t_2 is assigned as the dwell time from the additional spike to the end of the event. Two Gaussian distributions were observed due to two opposite translocation directions. (b) Histogram of t_1/t_2 , where the shorter end of DNA from the ZFP binding site is analyzed as t_1 and the longer end is analyzed as t_2 .

4.4. Summary

We have demonstrated the identifying of a protein binding site within DNA to single protein resolution using low noise solid-state nanopore. Characteristic ionic current signals arising from the passage of bare DNA and DNA/ZFP complexes enabled us to identify the location of the ZFP binding site within a DNA strand. ZFP is one of the most common transcriptional activators; thus, identification of the recognition locus within a long genomic DNA is important to understand biological phenomena and to design new drug or diagnostic tools. For this reason, nanopore technology is an ideal method to map the various ZFP binding sites along a long strand of DNA. Furthermore, our low noise nanopore device enabled us to detect the DNA/ZFP complex in a relatively low-salt environment. Because protein-DNA interactions are sensitive to salt concentrations, a reaction condition that is near physiological conditions may expand the application of nanopore devices for mapping or reading much useful genetic information in the near future.

References

1. Tupler, R.; Perini, G.; Green, M. R., Expressing the human genome. *Nature* 2001, 409 (6822), 832-833.
2. Klug, A., Co-chairman's remarks: protein designs for the specific recognition of DNA. *Gene* 1993, 135 (1–2), 83-92.
3. Posewitz, M. C.; Wilcox, D. E., Properties of the Sp1 Zinc Finger 3 Peptide: Coordination Chemistry, Redox Reactions, and Metal Binding Competition with Metallothionein. *Chemical Research in Toxicology* 1995, 8 (8), 1020-1028.
4. Kim, J.-S.; Pabo, C. O., Getting a handhold on DNA: Design of poly-zinc finger proteins with femtomolar dissociation constants. *Proceedings of the National Academy of Sciences* 1998, 95 (6), 2812-2817.
5. Urnov, F. D.; Miller, J. C.; Lee, Y.-L.; Beausejour, C. M.; Rock, J. M.; Augustus, S.; Jamieson, A. C.; Porteus, M. H.; Gregory, P. D.; Holmes, M. C., Highly efficient endogenous human gene correction using designed zinc-finger nucleases. *Nature* 2005, 435 (7042), 646-651.
6. Papworth, M.; Kolasinska, P.; Minczuk, M., Designer zinc-finger proteins and their applications. *Gene* 2006, 366 (1), 27-38.

7. Nakata, E.; Liew, F. F.; Uwatoko, C.; Kiyonaka, S.; Mori, Y.; Katsuda, Y.; Endo, M.; Sugiyama, H.; Morii, T., Zinc-Finger Proteins for Site-Specific Protein Positioning on DNA-Origami Structures. *Angewandte Chemie* 2012, 124 (10), 2471-2474.
8. Siggers, T.; Reddy, J.; Barron, B.; Bulyk, Martha L., Diversification of Transcription Factor Paralogs via Noncanonical Modularity in C2H2 Zinc Finger DNA Binding. *Molecular cell* 2014, 55 (4), 640-648.
9. Xu, S.; Wang, X.; Chen, J., Zinc finger protein 1 (ThZF1) from salt cress (*Thellungiella halophila*) is a Cys-2/His-2-type transcription factor involved in drought and salt stress. *Plant Cell Rep* 2007, 26 (4), 497-506.
10. Zimmerman, K. A.; Fischer, K. P.; Joyce, M. A.; Tyrrell, D. L. J., Zinc Finger Proteins Designed To Specifically Target Duck Hepatitis B Virus Covalently Closed Circular DNA Inhibit Viral Transcription in Tissue Culture. *Journal of Virology* 2008, 82 (16), 8013-8021.
11. Kim, S.; Gottfried, A.; Lin, R. R.; Dertinger, T.; Kim, A. S.; Chung, S.; Colyer, R. A.; Weinhold, E.; Weiss, S.; Ebenstein, Y., Enzymatically Incorporated Genomic Tags for Optical Mapping of DNA-Binding Proteins. *Angewandte Chemie International Edition* 2012, 51 (15), 3578-3581.
12. Forget, A. L.; Dombrowski, C. C.; Amitani, I.; Kowalczykowski, S. C., Exploring protein-DNA interactions in 3D using in situ construction, manipulation and

visualization of individual DNA dumbbells with optical traps, microfluidics and fluorescence microscopy. *Nat. Protocols* 2013, 8 (3), 525-538.

13. Chen, L.; Haushalter, K. A.; Lieber, C. M.; Verdine, G. L., Direct Visualization of a DNA Glycosylase Searching for Damage. *Chemistry & Biology* 2002, 9 (3), 345-350.

14. Wang, H.; Tessmer, I.; Croteau, D. L.; Erie, D. A.; Van Houten, B., Functional Characterization and Atomic Force Microscopy of a DNA Repair Protein Conjugated to a Quantum Dot. *Nano letters* 2008, 8 (6), 1631-1637.

15. Nakata, E.; Liew, F. F.; Uwatoko, C.; Kiyonaka, S.; Mori, Y.; Katsuda, Y.; Endo, M.; Sugiyama, H.; Morii, T., Zinc-Finger Proteins for Site-Specific Protein Positioning on DNA-Origami Structures. *Angewandte Chemie International Edition* 2012, 51 (10), 2421-2424.

16. Kim, M. J.; Wanunu, M.; Bell, D. C.; Meller, A., Rapid Fabrication of Uniformly Sized Nanopores and Nanopore Arrays for Parallel DNA Analysis. *Advanced Materials* 2006, 18 (23), 3149-3153.

17. Dekker, C., Solid-state nanopores. *Nat Nano* 2007, 2 (4), 209-215.

18. Branton, D.; Deamer, D. W.; Marziali, A.; Bayley, H.; Benner, S. A.; Butler, T.; Di Ventra, M.; Garaj, S.; Hibbs, A.; Huang, X.; Jovanovich, S. B.; Krstic, P. S.; Lindsay, S.; Ling, X. S.; Mastrangelo, C. H.; Meller, A.; Oliver, J. S.; Pershin, Y. V.; Ramsey, J. M.; Riehn, R.; Soni, G. V.; Tabard-Cossa, V.; Wanunu, M.; Wiggin, M.; Schloss, J. A.,

The potential and challenges of nanopore sequencing. *Nat Biotech* 2008, 26 (10), 1146-1153.

19. Li, J.; Gershow, M.; Stein, D.; Brandin, E.; Golovchenko, J. A., DNA molecules and configurations in a solid-state nanopore microscope. *Nat Mater* 2003, 2 (9), 611-615.

20. Fologea, D.; Uplinger, J.; Thomas, B.; McNabb, D. S.; Li, J., Slowing DNA Translocation in a Solid-State Nanopore. *Nano letters* 2005, 5 (9), 1734-1737.

21. Smeets, R. M. M.; Keyser, U. F.; Krapf, D.; Wu, M.-Y.; Dekker, N. H.; Dekker, C., Salt Dependence of Ion Transport and DNA Translocation through Solid-State Nanopores. *Nano letters* 2005, 6 (1), 89-95.

22. Fologea, D.; Ledden, B.; McNabb, D. S.; Li, J., Electrical characterization of protein molecules by a solid-state nanopore. *Applied Physics Letters* 2007, 91 (5), -.

23. Talaga, D. S.; Li, J., Single-Molecule Protein Unfolding in Solid State Nanopores. *Journal of the American Chemical Society* 2009, 131 (26), 9287-9297.

24. Wanunu, M.; Dadosh, T.; Ray, V.; Jin, J.; McReynolds, L.; Drndic, M., Rapid electronic detection of probe-specific microRNAs using thin nanopore sensors. *Nat Nano* 2010, 5 (11), 807-814.

25. Japrun, D.; Dogan, J.; Freedman, K. J.; Nadzeyka, A.; Bauerdick, S.; Albrecht, T.; Kim, M. J.; Jemth, P.; Edel, J. B., Single-Molecule Studies of Intrinsically Disordered Proteins Using Solid-State Nanopores. *Analytical chemistry* 2013, 85 (4), 2449-2456.
26. Kowalczyk, S. W.; Hall, A. R.; Dekker, C., Detection of Local Protein Structures along DNA Using Solid-State Nanopores. *Nano letters* 2009, 10 (1), 324-328.
27. Singer, A.; Wanunu, M.; Morrison, W.; Kuhn, H.; Frank-Kamenetskii, M.; Meller, A., Nanopore Based Sequence Specific Detection of Duplex DNA for Genomic Profiling. *Nano letters* 2010, 10 (2), 738-742.
28. Singer, A.; Rapireddy, S.; Ly, D. H.; Meller, A., Electronic Barcoding of a Viral Gene at the Single-Molecule Level. *Nano letters* 2012, 12 (3), 1722-1728.
29. Japrun, D.; Bahrami, A.; Nadzeyka, A.; Peto, L.; Bauerdick, S.; Edel, J. B.; Albrecht, T., SSB Binding to Single-Stranded DNA Probed Using Solid-State Nanopore Sensors. *The Journal of Physical Chemistry B* 2014, 118 (40), 11605-11612.
30. Carlsen, A. T.; Zahid, O. K.; Ruzicka, J. A.; Taylor, E. W.; Hall, A. R., Selective Detection and Quantification of Modified DNA with Solid-State Nanopores. *Nano letters* 2014, 14 (10), 5488-5492.
31. Bell, N. A. W.; Keyser, U. F., Specific Protein Detection Using Designed DNA Carriers and Nanopores. *Journal of the American Chemical Society* 2015, 137 (5), 2035-2041.

32. Mahmood, M. A. I.; Ali, W.; Adnan, A.; Iqbal, S. M., 3D Structural Integrity and Interactions of Single-Stranded Protein-Binding DNA in a Functionalized Nanopore. *The Journal of Physical Chemistry B* 2014, 118 (22), 5799-5806.
33. Wang, H.; Hurt, N.; Dunbar, W. B., Measuring and Modeling the Kinetics of Individual DNA–DNA Polymerase Complexes on a Nanopore. *ACS Nano* 2013, 7 (5), 3876-3886.
34. Van Meervelt, V.; Soskine, M.; Maglia, G., Detection of Two Isomeric Binding Configurations in a Protein–Aptamer Complex with a Biological Nanopore. *ACS Nano* 2014, 8 (12), 12826-12835.
35. Wang, H.-Y.; Li, Y.; Qin, L.-X.; Heyman, A.; Shoseyov, O.; Willner, I.; Long, Y.-T.; Tian, H., Single-molecule DNA detection using a novel SP1 protein nanopore. *Chemical Communications* 2013, 49 (17), 1741-1743.
36. Pomerantz, J. L.; Wolfe, S. A.; Pabo, C. O., Structure-Based Design of a Dimeric Zinc Finger Protein†. *Biochemistry* 1998, 37 (4), 965-970.
37. Moore, M.; Choo, Y.; Klug, A., Design of polyzinc finger peptides with structured linkers. *Proceedings of the National Academy of Sciences* 2001, 98 (4), 1432-1436.
38. Storm, A. J.; Chen, J. H.; Ling, X. S.; Zandbergen, H. W.; Dekker, C., Fabrication of solid-state nanopores with single-nanometre precision. *Nat Mater* 2003, 2 (8), 537-540.

39. Lee, M.-H.; Kumar, A.; Park, K.-B.; Cho, S.-Y.; Kim, H.-M.; Lim, M.-C.; Kim, Y.-R.; Kim, K.-B., A Low-Noise Solid-State Nanopore Platform Based on a Highly Insulating Substrate. *Sci. Rep.* 2014, 4.
40. Mackay, J. P.; Segal, D. J., *Engineered Zinc Finger Proteins: Methods and Protocols*. Humana Press: 2010.
41. Brinkers, S.; Dietrich, H. R. C.; de Groote, F. H.; Young, I. T.; Rieger, B., The persistence length of double stranded DNA determined using dark field tethered particle motion. *The Journal of Chemical Physics* 2009, 130 (21), -.
42. Wanunu, M.; Sutin, J.; McNally, B.; Chow, A.; Meller, A., DNA Translocation Governed by Interactions with Solid-State Nanopores. *Biophysical journal* 2008, 95 (10), 4716-4725.
43. Chen, P.; Gu, J.; Brandin, E.; Kim, Y.-R.; Wang, Q.; Branton, D., Probing Single DNA Molecule Transport Using Fabricated Nanopores. *Nano letters* 2004, 4 (11), 2293-2298.
44. Storm, A. J.; Chen, J. H.; Zandbergen, H. W.; Dekker, C., Translocation of double-strand DNA through a silicon oxide nanopore. *Physical Review E* 2005, 71 (5), 051903.
45. Lu, B.; Albertorio, F.; Hoogerheide, David P.; Golovchenko, Jene A., Origins and Consequences of Velocity Fluctuations during DNA Passage through a Nanopore. *Biophysical journal* 2011, 101 (1), 70-79.

46. Plesa, C.; van Loo, N.; Ketterer, P.; Dietz, H.; Dekker, C., Velocity of DNA during Translocation through a Solid-State Nanopore. *Nano letters* 2014.
47. Shim, J.; Humphreys, G. I.; Venkatesan, B. M.; Munz, J. M.; Zou, X.; Sathe, C.; Schulten, K.; Kosari, F.; Nardulli, A. M.; Vasmatzis, G.; Bashir, R., Detection and Quantification of Methylation in DNA using Solid-State Nanopores. *Sci. Rep.* 2013, 3.
48. Aksimentiev, A.; Heng, J. B.; Timp, G.; Schulten, K., Microscopic kinetics of DNA translocation through synthetic nanopores. *Biophysical journal* 2004, 87 (3), 2086-2097.
49. Meller, A.; Nivon, L.; Branton, D., Voltage-Driven DNA Translocations through a Nanopore. *Physical Review Letters* 2001, 86 (15), 3435-3438.
50. Keyser, U. F.; Koeleman, B. N.; van Dorp, S.; Krapf, D.; Smeets, R. M. M.; Lemay, S. G.; Dekker, N. H.; Dekker, C., Direct force measurements on DNA in a solid-state nanopore. *Nat Phys* 2006, 2 (7), 473-477.

CHAPTER 5.

Differentiation of Selectively Labeled Peptides using Solid-State Nanopores

5.1. Introduction

Proteins that make up the main structural and functional components of a cell are vital in all living organisms as they affect many cellular processes. The primary structure of a protein is known as a key factor in determining how a protein folds and functions.^{1, 2} Thus, determining a protein's amino acid sequence is important for understanding biological processes, including those in disease and aging. While mass spectrometry (MS) is a powerful tool for protein identification,³ it has fundamental limitations in detecting proteins present in a biological sample, particularly those with a large dynamic range of abundance.⁴ More specifically, low abundance proteins cannot be directly analyzed without prior enrichment processes due to the lack of sensitivity. Therefore, an alternative approach for protein sequencing is highly desired for the identification of proteins in trace amounts or those within a single cell.

Nanopore technology has emerged as a powerful platform for the detection and analysis of biomolecules, such as DNA, proteins, and peptides, as well as elucidating their interactions at the single molecule level.⁵⁻¹⁸ In a nanopore measurement, the presence of a biomolecule is sensed from the reduction of the ionic current, with the properties of the biomolecule, such as volume,^{19, 20} surface charge,²¹ folding state,²²⁻²⁴ and flexibility^{25, 26} inferred from the magnitude of current drop and translocation time distribution. Despite the high sensitivity of nanopores, protein sequencing using nanopores is challenging. Basically, it is difficult to distinguish the difference in nanopore signals from the volume differences of 20 kinds of amino acids. In addition, unlike uniformly charged DNA, the charge distribution of amino acids is so diverse that

linear translocation of protein through a nanopore by electrophoretic force is difficult. There have been efforts for protein or peptide detection using biological nanopores. For short peptides of 10-30 amino acids, structure of peptides passing through an α -hemolysin nanopore was investigated as the amino acid sequence changes,²⁷ and peptide translocation characteristics depending on the charge distribution were studied.²⁸ In addition, translocation of proteins unfolded by a denaturing agent,^{23, 29, 30} or a protein with an oligonucleotide attached to the end passed through α -hemolysin nanopore in a unfolded form was analyzed.^{22, 31, 32} On the other hand, solid-state nanopores have been used to detect protein or peptide based on the advantages of the diameter controllability and the excellent stability under a denaturing agent or a high electric field. Protein denaturation using sodium dodecyl sulfate (SDS) or urea was used to detect the translocation of protein through solid-state nanopores,^{24, 33} or unfolding or stretching of the protein at a high electric field was studied.³⁴⁻³⁶ Although the nanopore platform provides a great potential for sequencing proteins in low abundance, nanopore-based protein sequencing has not yet been achieved because it is very difficult to acquire 20 distinguishable signals derived from 20 different amino acids.³⁷

Recently, computational studies have demonstrated that readouts for only a subset of the 20 amino acids is sufficient to identify proteins.^{38,39} For instance, Yao et al. reported that the ordered detection of only two types of amino acids, cysteine and lysine, allowed for protein identification using a bioinformatics-based comparison with proteomics databases.³⁹ Inspired by these results, we attempted to use solid-state nanopore to distinguish between three peptides with very similar amino acid sequences in which the location or number of cysteine residues differed only by labeling the cysteine. Each of

the three peptide, Pep A, Pep B, and Pep C, has a cysteine at the end of the peptide, at the center, and two cysteine residues at both ends, respectively, and the cysteine residue was labeled by a negatively charged molecule, Flamma® 496. Unlabeled peptides were found to pass through the silicon nitride nanopore in the direction of the electroosmotic (EO) flow only, and differentiation of three peptides was difficult. On the other hand, peptides labeled with negatively charged molecule passed also in the electrophoretic (EP) direction as well as in the direction of EO flow. Comparing the ionic current drop in these two directions, it was confirmed that the negatively charged label changed the peptide's conformation when the peptides are passing through the nanopore in the EP direction. Moreover, peptides labeled with the negative charged molecule could be distinguished by nanopore signals, including relative current blockade, full width at half-maximum (FWHM) of the relative current blockade distribution, and peak shape patterns at the single molecule level.

5.2. Experimental details

Nanopore fabrication

The solid-state nanopores used in this study were fabricated as follows. First, 100 nm of LPCVD amorphous Si was deposited on both sides of a 300 μm thick quartz substrate. Through photolithography and SF_6 reactive ion etching (RIE), an ~ 2 μm opening was formed on one side. Using amorphous Si as a masking layer, the quartz substrate was wet etched with 49 wt% hydrogen fluoride (HF) to form a cavity. An ~ 100 μm opening was formed through the same process on the opposite a-Si layer and then connected to the previously formed cavity on the opposite side through HF wet etching.⁴⁰ Silicon nitride used as a nanopore membrane was deposited to a thickness of ~ 100 nm by LPCVD on a 500 μm Si substrate. An ~ 2 mm opening was formed through photolithography and the CF_4 RIE process, with a freestanding SiN_x layer formed by KOH wet etching. After transferring the freestanding SiN_x membrane to the 2 μm opening of the 5×5 mm² quartz substrate, the SiN_x membrane was thinned to 8–10 nm using CF_4 RIE (40 W, 0.05 mTorr, etch rate: ~ 0.5 nm/s). The nanopores were then drilled with a focused electron beam using TEM.

Nanopore measurement

Before use, the nanopore chip was cleaned with a piranha solution ($\text{H}_2\text{SO}_4:\text{H}_2\text{O}_2 = 3:1$) and rinsed in deionized water. After drying, the chip was placed in custom-made PTFE cells that were sealed using ~ 2 mm thick PDMS between the chip and cells. Both

chambers were filled with 1 M KCl containing 10 mM Tris-HCl and 1 mM EDTA buffered at pH 8.0, and unlabeled peptide or peptides labeled with flamma 496 at a concentration of 1 μ M were added to the cis chamber. Then, Ag/AgCl electrodes connected to Chimera VC100 amplifiers were immersed in both chambers. Data were collected at a sampling rate of 4.17 MHz and low-pass filtered at 200 kHz. Nanopore events were analyzed using the Transalyzer Matlab package.⁵⁰

Peptide labeling

The synthetic peptides (Pep A, Pep B, and Pep C), obtained from Pepton Inc. (Daejeon, Korea) and Flamma® 496 (BioActs, Incheon, Korea), were prepared as 10 mM stock solution in DMSO. Each peptide stock solution was further diluted to 100 μ M and mixed with n+1 equivalent (n = the number of cysteines in the peptide sequence) of Flamma® 496. Then, the mixture was diluted to a final volume of 500 μ L with DMSO and gently mixed for 4 hours at 4 °C. Peptide labeling was confirmed by SDS-PAGE (15% polyacrylamide gel), and the labeled peptides were used for nanopore measurement without further purification.

5.3. Results and Discussion

5.3.1. Schematics of the experiments

Figure 5-1a depicts the nanopore experiment as a schematic diagram. Nanopore devices comprised $5 \times 5 \text{ mm}^2$ quartz chips to reduce dielectric noise, and 8–10 nm thick low-stress low-pressure chemical vapor deposition (LPCVD) silicon nitride membranes, as previously reported.^{17, 40} Nanopores, with diameters of 1 to 2 nm, were formed on freestanding membranes by a focused electron beam using transmission electron microscopy (TEM) (Figure 5-1b). In particular, low beam current density of spot mode 3, which is ~50 % lower than the commonly used beam current density of $\sim 10^8 \text{ e/nm}^2$ in drilling silicon nitride nanopore, was utilized to make nanopores with diameters less than 2 nm. The nanopore chip was then assembled with a polydimethylsiloxane (PDMS) gasket in a polytetrafluoroethylene (PTFE) fluid cell, and both chambers were filled with 1 M KCl and TE buffer solution (10 mM Tris-HCl and 1 mM EDTA buffer, pH 8.0). Peptide samples were loaded into the cis chamber to a concentration of 1 μM and Ag/AgCl electrodes were inserted into both chambers. Since the peptides used in the experiments have a small size of ~5 kDa, the ionic current was measured with a high bandwidth Chimera VC100 amplifier using a 4.17 MHz sampling rate and low pass filtered at 200 kHz. Figure 1c shows the three types of peptides under study, consisting of either 41 (Pep A and Pep B) or 42 amino acids (Pep C) and having a slightly negative charge under the experimental conditions. Cysteine residue is present at near the C-terminus of Pep A, at the center of Pep B, and at near both termini of Pep C (see Table 1 for detailed peptide information).

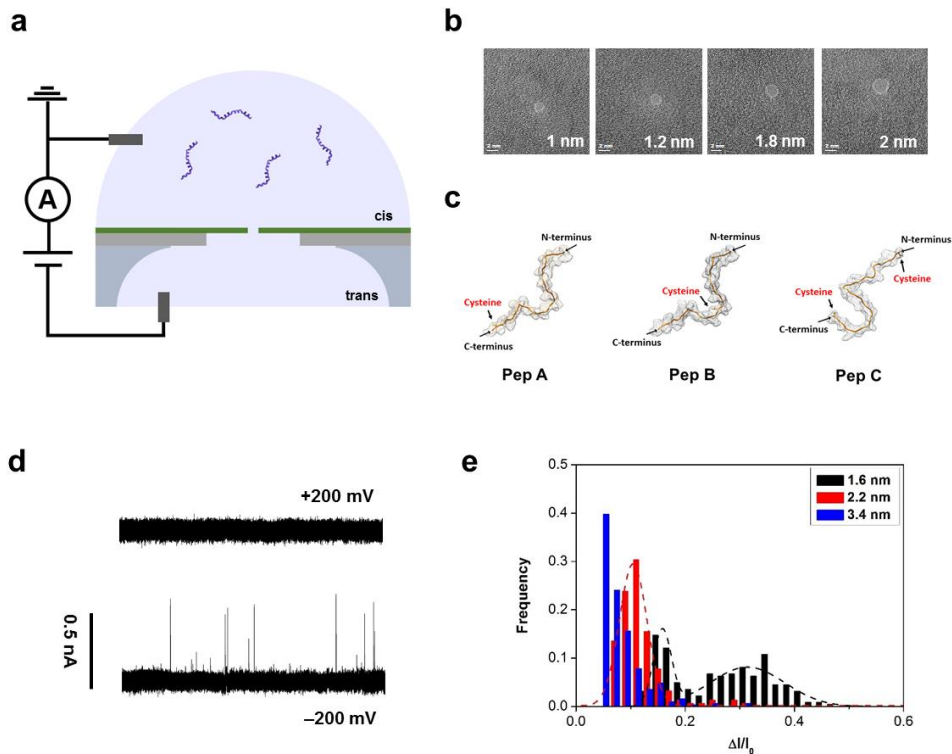


Figure 5-1. (a) Schematic diagram of the nanopore experiment (not to scale). LPCVD silicon nitride of < 10 nm thickness is used as a nanopore membrane on a quartz substrate. (b) Representative TEM images of silicon nitride nanopores of diameters < 2 nm. (c) Schematic diagrams of the three peptides of ~5 kDa used in the experiment (Detailed information is shown in Table 1 and Figure 5-2). (d) Example 2.5 s current traces of the Pep A solution when ± 200 mV is applied across the ~1.6 nm diameter nanopore. (e) $\Delta I/I_0$ distribution of Pep A translocation through three different nanopore diameters in the EO direction (black: ~1.6 nm, red: ~2.2 nm, and blue: ~3.4 nm).

Table 5-1. Characteristics of the three synthetic peptides used in the experiments

	Sequence	# of amino acids	Molecular weight (Da)	pI
Pep A	DRVYIHPFHLDRVYIHPFHLDRVYIHPFHLDRVYIHPFH <u>C</u> L	41	5231.69	7.340
Pep B	DRVYIHPFHLDRVYIHPFH <u>L</u> CDRVYIHPFHLDRVYIHPFHL	41	5231.69	7.340
Pep C	D <u>C</u> RVYIHPFHLDRVYIHPFHLDRVYIHPFHLDRVYIHPFH <u>C</u> L	42	5334.70	7.285

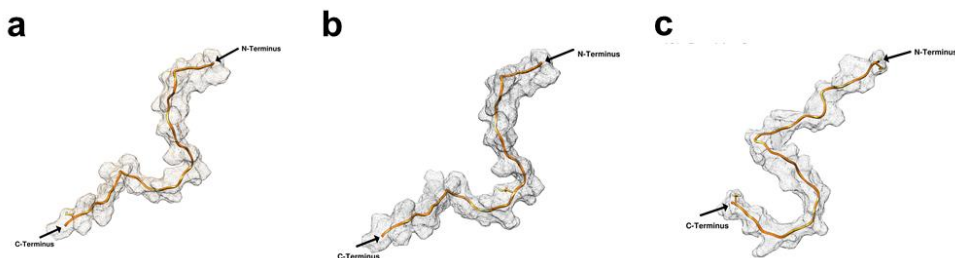


Figure 5-2. Theoretical volume of the peptides used in the experiment. (a) Pep A, (b) Pep B, and (c) Pep C.

We performed simulations using the NAMD 2.9 package with the CHARMM 27 force field with the protein parameters incorporating the CMAP. The TIP3P water model was employed. Positions for Na^+ and Cl^- ions were generated with a condition of 5 Å between ions employing the AUTOIONIZE module of VMD to approximate the system to be in the physiological condition, 150 mM in NaCl. The particle mesh Ewald (PME) method was used for electrostatic interactions. The damping coefficient was 5 ps^{-1} for Langevin dynamics. The direct space cut off was 12 Å. We performed molecular dynamics simulation in the NPT ensemble (300 K, 1 atm) for 10 ns. Peptides were modelled using Model1er 9.19. The volume of the peptides is 5287 Å³, 5278 Å³, and 5541 Å³ for Pep A, Pep B, and Pep C.

5.3.2. Electroosmotic capture of unlabeled peptides

Protein translocation events through a nanopore drastically decrease as protein size becomes smaller because of measurement limits.^{19, 41} Efficient detection can be achieved by slowing the transport velocity via a dragging interaction between the protein and pore wall, when the diameter of the nanopore is smaller than ~ 1.5 times that of the protein.^{19, 25} Since the peptides used in the present study (Pep A, Pep B, and Pep C; Table 1) were as small as ~ 5 kDa and were not expected to adopt a specific shape, such as a globular form, we first attempted to test detection efficiency using different nanopore diameters. Considering the diameters of amino acids are approximately 0.3–1 nm,⁴² nanopores having diameters of ~ 1.5 , ~ 2 , and ~ 3 nm were respectively tested. Interestingly, irrespective of pore size, Pep A translocation signals were only obtained when the negative bias was applied to the trans chamber, even though the peptide had an overall slight negative charge ($z = -0.973$ at pH 8.0) (Figure 5-1d). Silicon nitride nanopores are known to have negative surface charges at pH 8 (zeta potential of -20 mV)⁴³ and that cations accumulated at the electrical double layer generate an EO flow when a voltage is applied to the chamber, which can subsequently result in protein translocations.^{33, 43} Since the translocation of unlabeled Pep A was found to occur only in the EO flow direction, it can be assumed that the dominant factor in unlabeled Pep A translocation was EO flow instead of EP force. The velocities in both directions at high ionic strength were calculated according to the surface charge of the peptide, and for the weak charge of -0.973 e, the EO direction velocity was found to be dominant (Figure 5-3).

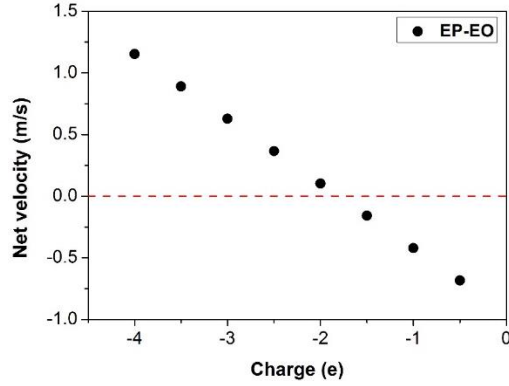


Figure 5-3. Calculated velocities of Pep A in EO and EP directions

The electrophoretic velocity, v_{EP} and electroosmotic velocity, v_{EO} of the Pep A in ionic solution can be calculated as follows. According to Stokes-Einstein relation, $v_{EP} = \mu E = \frac{qD}{k_B T} E = \frac{qE}{6\pi\eta r}$, where μ is electrophoretic mobility, E is the applied electric field, q is the charge of the peptide, D is diffusion coefficient, k_B is the Boltzmann constant, T is the absolute temperature, η is viscosity of the electrolyte solution, and r is the radius of the peptide. Since the Pep A used in the experiment did

not have a spherical shape, it was assumed $r = \sqrt[3]{\left(\frac{3}{4\pi}\right) V_{peptide}}$, where $V_{peptide}$ is the volume of the Pep A. Based on the calculation of amino acids sequences, (Figure 5-2) $V_{peptide}$ is $\sim 5.29 \text{ nm}^3$ and $r = \sim 1.08 \text{ nm}$. Using $E = 200 \text{ mV}/3 \text{ nm}$, $\eta = 10^{-3} \text{ Pa}\cdot\text{s}$, the theoretical v_{EP} was calculated according to the charge of the peptide. At a high ionic strength of 1 M, the Debye length is very thin, $\sim 0.3 \text{ nm}$, and the velocity of the electroosmotic flow, v_{EO} can be expressed as $v_{EO} = -\frac{\varepsilon_0 \varepsilon_r \zeta_{pore} E}{\eta}$, where ε_0 is vacuum permittivity and ε_r is relative permittivity, and ζ_{pore} is the zeta potential of the pore wall. Since the net velocity $v_{net} = v_{EP} - v_{EO}$ of the Pep A, having a net charge of -0.973 e , is less than 0, the EO direction translocation is more dominant.

The relative current blockade, $\Delta I/I_0$ (ΔI = magnitude of the current drop, I_0 = open pore current), and dwell time (t_D) of Pep A nanopore events at -200 mV are shown in Figure 5-1d and 5-1e at three different nanopore diameters (number of events, $n \sim 500$). For the smallest pore of 1.6 nm, the $\Delta I/I_0$ histogram showed two distinct Gaussian distributions with mean values of ~ 0.158 and ~ 0.314 , respectively. The Gaussian distribution of the smaller $\Delta I/I_0$ value is assumed to be resulted from the “bouncing” of Pep A, which partially blocked and did not fully traverse the nanopore. The larger $\Delta I/I_0$ values were considered as real translocations. The volume of the nanopore is $\sim 6.03 \text{ nm}^3$ when assuming cylindrical pore shape with an effective thickness, h_{eff} of $\sim 3 \text{ nm}$, which can be calculated from the nanopore conductance, $G = \sigma \left[\frac{4h_{\text{eff}}}{\pi d^2} + \frac{1}{d} \right]^{-1}$, where σ is the conductivity of 1 M KCl (11.1 S/m) and d is the nanopore diameter. It is also consistent with previous results that were described as $h_{\text{eff}} = h/3$,^{15, 44, 45} where h is the total thickness of the nanopore membrane, 8–10 nm in this experiment. Assuming that $\Delta I/I_0$ of ~ 0.314 reflects the relative occupied volume of the pore, a peptide volume of $\sim 1.89 \text{ nm}^3$ is inserted inside the pore. Since the volume of Pep A is $\sim 5.29 \text{ nm}^3$, based on a calculation of amino acid sequences (Figure 5-2), $\sim 35\%$ of the peptide’s total volume is instantly present in the pore. On the other hand, only one Gaussian distribution of $\Delta I/I_0$ appeared (~ 0.104) for the 2.2 nm pore, indicating the peptide rarely bounced at this nanopore diameter. For the 3.4 nm pore, $\Delta I/I_0$ distribution was not well fitted because most of the histograms were clustered on small values, with smaller $\Delta I/I_0$ values being outside the detection limit ($\Delta I > 7 \times I_{\text{RMS}}$; $I_{\text{RMS}} \sim 35 \text{ pA}$ at 200 kHz filter). This result indicates it is difficult to obtain accurate information when detecting small peptides of $\sim 5 \text{ kDa}$ using solid-state nanopores with diameters exceeding 3 nm.

5.3.3. Nanopore measurement of three unlabeled peptides

Before measuring nanopore signals for the three peptides labeled with the negatively charged molecule, we tested whether the three unlabeled peptides were distinguishable by nanopore signals (Figure 5-4). In all experiments, solid-state nanopores with diameters of 1.6–1.8 nm and 8–10 nm thickness were used. Measurements were gathered until the initial open pore conductance increased by 30% due to pore expansion. As was observed for unlabeled Pep A, all unlabeled peptides, including Pep B and Pep C, only passed through the nanopore in the EO direction (negative voltage on the trans chamber). In the case of Pep A and Pep B, which only differed by the location of one cysteine residue, the $\Delta I/I_0$ histogram showed two distinct Gaussian distributions; one from the bouncing and another one from the real translocation. The mean value of the Gaussian distribution of $\Delta I/I_0$ for Pep A, Pep B, and Pep C were $\sim 0.314 \pm 0.07$, $\sim 0.349 \pm 0.03$, and $\sim 0.310 \pm 0.07$, while the FWHM values were ~ 0.1612 , ~ 0.1466 , and ~ 0.1573 , respectively. These were not significantly different from one another (Figure 5-4d), which could result from the theoretical volume differences of the peptides not being large enough to be detected by nanopores. While the net charges of Pep A and Pep B were -0.973, and Pep C is -1.32, most translocation events were generated by the EO flow, resulting in no difference in peptide shape or flexibility when passing through the nanopores.

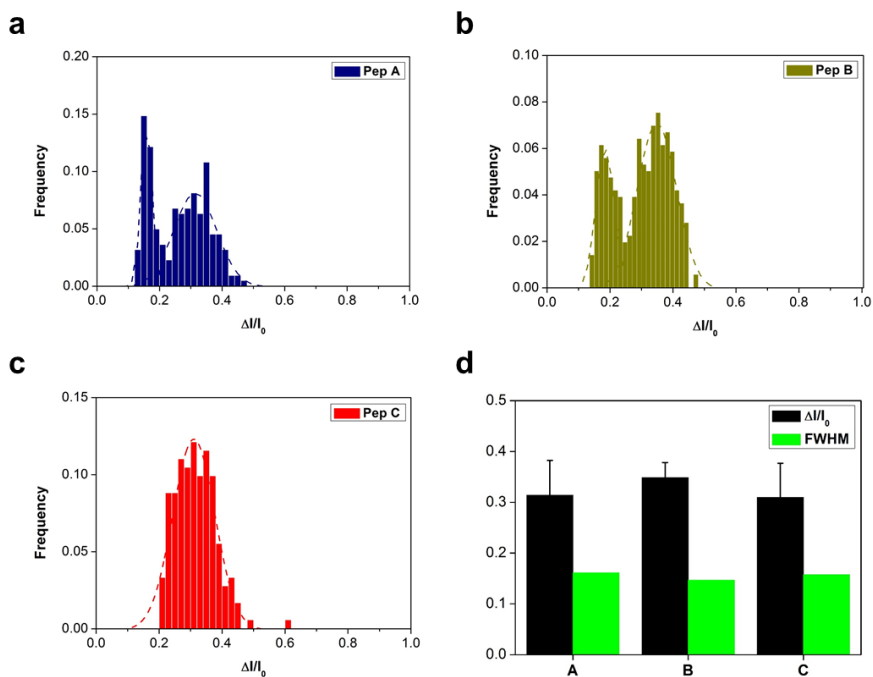


Figure 5-4. Differentiation of unlabeled peptides. (a) $\Delta I/I_0$ distribution of unlabeled Pep A (navy), (b) Pep B (dark yellow), and (c) Pep C (red) when -100 mV was applied across a 1.6–1.8 nm diameter nanopore. (d) Relative current blockade $\Delta I/I_0$ (black) and FWHM (green) of the $\Delta I/I_0$ distribution for three types of peptide.

5.3.4. Capture rate of labeled peptide in the EO and EP directions

While translocation events of unlabeled Pep A were observed by the EO flow only, Pep A in which the cysteine residue was labeled with a negatively charged fluorophore (Flamma[®] 496, $z = -2$ at pH 8.0) generated translocation signals across the nanopore with an ~ 2 nm diameter when both negative and positive voltages were applied (Figure 5-5a). Firnkes *et al.* reported that translocation occurs in both directions when zeta potentials of the protein and pore are similar.⁴³ They explained that the effective velocity of the protein is almost eliminated when EO and EP flow counterbalanced each other, with protein translocation occurring by the concentration gradient of the protein between the cis and trans chambers. However, in our experiments, it was observed that the capture rate, relative current blockade, and dwell time changed depending on the applied voltage, which would not occur if the peptides were driven by a concentration gradient. For instance, Figure 5-5b shows the capture rate of Pep A' (Pep A of which cysteine is labeled with Flamma[®] 496) in the EO (negative applied voltages) and EP (positive applied voltages) directions relative to the magnitude of the applied voltage. In here, capture rate (R_C) was obtained by fitting an exponential function in the histogram of the interval time between successive events.⁴⁶ While the R_C of Pep A' in the EO direction ($\sim 8.405 \text{ s}^{-1}$ at -50 mV) was about twice that in the EP direction ($\sim 3.907 \text{ s}^{-1}$ at $+50 \text{ mV}$) at low voltages, the difference was more than four times as the voltage was increased to 150 mV ($\sim 9.4 \text{ s}^{-1}$ at -150 mV and $\sim 1.9 \text{ s}^{-1}$ at $+150 \text{ mV}$), indicating that EO flow was dominant in the translocation event. In the EO direction, the R_C varied slightly for voltages within the error ranges ($\sim 10\%$ increase from -50 mV to -150 mV),

whereas the RC in the EP direction exponentially decreased for the applied voltages (R^2 of linear fit ~ 0.80 , and R^2 of exponential fit ~ 0.98) by $\sim 50\%$ from +50 mV to +150 mV.

The capture rate of a protein is described as a diffusion-limited model or an energy barrier model that is described as $R = R_0 \exp\left(\frac{|V|}{V_0}\right)$, where $R_0 \propto \nu \times \exp\left(\frac{-U'}{k_B T}\right)$ is the capture rate at zero voltage, V is the applied voltage, V_0 is the required applied voltage to overcome the Brownian motion ($V_0 = k_B T / ze$; where k_B is the Boltzmann constant, T is temperature, z is total number of elementary charges, and e is the elementary charge), U' is an energy barrier, and ν is a frequency factor.^{35, 47} In this equation, when the energy barrier U' is constant, the capture rate in the EP direction exponentially increases as the applied voltage increases, which is the case when the pore radius is much larger than the Debye length (the ratio of Debye length to the pore radius is ~ 0.03 in ref. 33).³⁵ In our experiments, the ratio of Debye length to the pore radius is as high as ~ 0.3 , in which the EO flow can be dominant and the energy barrier U' for peptide translocation can be increased with voltage. This result is consistent with a previous report, in which translocation frequency of peptides in the EP direction through an α -hemolysin nanopore decreased as the applied voltage increased when EO flow was opposite to the EP direction.⁴⁸

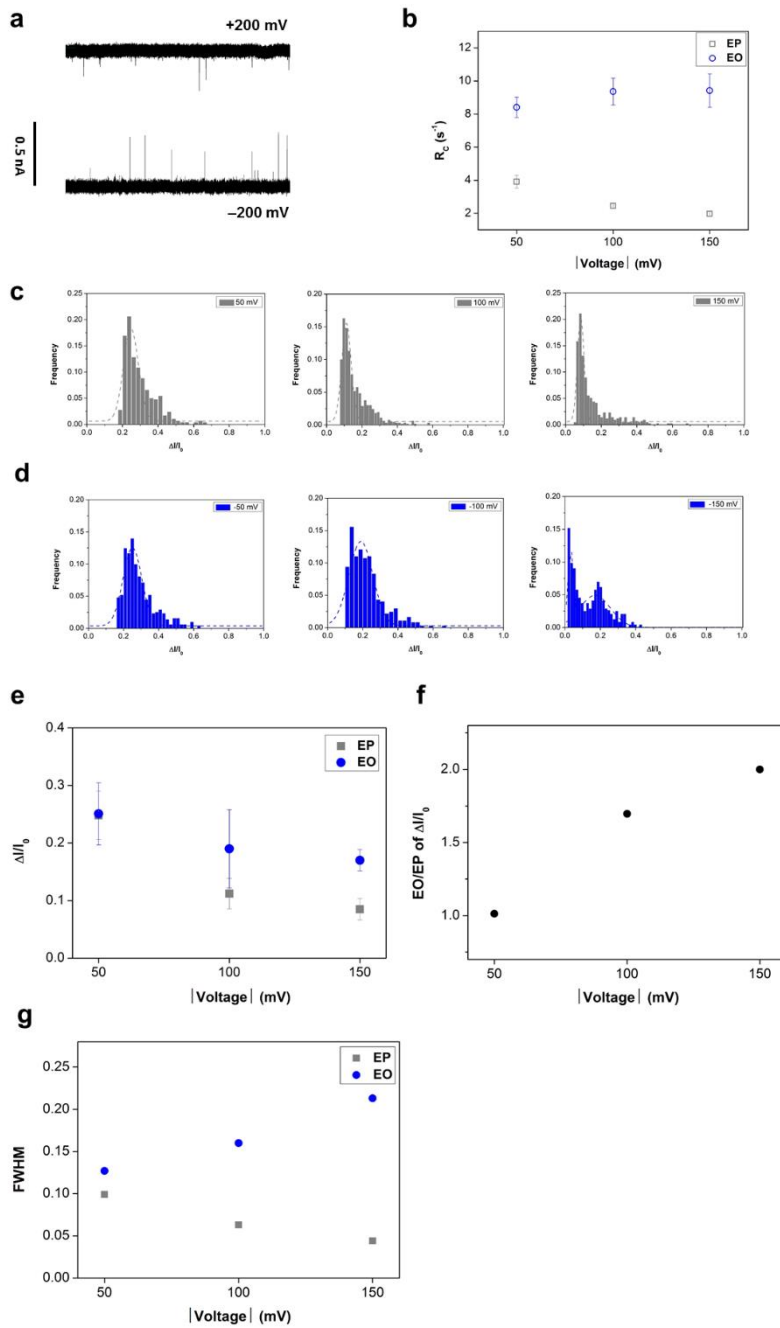


Figure 5-5. Comparison of translocation characteristics of EO and EP directions of Pep A labeled with the negatively charged molecule. (a) Example 2.5 s current traces of the labeled Pep A solution when ± 200 mV is applied across an ~ 1.8 nm diameter nanopore.

(b) Capture rate, R_C , of labeled Pep A through a nanopore in the EO (blue circle) and EP (gray square) directions, respectively, according to the magnitude of applied voltage from -50 mV to -150 mV and +50 mV to +150 mV. (c) $\Delta I/I_0$ distribution of labeled Pep A at 50, 100, and 150 mV resulting from EP force, and (d) $\Delta I/I_0$ distribution of labeled Pep A at -50, -100, and -150 mV resulting from EO flow. (e) Comparison of $\Delta I/I_0$ in EO and EP directions according to the magnitude of the negative and positive voltages, respectively. (f) The ratio of $\Delta I/I_0$ in the EO compared to EP direction according to the voltages. (g) FWHM of $\Delta I/I_0$ distributions in the EO and EP directions, according to the negative and positive voltages, respectively.

5.3.5. Stretching of labeled peptide in the EP direction

The Pep A' was translocated through the nanopore by the EP and EO direction, respectively, with the histograms of the relative current blockade ($\Delta I/I_0$) shown in Figures 5-5c and 5d. At ± 50 mV, the $\Delta I/I_0$ values were similar in both directions ($\sim 0.248 \pm 0.04$ in EP direction and $\sim 0.251 \pm 0.05$ in EO direction). However, at ± 100 and ± 150 mV, the $\Delta I/I_0$ values were larger in the EO direction translocation (0.190 ± 0.07 and 0.170 ± 0.02 for -100 and -150 mV, respectively) than the EP translocation (0.112 ± 0.03 and 0.085 ± 0.02 for $+100$ and $+150$ mV, respectively), even though the same peptides passed through the nanopore with the same dimension (Figure 5-5e). This result indicates that peptide volume in the pore is larger in the EO direction, and that peptide conformations can differ between the two directions. If the nanopore's effective thickness is greater than the full length of the peptide, $\Delta I/I_0$ will not vary during translocation irrespective of peptide conformation. However, since the effective thickness of the nanopore used in these experiments is ~ 3 nm, and the full length of the peptide is ~ 10 nm, $\Delta I/I_0$ can vary depending on peptide translocation conformation. In the EO direction, there is no reason for the peptide to adopt a specific conformation. On the other hand, in the EP direction, since the negatively charged molecule Flamma[®] 496 is attached to the cysteine residue located near the peptide's C-terminus, Pep A' can be pulled into the nanopore by the electric field. It can thus be assumed that the overall peptide shape is stretched and the volume of peptide present inside the nanopore would be smaller than in the EO direction. This becomes clearer when comparing the differences between $\Delta I/I_0$ in both directions according to the applied voltage.

At low voltage (± 50 mV), $\Delta I/I_0$ values in both directions were almost the same, but $\Delta I/I_0$ values in the EO direction were ~ 1.7 times larger than those in the EP direction at 100 mV and ~ 2 times larger at 150 mV (Figure 5-5f). In the EP direction, the electrical force exerted on Pep A' became larger and the peptide appeared to become more stretched during translocation at higher voltages. These results were consistent with the full-width at half-maximum (FWHM) of the Gaussian fitting of the $\Delta I/I_0$ histogram, indicating the variety of peptide shape or flexibility during nanopore translocation (Figure 5-5g).^{25, 26} The FWHM of the $\Delta I/I_0$ histogram was larger in the EO direction than the EP direction at all voltage ranges indicating that the shape of the Pep A' in the EP direction was limited to the stretched form by the charged label. Increasing FWHM of the $\Delta I/I_0$ histogram in the EO direction with the applied voltages could result from measurement limitations. When the peptide dwell time was less than twice the rise time of the filter (in these experiments, ~ 3.3 μ s for 200 kHz low-pass filter), the translocation signals were distorted and the distribution of $\Delta I/I_0$ could be broadened.^{26, 41} The dwell time of EP and EO translocation events at ± 100 (~ 3.1 and ~ 3.5 μ s for EP and EO, respectively) and ± 150 mV (~ 2.9 and ~ 3.2 μ s for EP and EO, respectively) are close to the signal distortion limits (Figure 5-6). On the other hand, the FWHM of the $\Delta I/I_0$ histogram in the EP direction was reduced because the stretching effect was increased with the applied voltages, resulting in limited shapes for Pep A'.

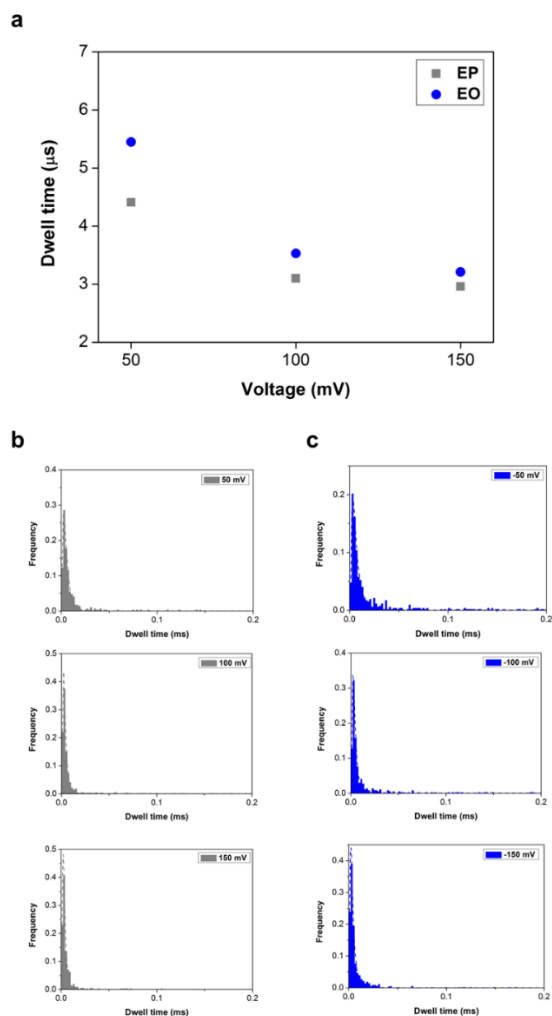


Figure 5-6. Dwell time of the labeled Pep A. (a) Dwell time of the labeled Pep A in EO and EP direction translocations according to the applied voltages. Dwell time distributions for each voltage in (b) EP direction and (c) EO direction. In the EP translocation, the dwell time is 4.4, 3.1, and 2.9 μs at 50, 100, and 150 mV, respectively. In the EO translocation, the dwell time is 5.4, 3.5, and 3.2 μs at 50, 100, and 150 mV, respectively. The dwell time at 100 and 150 mV in both directions are close to the measurement limit for the signal distortion. ($\sim 3.3 \mu\text{s}$ at 200 kHz low-pass filter)

5.3.6. Nanopore measurement of three labeled peptides

Thus far, we found a stretching of Pep A' when it was passed through the nanopore by EP force. If Pep B and Pep C (Table 1) were labeled with the same charged molecule, they could also pass through the nanopore in different conformations and thereby show distinct signal characteristics. For the measurement of translocation in the EP direction of Pep A, Pep B, and Pep C labeled with Flamma[®] 496, positive voltages were applied to the trans chamber in order to observe translocations. As was observed for Pep A' in Figure 5-5, it was expected that the electrical force exerted on the labeled peptides would increase as the applied voltage increased, resulting in characteristic translocation conformations for each peptide. When +200 mV was applied, translocation of all three labeled peptides occurred through nanopores 1.5–1.8 nm in diameter and 8–10 nm thick. Unlike unlabeled peptides, the $\Delta I/I_0$ distributions of the three labeled peptides exhibited different characteristics (Figure 5-7). First, in the case of Pep A labeled near the C terminus, the $\Delta I/I_0$ histogram shows one Gaussian distribution with a mean value of $\sim 0.144 \pm 0.03$ and FWHM of ~ 0.038 . The $\Delta I/I_0$ of Pep B', which was labeled at its center, was $\sim 0.209 \pm 0.06$, $\sim 45\%$ higher than that of Pep A', with the FWHM of the $\Delta I/I_0$ distribution being ~ 0.142 , which was also significantly larger than that of Pep A'. The significant differences in the translocation event characteristics of the Pep A' and Pep B' can be attributed to the location of the negative charged molecule attached to the cysteine residue. Location of the charged molecule near the peptide's C-terminus can stretch the entire peptide when the Pep A' passes through the nanopore due to the electric

field. That is, the volume occupied by Pep A' inside the nanopore and the flexibility or variety of shape of Pep A' can be smaller than that of Pep B'.

Similarly, the larger $\Delta I/I_0$ distribution of Pep B' could result from translocation through the nanopore in a folded form due to a charged label being located at the center of the peptide. The difference in the FWHM of $\Delta I/I_0$ distribution of Pep A' and Pep B' could be explained by the folded shape of Pep B'. Since the volume of Pep B' inside the pore is larger than that of Pep A', interactions with the pore wall and resulting fluctuations could be more significant, leading to larger variation in $\Delta I/I_0$ distribution. As for Pep C', the histogram of $\Delta I/I_0$ showed two distinct Gaussian distributions that had $\Delta I/I_0$ values of $\sim 0.252 \pm 0.02$ and $\sim 0.314 \pm 0.03$, and FWHM of ~ 0.051 and ~ 0.061 , respectively. We previously assumed that the first of the two Gaussian distributions of the $\Delta I/I_0$ histogram observed for the unlabeled peptides in the EO direction resulted from "bouncing" events. However, in this case, the lower $\Delta I/I_0$ distribution of Pep C' showed a significant blockade of ~ 0.252 , with the difference with the larger $\Delta I/I_0$ value (~ 0.314) only being $\sim 25\%$. Therefore, the two Gaussian distributions are considered to arise from two different conformations when Pep C' passed through the nanopore. For the lower $\Delta I/I_0$ distribution of $\sim 0.252 \pm 0.02$, Pep C' could pass through the nanopore as a stretched form with a charged label at both ends of the peptide, i.e. the maximum current drop is determined when one label of the peptide is inserted in the nanopore. The higher $\Delta I/I_0$ distribution implies Pep C' adopted a folded form, whereby two charged labels were inserted together in the nanopore, leading to a current drop increase of $\sim 25\%$.

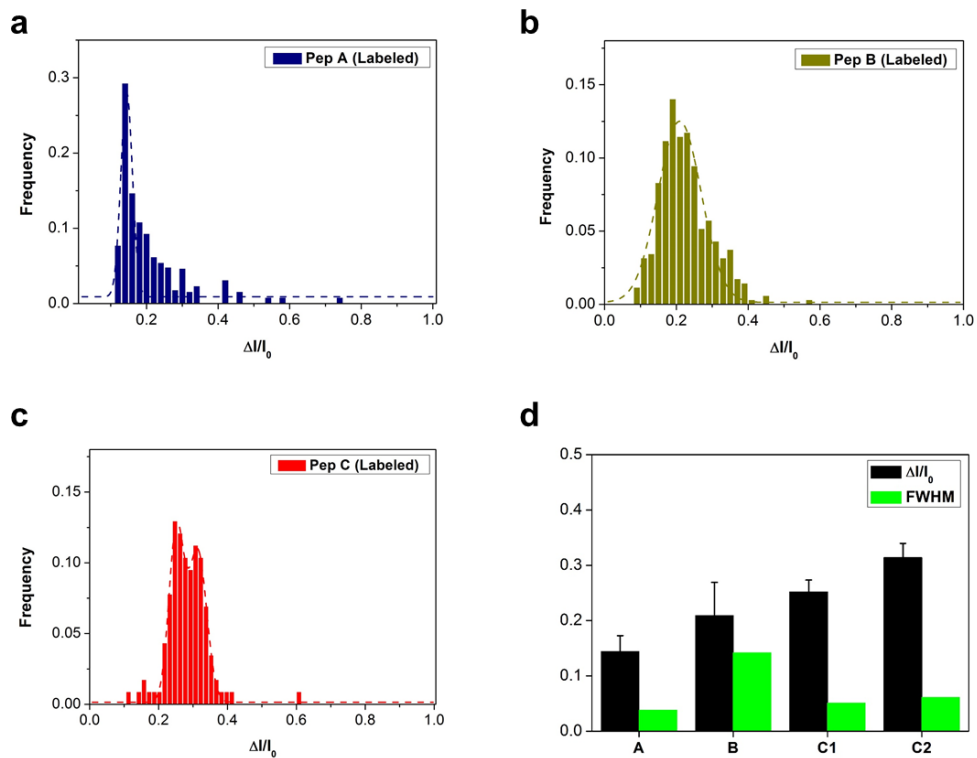


Figure 5-7. Differentiation of labeled peptides. (a) $\Delta I/I_0$ distribution of Pep A' (navy), (b) Pep B' (dark yellow), and (c) Pep C' (red) when +200 mV was applied across a 1.5–1.8 nm diameter nanopore. (d) Relative current blockade $\Delta I/I_0$ and FWHM of the $\Delta I/I_0$ distribution for three types of labeled peptides. Pep C shows two distinct $\Delta I/I_0$ distributions (C1 and C2).

5.3.7. Comparison of peak shapes of the three labeled peptides

The signals generated from peptide translocations through a nanopore also reflect the shape of the peptide at the single molecule level, which is an advantage of nanopore technology.^{24, 36, 49} Figure 5-8a shows the four most typical peak shapes that occurred in the translocation of the labeled peptides under a voltage of +200 mV. Single step events that do not have an additional peak account for ~50% of all events. This seems to be due to the limitations of insufficient time resolution such that the additional current drop caused by the negatively charged label cannot be distinguished. The average dwell time of the single step event is ~9 μ s which is ~1.7 times faster than that of other peak shapes (~15 μ s, Figure 5-9). In addition to the peak shape of single step events, the characteristic peak shapes were classified into three types: (1) double peaks, (2) a peak at the entrance, and (3) a peak at the end. All three types of peaks were selected when an additional current drop was more than three times the I_{RMS} of the open pore current. Figure 5-8c shows the percentage of the three types of peak shape patterns in translocation events of Pep A', Pep B', and Pep C' and peaks with too complicated shapes are unclassified. The percentage of unclassified events was ~8, ~9, and ~16% for Pep A', Pep B', and Pep C', respectively. There is a large portion of events with complicated shapes in the case of Pep C', because two labels of two cysteine residues can generate various nanopore signals.

In the case of Pep A', peak shape 1 (~52.7%) and 2 (31.6%) were dominant. As can be seen in Figure 5-8b, peak shape 2 is predictable because the negatively charged label located near the C-terminus of Pep A' can lead to a typical translocation event for the

peptide. Peak shape 1 can result from the translocation in which the backside of the peptide is not sufficiently stretched. Pep C' has a similar ratio to Pep A' in peak shape 1 (~55 %) and 3 (~8.3 %), while peak shape 2 is relatively low (~20 %). Peak shape 1 (double peaks) indicates that no two labels are present in the pore at the same time because the two charged labels of Pep C' are separated at both ends. Also, the Pep C' has a low percentage of the peak shape 2 which shows the flat current level at the backside because there are labels at both ends, which can generate additional current drops. On the other hand, peak shape 3 (a peak at the end) was the most dominant for Pep B' (~42.3 %). This is a counterintuitive result because the label at the center of Pep B' enters the pore while folding the peptide and thus peak shape 2 (a peak at the entrance) was expected to be the most probable. We interpreted these results as follows. Unlike Pep A' and Pep C', folding of Pep B' by the negatively charged label at the center is more likely to be stuck at the nanopore entrance. Therefore, it can be considered that the initial part (lower current drop) of peak shape 3 is likely due to the bulky conformation of folded Pep B' entering the pore inlet and partially blocking it, with the latter part (maximum current drop) showing the complete translocation of the Pep B'. This suggestion is more convincing when comparing the peak shape ratios of Pep B' at a lower applied voltage. At +100 mV, the percentage of peak shape 3 decreases to less than half that seen at +200 mV (~18 %, Figure 5-10). This suggests that at +200 mV, where the EP force is relatively strong, the bulky structure of Pep B' is more likely to be forced to pass through the pore, resulting more number of peak shape 3.

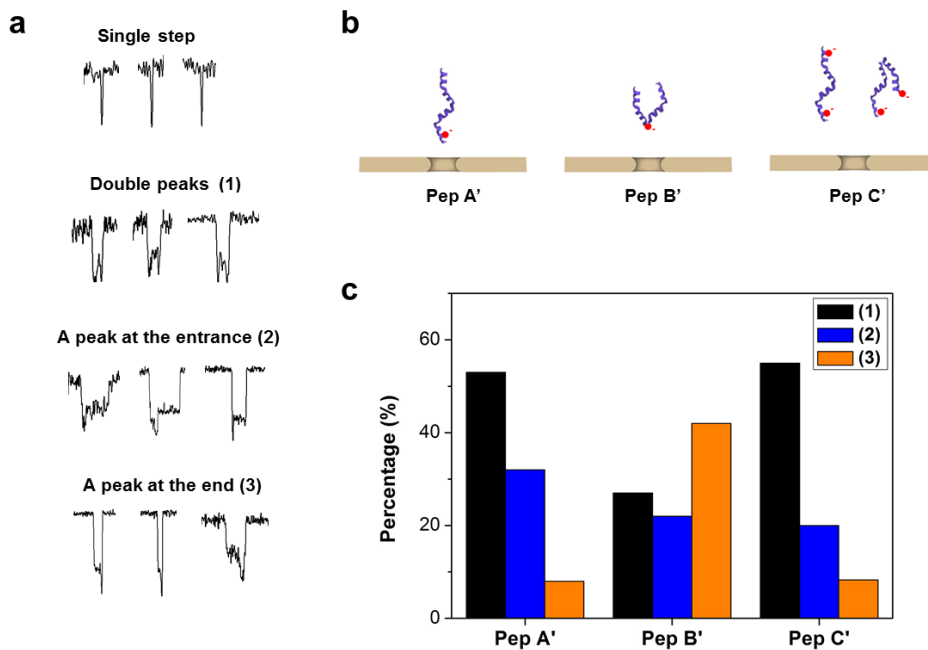


Figure 5-8. Single molecule level analysis. (a) Representative events of four most typical peak shapes of nanopore translocation of labeled peptides under +200 mV voltage. (b) Schematic diagrams of the conformations of each labeled peptide under an electric field. (c) Comparison of the three types of peak shape occurrence rates in translocation events of the three labeled peptides.

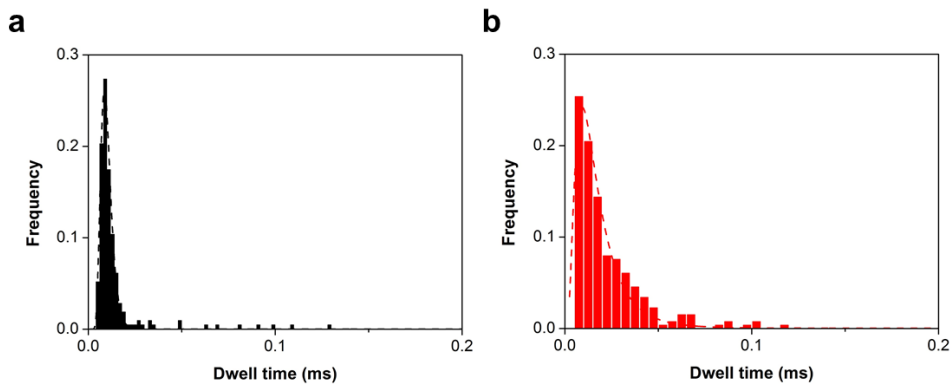


Figure 5-9. Dwell time of single step events and peaks with specific conformations. (a) Dwell time of single step events occurred in the translocation of the labeled peptides. Dwell time of $\sim 9 \mu\text{s}$ is obtained from the log-normal distribution fitting. (b) Dwell time of peak shape (1) - (3) occurred in the translocation of labeled peptides. Dwell time of $\sim 15 \mu\text{s}$ is obtained from the log-normal distribution fitting.

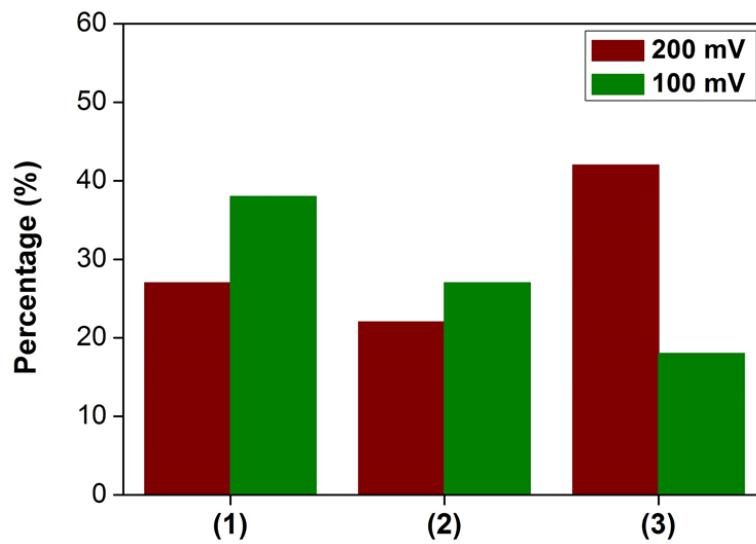


Figure 5-10. Peak shape occurrence ratio of the Pep B' at different applied voltages. (+100 and +200 mV)

Peak shape (3) decreased to less than half at 100 mV (~18 %) than at 200 mV (~42 %).

5.4. Summary

In this study, we used a low noise solid-state nanopore to detect small peptides of ~5 kDa and confirmed detection efficiency according to the pore diameters. While unlabeled peptides with weak surface charge were found to pass through the nanopore by EO flow only, peptides labeled with a negatively charged molecule passed through the nanopore in the EP as well as EO flow direction. We also demonstrated that the charged label enabled determination of the peptides' conformations during translocation by comparing capture rate, relative current blockade, and FWHM values of the relative current blockade distribution according to the applied voltages. As for the three peptides labeled in different positions, depending on the location or number of cysteine residues, the shape of each peptide was successfully differentiated based on the characteristics of the nanopore events and peak shape patterns at the single molecule level. More direct information to predict the number and location of a specific residue such as cysteine or lysine from nanopore signals is still needed for protein sequencing using a bioinformatics-based comparison with proteomics databases. We assume that a peptide structure with a charged label attached at one end leading the peptide in a stretched form and neutral labels attached to specific amino acid residues which can generate additional current drops could be helpful in future work. Although further work is required, the results of our current study provide a step toward protein sequencing using solid-state nanopores.

References

1. B. Alberts, *Molecular Biology of the Cell*, 2002, 615-657.
2. W. T. Clark and P. Radivojac, *Proteins: Structure, Function, and Bioinformatics*, 2011, 79, 2086-2096.
3. T. E. Angel, U. K. Aryal, S. M. Hengel, E. S. Baker, R. T. Kelly, E. W. Robinson and R. D. Smith, *Chemical Society Reviews*, 2012, 41, 3912-3928.
4. J. Eriksson and D. Fenyö, *Nature biotechnology*, 2007, 25, 651.
5. K. Chen, M. Juhasz, F. Gularek, E. Weinhold, Y. Tian, U. F. Keyser and N. A. Bell, *Nano letters*, 2017, 17, 5199-5205.
6. M. Chinappi and F. Cecconi, *Journal of Physics: Condensed Matter*, 2018, 30, 204002.
7. J. Clarke, H.-C. Wu, L. Jayasinghe, A. Patel, S. Reid and H. Bayley, *Nature nanotechnology*, 2009, 4, 265.
8. J. Kong, J. Zhu and U. F. Keyser, *Chemical Communications*, 2017, 53, 436-439.
9. S. W. Kowalczyk, A. R. Hall and C. Dekker, *Nano letters*, 2009, 10, 324-328.
10. W. Li, N. A. Bell, S. Hernández-Ainsa, V. V. Thacker, A. M. Thackray, R. Bujdoso and U. F. Keyser, *ACS nano*, 2013, 7, 4129-4134.

11. E. A. Manrao, I. M. Derrington, A. H. Laszlo, K. W. Langford, M. K. Hopper, N. Gillgren, M. Pavlenok, M. Niederweis and J. H. Gundlach, *Nature biotechnology*, 2012, 30, 349.
12. J. Shim, G. I. Humphreys, B. M. Venkatesan, J. M. Munz, X. Zou, C. Sathe, K. Schulten, F. Kosari, A. M. Nardulli and G. Vasmatzis, *Scientific reports*, 2013, 3, 1389.
13. A. Singer, M. Wanunu, W. Morrison, H. Kuhn, M. Frank-Kamenetskii and A. Meller, *Nano letters*, 2010, 10, 738-742.
14. R. Smeets, S. W. Kowalczyk, A. Hall, N. Dekker and C. Dekker, *Nano letters*, 2008, 9, 3089-3095.
15. M. Wanunu, T. Dadosh, V. Ray, J. Jin, L. McReynolds and M. Drndić, *Nature nanotechnology*, 2010, 5, 807.
16. M. Wanunu, J. Sutin and A. Meller, *Nano letters*, 2009, 9, 3498-3502.
17. J.-S. Yu, M.-C. Lim, D. T. N. Huynh, H.-J. Kim, H.-M. Kim, Y.-R. Kim and K.-B. Kim, *ACS nano*, 2015, 9, 5289-5298.
18. E. C. Yusko, J. M. Johnson, S. Majd, P. Prangkio, R. C. Rollings, J. Li, J. Yang and M. Mayer, *Nature nanotechnology*, 2011, 6, 253.
19. J. Larkin, R. Y. Henley, M. Muthukumar, J. K. Rosenstein and M. Wanunu, *Biophysical journal*, 2014, 106, 696-704.

20. D. J. Niedzwiecki, C. J. Lanci, G. Shemer, P. S. Cheng, J. G. Saven and M. Drndic, *ACS nano*, 2015, 9, 8907-8915.
21. D. Fologea, B. Ledden, D. S. McNabb and J. Li, *Applied physics letters*, 2007, 91, 053901.
22. D. Rodriguez-Larrea and H. Bayley, *Nature nanotechnology*, 2013, 8, 288.
23. G. Oukhaled, J. Mathe, A.-L. Biance, L. Bacri, J.-M. Betton, D. Lairez, J. Pelta and L. Auvray, *Physical review letters*, 2007, 98, 158101.
24. D. S. Talaga and J. Li, *Journal of the American Chemical Society*, 2009, 131, 9287-9297.
25. P. Waduge, R. Hu, P. Bandarkar, H. Yamazaki, B. Cressiot, Q. Zhao, P. C. Whitford and M. Wanunu, *ACS nano*, 2017, 11, 5706-5716.
26. R. Hu, J. V. Rodrigues, P. Waduge, H. Yamazaki, B. Cressiot, Y. Chishti, L. Makowski, D. Yu, E. Shakhnovich and Q. Zhao, *ACS nano*, 2018, 12, 4494-4502.
27. T. C. Sutherland, Y.-T. Long, R.-I. Stefureac, I. Bediako-Amoa, H.-B. Kraatz and J. S. Lee, *Nano letters*, 2004, 4, 1273-1277.
28. R. Stefureac, Y.-t. Long, H.-B. Kraatz, P. Howard and J. S. Lee, *Biochemistry*, 2006, 45, 9172-9179.

29. M. Pastoriza-Gallego, L. Rabah, G. Gibrat, B. Thiebot, F. o. G. van der Goot, L. Auvray, J.-M. Betton and J. Pelta, *Journal of the American Chemical Society*, 2011, 133, 2923-2931.
30. C. I. Merstorf, B. Cressiot, M. Pastoriza-Gallego, A. Oukhaled, J.-M. Betton, L. Auvray and J. Pelta, *ACS chemical biology*, 2012, 7, 652-658.
31. D. Rodriguez-Larrea and H. Bayley, *Nature communications*, 2014, 5, 4841.
32. M. Pastoriza-Gallego, M.-F. Breton, F. Discala, L. Auvray, J.-M. Betton and J. Pelta, *ACS nano*, 2014, 8, 11350-11360.
33. L. Restrepo-Pérez, S. John, A. Aksimentiev, C. Joo and C. Dekker, *Nanoscale*, 2017, 9, 11685-11693.
34. B. Cressiot, A. Oukhaled, G. Patriarche, M. Pastoriza-Gallego, J.-M. Betton, L. c. Auvray, M. Muthukumar, L. Bacri and J. Pelta, *ACS nano*, 2012, 6, 6236-6243.
35. A. Oukhaled, B. Cressiot, L. Bacri, M. Pastoriza-Gallego, J.-M. Betton, E. Bourhis, R. Jede, J. Gierak, L. c. Auvray and J. Pelta, *ACS nano*, 2011, 5, 3628-3638.
36. K. J. Freedman, S. R. Haq, J. B. Edel, P. Jemth and M. J. Kim, *Scientific reports*, 2013, 3, 1638.
37. E. Kennedy, Z. Dong, C. Tennant and G. Timp, *Nature nanotechnology*, 2016, 11, 968.

38. J. Swaminathan, A. A. Boulgakov and E. M. Marcotte, PLoS computational biology, 2015, 11, e1004080.
39. Y. Yao, M. Docter, J. Van Ginkel, D. de Ridder and C. Joo, Physical biology, 2015, 12, 055003.
40. M.-H. Lee, A. Kumar, K.-B. Park, S.-Y. Cho, H.-M. Kim, M.-C. Lim, Y.-R. Kim and K.-B. Kim, Scientific reports, 2014, 4, 7448.
41. C. Plesa, S. W. Kowalczyk, R. Zinsmeister, A. Y. Grosberg, Y. Rabin and C. Dekker, Nano letters, 2013, 13, 658-663.
42. C. Ching, K. Hidajat and M. Uddin, Separation Science and Technology, 1989, 24, 581-597.
43. M. Firnkes, D. Pedone, J. Knezevic, M. Doblinger and U. Rant, Nano letters, 2010, 10, 2162-2167.
44. M. J. Kim, M. Wanunu, D. C. Bell and A. Meller, Advanced materials, 2006, 18, 3149-3153.
45. I. Yanagi, R. Akahori, T. Hatano and K.-i. Takeda, Scientific reports, 2014, 4, 5000.
46. A. Meller and D. Branton, Electrophoresis, 2002, 23, 2583-2591.
47. S. E. Henrickson, M. Misakian, B. Robertson and J. J. Kasianowicz, Physical Review Letters, 2000, 85, 3057.

48. A. Asandei, I. Schiopu, M. Chinappi, C. H. Seo, Y. Park and T. Luchian, *ACS applied materials & interfaces*, 2016, 8, 13166-13179.
49. E. C. Yusko, B. R. Bruhn, O. M. Eggenberger, J. Houghtaling, R. C. Rollings, N. C. Walsh, S. Nandivada, M. Pindrus, A. R. Hall and D. Sept, *Nature nanotechnology*, 2017, 12, 360.
50. C. Plesa and C. Dekker, *Nanotechnology*, 2015, 26, 084003.

CHAPTER 6.

Summary and Conclusions

Nanopore technology, which first appeared in the late 90s, has been studied intensively during the last two decades. Nanopores have been used as an efficient and accurate tool for analyzing small biomolecules such as DNA, RNA, proteins, and peptides based on its advantages of label-free, high-throughput, low cost and single-molecule level detection. At first, biological nanopores have been studied for the purpose of DNA sequencing, and after 5 years, their counterparts solid-state nanopores have been developed. The advent and development of solid-state nanopores enabled the expansion of a variety of analytes. This dissertation mainly focused on improvements in the noise property and stability of solid-state nanopore devices, and biological applications that were previously difficult to analyze, using the improved nanopore devices.

Chapter 2 described the limitations of the quartz based nanopore platform, which reduced the dielectric noise of solid-state nanopores, and results for new nanopore devices that have improved the limitations. The problems caused by using PECVD SiN membrane such as nanopore expansion, chemical stability, protein adsorption at the SiN surface, and increase in $1/f$ noise were solved by the development of a transfer processes using LPCVD SiN membrane. The LPCVD SiN nanopore device has excellent stability in measurement and a clean and uniform SiN surface, which significantly improves measurement time and reproducibility of nanopore experiments. The low noise LPCVD SiN nanopore devices have been registered as a domestic patent and a US patent pending, and commercialized and sold domestically and internationally for past several years.

Chapter 3 introduced the results of using a biological material as a nanopore

membrane, on a solid-state substrate. The YFCFY peptide used in this study forms a stable film by self-assembly at the air/water interface and has advantages of simple preparation method, quick film formation time, and thin thickness of ~ 5 nm. The peptide nanopore has a comparable noise property to the conventional SiN nanopores or the multilayered 2D nanopores. The DNA translocation events through the peptide nanopore were obtained at a sufficient signal-to-noise ratio of ~ 30 and the slow translocation speed of ~ 1 bp/ μ s due to the interactions between DNA bases and amino acids. These results suggest the possibility of incorporation of biological functionalities to solid-state nanopores.

Chapter 4 described the results of detection and analysis of interaction between DNA and ZFP at a single-molecule level using the low noise LPCVD SiN nanopores developed in the chapter 2. Conventional methods for the binding of DNA and protein have limitations in that binding sites cannot be identified, fluorescent dye labeling on protein is required, or the analytes must be fixed on a surface. However, by using low noise LPCVD SiN nanopores, it was possible to figure out the ZFP binding position in a freely moving state in the ionic solution, without any labeling. These results demonstrated that genetic information can be read rapidly using solid-state nanopores.

Chapter 5 described the results of detection and discrimination of three similar peptides of ~ 40 amino acids and ~ 5 kDa, which only differs in number or location of one cysteine. Based on previous studies that protein identification is possible when the numbers and locations of cysteine and lysine are identified, three different peptides were distinguished by solid-state nanopores. Combining targeted labeling strategy, we confirmed that the peptide conformation through the nanopore can be changed under

the electric field according to the distribution of surface charge of the passing molecules. Based on the relative current drop, distribution, and peak shapes of the nanopore signals, three similar peptides were successfully distinguished.

In this dissertation, the improvement of solid-state nanopore devices and various biological applications using the device are presented. Though not fully described in here, solid-state nanopores have been steadily evolving for the last 15 years. I hope that my research results presented in this dissertation will help many follow-up researchers solve the remaining limitations of solid-state nanopores such as efficient poring method, pore shape and size reproducibility, pore clogging.

요약 (국문초록)

나노포어는 DNA, RNA, 단백질, 펩타이드 등의 작은 크기의 생체 분자들을 높은 정확도로 검지할 수 있는 바이오센서이다. 기본적으로, 나노포어는 지질 이중층이나 인공적으로 제작된 나노미터 두께 수준의 얇은 멤브레인에 형성된 수 나노미터 수준 직경의 구멍을 말한다. 전해질 수용액 내에 전압을 걸어주면 나노포어 멤브레인에 전기장이 생기고 나노포어를 통한 이온 전류가 발생한다. 이 때 수용액 내의 전하를 띤 생체 분자가 나노포어를 통과하며 이온 전류를 일시적으로 막게 된다. 이 때 발생하는 전류 하강의 크기, 지속 시간, 발생 빈도, 모양 등을 분석하여, 통과하는 생체분자의 크기, 모양, 표면 전하 등 생체 분자의 물리적, 화학적 특성을 파악할 수 있다. 이 학위 논문은 주로 기존 솔리드스테이트(solid-state) 나노포어 소자의 개선과, 개선된 나노포어 소자를 이용한 단일 분자 수준의 효율적인 생체 분자 분석에 대한 연구 결과를 담고 있다.

제 1장에서는 나노포어에 대한 전반적인 소개가 서술되어 있다. 먼저, 나노포어의 기본적인 생체 분자 검지 원리를 자세히 소개하고, 나노포어의 가장 큰 두 가지 분류인 단백질 나노포어와 솔리드스테이트 나노포어에 대해 소개한다. 알파헤모라이신(α -hemolysin) 혹은 MspA로 대표되는 단백질 나노포어는, 그 자체로 나노미터 크기의 포어를 갖고 있는 형태의 단백질이고, 보통 지질 이중층에 삽입하여 이온 통로를 형성한다. 솔리드스테이트 나노포어는 단백질 나노포어의 한계점인

물리적 견고성, 실험 지속성, 화학적 안정성, 고정된 크기의 나노포어 직경 등을 개선하고자 개발되었다. 이러한 솔리드스테이트 나노포어를 이용한 다양한 생체 분자 검지 예시들을 서술하고, 솔리드스테이트 나노포어가 갖고 있는 한계점들, 그리고 그것들을 극복하기 위한 연구 결과들을 소개한다.

제 2장에서는 저잡음 솔리드스테이트 나노포어 소자의 멤브레인 품질 향상을 위한 제작 공정의 개선을 서술한다. 기존 저잡음 솔리드스테이트 나노포어는 쿼츠를 나노포어 기판으로 사용하여 dielectric noise를 줄였지만, 해당 소자에 사용된 실리콘나이트라이드 멤브레인은 몇 가지 뚜렷한 한계점이 있었다. 이는 측정 중 나노포어가 단시간 내에 커지거나, 멤브레인이 고온의 클리닝 공정을 버티지 못하거나, 멤브레인 표면에 단백질들이 들러붙는 등의 측정 안정성 문제이다. 여기서는 안정성 측면에서 훌륭한 특성을 갖는 LPCVD 실리콘나이트라이드를 저잡음 나노포어 소자의 멤브레인으로 활용하는 제작 방법에 대해 서술하고, 제작된 나노포어 소자의 특성을 분석한다.

제 3장에서는 솔리드스테이트 나노포어 기판에 자가 조립 펩타이드 필름을 멤브레인 물질로 활용하는 하이브리드 나노포어에 대한 연구 결과를 소개한다. 물/공기 계면에서 우리가 사용한 tyrosine 기반 펩타이드인 YFCFY는 균일하고 안정성 있는 2D 구조를 형성하고, 그 자가 조립 펩타이드 필름은 저잡음 나노포어 기판에 쉽게 전사될 수 있다. 펩타이드 필름의 초기 두께는 10 nm 이상이었지만, 에칭 과정을 통해 약 5 nm 수준으로 조절이 가능하다. 기존의 TEM을 이용한 나노포어 형성 방식을 이용해 펩타이드 멤브레인에 나노포어를 형성하는데 성공했고,

전자빔의 세기를 조절하여 1 nm 수준에서 정교하게 펩타이드 나노포어의 직경을 조절할 수 있었다. 펩타이드 나노포어의 이온 전류 잡음 특성은 일반적인 실리콘나이트라이드 나노포어 혹은 다중층의 2D 물질 나노포어와 유사한 수준으로, 나노포어로 활용되기에 충분했다. 펩타이드 나노포어를 통한 dsDNA의 통과를 약 30 정도의 훌륭한 신호대잡음비와 약 1 bp/ μ s의 느린 통과 속도로 검출할 수 있었다. 이 결과는 자가 조립 펩타이드 필름이 나노포어 멤브레인으로 사용될 수 있고, 솔리드스테이트 기판에 생물학적 기능을 결합시킬 수 있는 가능성을 제시했다.

제 4장에서는 저잡음 솔리드스테이트 나노포어를 이용해 zinc finger protein (ZFP)이 dsDNA의 특정 염기 서열에 결합하는 것을 단일 분자 수준에서 빠르고 정확하게 검출한 결과를 소개한다. ZFP/DNA 결합체가 전기장에 의해 나노포어를 통과할 때, DNA만 통과할 때와는 확연히 다른 전류 하강 형태를 검출할 수 있었다. DNA가 나노포어를 통과할 때, ZFP가 결합된 부분에서 순간적으로 더 큰 전류 하강을 보여주고 이를 바탕으로 ZFP의 결합 여부 및 결합 위치를 확인할 수 있다. 총 길이와 ZFP 결합 위치가 다른 두 종류의 DNA에 대해, 실제 염기 서열 존재 위치와 나노포어 실험을 통해 얻어낸 ZFP 결합 위치가 일치하는 것을 확인했다. 이 결과는 단백질이 DNA에 결합하는 위치를 저잡음 솔리드스테이트 나노포어를 이용해 빠르게 검출하고, DNA의 특정 유전 정보를 단일 분자 수준에서 효율적으로 얻을 수 있음을 보여준다.

제 5장에서는 거의 같은 아미노산 서열로 구성된 세 종류의 유사한 펩타이드를 솔리드스테이트 나노포어로 구별한 결과를 소개한다. 세 종류의 펩타이드는 1개의 cystine의 위치 혹은 개수만 다른 약 40개의

아미노산으로 이루어진 약 5 kDa 수준의 작은 펩타이드이며, 첫번째 펩타이드는 cysteine이 한 쪽 끝에, 두번째 펩타이드는 중앙에, 마지막 펩타이드는 양 쪽 끝에 cysteine이 1개씩 존재한다. 세 종류의 펩타이드가 발생시키는 나노포어 전류 하강 신호는 구별이 힘들었지만, cysteine에 선택적으로 결합하는 음전하를 띠는 분자인 Flamma[®] 496을 붙인 labeled 펩타이드의 경우, 각각의 펩타이드가 뚜렷하게 구별되는 나노포어 신호를 나타냈다. 나노포어 멤브레인에 인가되는 전압에 따라 전류 하강 신호를 비교하여, label의 존재 위치에 따라 펩타이드의 통과 형태가 달라질 수 있음을 확인했다. 펩타이드의 나노포어 통과 형태에 따라, 전류 하강 크기, 전류 하강 크기의 분포, 그리고 단일 분자 수준에서의 픽 모양 분석을 통해 세 종류의 펩타이드를 구별할 수 있었다. 이 결과는 솔리드스테이트 나노포어와 표적화된 labeling 기술의 결합이 궁극적으로 단백질 동정에 사용될 수 있음을 제안했다.

표제어 : 나노포어, 솔리드스테이트 나노포어, 단일분자, DNA 염기서열 분석, 단백질, 펩타이드, 전사 인자, 바이오센서, 단백질 동정, DNA-단백질 상호작용

학 번 : 2013-22479

List of publications

- (1) **Jae-Seok Yu**, Min-Cheol Lim, Duyen ThiNgocHuynh, Hyung-Jun Kim, Hyun-Mi Kim, Young-Rok Kim, and Ki-Bum Kim, "Identifying the Location of a Single Protein along the DNA Strand Using Solid-State Nanopores", ACS NANO, 9 (5), 2015

- (2) **Jae-Seok Yu**, Seong Cheol Hong, Sangwook Wu, Hyun-Mi Kim, Cheolju Lee, Jun-Seok Lee, Ji Eun Lee and Ki-Bum Kim, "Differentiation of selectively labeled peptides using solid-state nanopores", Nanoscale, 11 (5), 2019

- (3) **Jae-Seok Yu**, Jaehun Lee, Misong Ju, Ouk Hyun Cho, Hyun-Mi Kim, Ki Tae Nam and Ki-Bum Kim, "DNA translocation through a nanopore in an ultrathin self-assembled peptide membrane", Nanotechnology, 30 (19), 2019

- (4) William H. Pitchford, Hyung-Jun Kim, Aleksandar P. Ivanov, Hyun-Mi Kim, **Jae-Seok Yu**, Robin J. Leatherbarrow, Tim Albrecht, Ki-Bum Kim and Joshua B. Edel, "Synchronized Optical and Electronic Detection of Biomolecules Using a Low Noise Nanopore Platform", ACS NANO, 9(2), (2015)

- (5) Kyeong-Beom Park, Hyung-Jun Kim, Yun-Ho Kang, **Jae-Seok Yu**, Hongsik Chae, Kidan Lee, Hyun-Mi Kim and Ki-Bum Kim, "Highly reliable and low-noise solid-state nanopores with an atomic layer deposited ZnO membrane on a quartz substrate", Nanoscale, 9 (47), (2017)

(6) Ki-Baek Jeong, Ke Luo, Min-Cheol Lim, Jong-Yoon Jung, **Jae-Seok Yu**, Ki-Bum Kim, and Young-Rok Kim, "Reduction of DNA folding by ionic liquids and its effects on the analysis of DNA-protein interaction using solid-state nanopore", *Small*, 14 (31), (2018)

(7) Kidan Lee, Kyeong-Beom Park, Hyung-Jun Kim, **Jae-Seok Yu**, Hongsik Chae, Hyun-Mi Kim, and Ki-Bum Kim, "Recent progress in solid-state nanopores" *Adv. Mater.* 30 (42), (2018)

(8) Hyun-Mi Kim, Kyeong-Beom Park, Hyung-Jun Kim, Hongsik Chae, **Jae-Seok Yu**, Kidan Lee and Ki-Bum Kim, "The dynamics of electron beam scattering on metal membranes: nanopore formation in metal membranes using transmission electron microscopy", *Nano Convergence*, 5 (32), (2018)

First author presentations

- (1) **Jae-Seok Yu**, Min-Cheol Lim, Young-Rok Kim, and Ki-Bum Kim, “The Detection of SNP(Single Nucleotide Polymorphim) using Low-Noise Solid-state Nanopore”, ENGE 2014 (2014)

- (2) **Jae-Seok Yu**, Min-Cheol Lim, Duyen ThiNgocHuynh, Hyung-Jun Kim, Hyun-Mi Kim, Young-Rok Kim, and Ki-Bum Kim, “Identifying the Location of a Single Protein along the DNA Strand Using Solid-State Nanopores”, 2015 EIPBN (2015)

- (3) **Jae-Seok Yu**, Min-Cheol Lim, Duyen ThiNgocHuynh, Hyung-Jun Kim, Hyun-Mi Kim, Young-Rok Kim, and Ki-Bum Kim, “Single Protein Resolution Mapping of the DNA-ZFP Interaction Using Solid-State Nanopores”, NANO KOREA 2015 (2015)

- (4) **Jae-Seok Yu**, Jaehun Lee, Hyun-Mi Kim, Ki Tae Nam, and Ki-Bum Kim, “DNA Translocation through a Nanopore in Ultrathin Self-Assembled Peptide Membrane”, 648 WE-Heraeus-Seminar: Transport Mechanisms in Biological and Synthetic Nanopores and channels (2017)

- (5) **Jae-Seok Yu**, Jaehun Lee, Hyun-Mi Kim, Ki Tae Nam, and Ki-Bum Kim,

“DNA Translocation through a Nanopore in Ultrathin Self-Assembled Peptide Membrane”, NANO KOREA 2017 (2017)

- (6) **Jae-Seok Yu**, Seong Cheol Hong, Sangwook Wu, Hyun-Mi Kim, Cheolju Lee, Jun-Seok Lee, Ji Eun Lee and Ki-Bum Kim, “Differentiation of selectively labeled peptides using solid-state nanopores”, ENGE 2019 (2019)

Patent

- (1) “나노포어 구조체, 나노포어 구조를 이용한 이온소자 및 나노멤브레인 구조체 제조방법”, 김기범, 유재석, 김형준, 대한민국, 등록번호 10-1759093

- (2) “나노포어 구조체, 나노포어 구조를 이용한 이온소자 및 나노멤브레인 구조체 제조방법”, 김기범, 유재석, 김형준, PCT 출원번호 PCT/KR2015/007399

- (3) “Nanopore Structure, Ionic Device Using Nanopore Structure and Method of Manufacturing Nanomembrane Structure”, Ki-Bum Kim, Jae-Seok Yu, Hyung-Jun Kim, US patent pending, 14/901119

- (4) “나노포어 구조체를 사용한 폴리펩티드의 아미노산 서열을 분석하는 방법”, 이지은, 이철주, 이준석, 홍성철, 박대찬, 옥명렬, 이상욱, 김기범, 김현미, 유재석, 지승욱, 곽동규, 대한민국, 출원번호 10-2017-0184811